Topics in Theoretical Metamorphic Petrology

Catherine J. Wheller
https://orcid.org/0000-0001-5345-1807

Thesis submitted for the Degree of Doctor of Philosophy

1st April 2020

THE UNIVERSITY OF MELBOURNE

School of Earth Sciences

This thesis is being submitted in total fulfilment of the degree.

Abstract

The aim of this thesis is to progress research on three factors influencing phase equilibrium modelling of metamorphic rocks. The first involves updating the activity–composition model for the ilmenite–hematite solid solution so that the P–T conditions for the evolution of rocks containing ilmenite can be modelled across a wider range of composition. The second investigates how to model high-grade rocks that have equilibrated domainally. The third explores whether mechanical closure can be a primary control on mineral assemblage evolution in subsolidus rocks.

A new thermodynamic model suitable for the ilmenite–hematite solid solution has been calibrated in the system FMTOMn (FeO–MgO–TiO_2–Fe_2O_3–MnO). The activity–composition relationships are parameterised in the symmetric formalism, and the model now allows inclusion of long-range cation-order of Fe^{2+}, Mg and Mn. Calibrated using relatively new cation-ordering data from Harrison, Becker and Redfern (2000), Harrison, Redfern and Smith (2000) and Harrison and Redfern (2001), the model is internally-consistent with the thermodynamic database of Holland and Powell (2011). As disorder in mineral solid solutions is a contributing factor to mineral stability at high temperatures, this model should be an improvement for use in calculations at higher temperature.

Interpretation of the metamorphic history of a rock is commonly made through the application of P–T pseudosections which use the effective bulk composition (e.g. whole-rock XRF analysis) as a basis for modelling. This becomes difficult if the rock has equilibrated domainally post the metamorphic peak. Texturally-distinct microdomains can form when there are small-scale effective-composition variations in the rock where localised mineral reaction occurs at the grain scale. A method for interpreting the P–T history of a rock with domainal textures using a P–T grid and compatibility diagrams is investigated, using a texturally complex sapphirine–quartz bearing granulite from the Anosyen tectonic domain in southern Madagascar. Future studies that involve interpreting the conditions of formation of high-grade rocks may benefit from the proposed P–T grid and compatibility diagram method if effective bulk composition is inhomogeneous on a thin-section scale.

The P–T history of the oxidised Anosyen terrane is further constrained using the traditional pseudosection approach on homogeneous samples in the same area. With ferric in the sapphirine model (Wheller & Powell, 2014), it is possible to explore the P–T conditions for the evolution of rocks across oxidation state. For the first time, rocks from highly oxidised to reduced sapphirine granulites can be modelled. The peak P–T conditions experienced in the south-east of the Anosyen tectonic domain attained at least 850°C and pressures greater than 7.6 kbar. This also shows that the stability of sapphirine+quartz can occur below 900°C and may not be a universal ultra-high-temperature (UHT) terrane indicator as commonly suggested.

Finally, rocks with reactions textures that would normally be inferred to have formed due to sluggish kinetics may instead have formed through reaction along an isochor, the rock evolving at constant volume. In order to investigate the consequences of a constant volume process, a calculated volume–temperature (V–T) phase diagram is calculated for a granulite sample that has been reworked in subsolidus fluid-absent conditions. Constant volume paths show that reaction at equilibrium can be attenuated due to the reaction 'vessel' maintaining constant volume, with the external environment unable to accommodate volume change. This has implications for the assumption that depth can be constrained by the mineral assemblage.

Declaration

This is to certify that:

i the thesis comprises only my original work towards the PhD except where indicated in the Preface,

ii due acknowledgment has been made in the text to all other material,

iii the thesis is fewer than 100 000 words in length, exclusive of tables, maps, bibliographies and appendices.

Catherine J. Wheller
1st April 2020

Preface

The candidate is the sole author of all chapters in this thesis. At this time, all chapters are unpublished material not submitted for publication. Prof. Roger Powell (supervisor) assisted with the project conception and with troubleshooting THERMOCALC modelling. No third party editorial assistance was provided in the preparation of the thesis, outside of the candidate's supervisor in accordance with The Australian Standards for Editing Practice. Dr Steven Boger and Prof. Richard White accompanied the candidate in the field in Madagascar and assisted in locating sapphirine-bearing samples. Dr Stephan Buhre provided instruction on how to use the electron microprobe and assisted with the preparation of samples. Wet-chemical analysis (titration) was run by Prof. Richard White at the Johannes Gutenberg University Mainz.

During the PhD tenure, the candidate published a new activity–composition model for sapphirine which is suitable for mineral equilibria modelling in oxidised terranes, which is heavily referenced in, and provided the impetus for Chapter 4:

> Wheller, C. J. and Powell, R. (2014). A new thermodynamic model for sapphirine: calculated phase equilibria in K_2O–FeO–MgO–Al_2O_3–SiO_2–H_2O–TiO_2–Fe_2O_3. *Journal of Metamorphic Geology, 32*, 287–299. doi.org/10.1111/jmg.12067

Chapter 4 was also presented in an early form at the Granulites & Granulites conference in Windhoek, Namibia in 2015:

> Wheller, C. J., Powell, R., White, R. W., and Boger, S. D. (2015). Conditions of formation for an oxidised sapphirine-bearing mineral assemblage from southern Madagascar. In Granulites & Granulites Conference.

This research was supported by an Australian Postgraduate Award (APA) from the Australian Government. The John and Allan Gilmour Research Award (The University of Melbourne), the Nancy Millis Bursary (Graduate Women Victoria), a Student Research Scholarship (Geological Society of Australia - Victoria Division), and a Research Fellowship for PhD students (German Academic Exchange Service, DAAD) supported fieldwork, conference attendance and international collaboration.

To Graeme Wheller
— who instilled a love of geology, and a kidney.

Acknowledgements

I have benefited enormously, both scientifically and personally, from the mentorship of Prof. Roger Powell over many years. Not only from his keen discussions and unfailing ability to fix all of my THERMOCALC problems and roadblocks, but for his kindness, enthusiasm, and unwavering support in anything I've strived to do.

I am grateful for the opportunity to visit Madagascar for my fieldwork, and I thank the villagers and authorities who we encountered for making the trip so fantastically enjoyable. Many thanks to Dr Steven Boger and Prof. Richard White for field and laboratory support in Madagascar and at the Johannes Gutenberg University of Mainz. Thank you to Auguste Razafinjoelina and Matteo [surname unknown] for their impeccable driving, machete skills and company.

My appreciation goes to the School of Earth Sciences and the Faculty of Science at the University of Melbourne for opening doors to develop skills in science communication which I will use throughout my career. Thank you for the opportunity to be involved in the curriculum development, teaching, and examination of two cohorts of undergraduate metamorphic petrology students. This is where I have had the most fun.

My special thanks are extended to the multitude of graduate student colleagues, housemates, and family with whom I've shared thoughtful discussions on life in academia, and what comes next. I would like to acknowledge the supportive friendships, in particular, of Dr Toni Cox, Dr Claire Gorrie, and Dr Lachlan Mason, that have been honed through chain-drinking tea, aggressive progress accountability, and persistent encouragement.

On a more personal note – my decision to study Earth Sciences coincided with a sudden decline of my health in my first year of university and required me to re-calibrate my ideas of the future and of success. I would like to say that the milestones I have reached in the 10 years since are beyond what I could have imagined. I am thankful to have medical professionals around me who barely blinked when I said I wanted to do fieldwork in one of the more remote areas of the world.

Thank you.

Contents

List of Figures

List of Tables

Table 1. Notation - standard units are kJ, Kelvin (K) and kbar

Units and Symbols	
a	activity
a-x	activity-composition relationship
C	number of chemical components in a model system
C_p	heat capacity (kJ K^{-1} mol^{-1})
°C	degrees Celsius (°C = K - 273)
F	assemblage variance
G	Gibbs energy (kJ mol^{-1})
H	enthalpy (kJ mol^{-1})
kbar	kilobar
K	equilibrium constant
μ	chemical potential (kJ K^{-1} mol^{-1})
P	number of phases
P	pressure
Q	order parameter
R	gas constant = 0.0083144 (kJ K^{-1} mol^{-1})
S	entropy (kJ K^{-1} mol^{-1})
T	temperature
V	volume (kJ $kbar^{-1}$ mol^{-1})
W_{ij}	macroscopic interaction parameter between end-members, i-j, (kJ)
X	composition

Phase abbreviations	
cd	cordierite
g	garnet
opx	orthopyroxene
sa	sapphirine
ged	gedrite
bi	biotite
hem	hematite
ilm	ilmenite
sp	spinel
ru	rutile
mt	magnetite
ksp	K-feldspar
pl	plagioclase
q	quartz
liq	silicate melt

General Abbreviations	
FMAS	FeO–MgO–Al_2O_3–SiO_2 model chemical system
FMASO	FeO–MgO–Al_2O_3–SiO_2–O model chemical system
FMASTO	FeO–MgO–Al_2O_3–SiO_2–TiO_2–O model chemical system
KFMASHTO	K_2O–FeO–MgO–Al_2O_3–SiO_2–H_2O–TiO_2–O model chemical system
NCKFMASHTO	Na_2O–CaO–K_2O–FeO–MgO–Al_2O_3–SiO_2–H_2O–TiO_2–O model chemical system

Chapter 1

Introduction

This thesis seeks to extend our knowledge and understanding in the field of metamorphic geology—the study of rocks formed deep in mountain belts—in the light of recent advances in thermodynamic methods for studying metamorphic rocks, and progress in understanding metamorphic processes. Combining the results of theoretical metamorphic petrology with experimental results, laboratory work, and field studies provides metamorphic petrologists with further tools to appropriately understand metamorphic processes and orogensis. A major advance in applying phase equilibria to natural rocks has been the ability to construct quantitative phase diagrams using an internally-consistent dataset of thermodynamic properties combined with activity–composition models for phases. Updates to the dataset and thermodynamic models provide closer approximations to the natural composition of rocks and allow modelling over a larger range of rock compositions.

The research presented herein sets out to explore factors influencing phase equilibrium modelling of metamorphic rocks, including activity–composition models, modelling inhomogeneous rocks, and the controls on mineral assemblage evolution. This thesis begins with an introduction to the equilibrium thermodynamics that are relevant to the content in the following chapters. Each chapter comprises an investigation into a topic in theoretical metamorphic petrology, each of which is part of the continuum of development in the subject. The thesis is structured as follows:

Chapter 2 an introduction to equilibrium thermodynamics

Chapter 3 an activity–composition model

Chapter 4 an approach to modelling high-grade rocks with domainal textures

Chapter 5 an alternative control on the development of mineral assemblages

Chapter 6 concluding remarks and possibilities for future work

Chapter 2

An introduction to equilibrium thermodynamic calculations

2.1 Introduction

To begin a thesis on topics of metamorphic petrology, it needs to be considered that rocks operate in a world governed by chemical systems, which in turn follow the 'laws of thermodynamics'. Chemical systems can be considered open, in which elements can be transferred from or to the environment of the system, or closed, whereby the system is independent on the outside environment. Often, this depends on the scale of the system involved. In the case of a hand specimen of rock, the equilibrium assemblage attained may be a closed system in regards to major elements, but an open system when taking into account, say, H_2 and H_2O. Using equilibrium thermodynamics in petrology to answer questions about rock systems needs to begin with a foundation of the thermodynamics which are involved. Such a foundation is provided by, for example, Callen (1985) and Powell (1978). This chapter is intended to provide the background information on two equilibrium thermodynamic topics: the construction of activity–composition relationships for Chapter 3 and in investigating the applicability of equilibrium thermodynamics on equilibration in rocks, for Chapter 4 and Chapter 5. To this end, the following section considers:

- how to formulate thermodynamic properties
- the approaches that can be made to quantify and predict equilibrium in rocks

The diagrams that make up the figures throughout this thesis are also explained. The view of equilibrium thermodynamics adopted in this thesis is strongly founded on content from Powell (1978), *Equilibrium Thermodynamics in Petrology: an Introduction* and this publication is referenced heavily in this chapter.

2.2 Formulating thermodynamic properties

2.2.1 Gibbs energy of a system

Generally in geological systems, pressure (P) and temperature (T) are taken as superimposed on the system by the external environment. For a mineral assemblage in equilibrium with the imposed P–T conditions, the Gibbs energy of the system is minimised. This energy is the sum of all the Gibbs energies of the phases involved, in proportion to the amount of these phases within the

system. In turn, the Gibbs energies of the phases are made by combining the Gibbs energies of the end-members of the phase, and, as well, the energetic contribution of the mixing of the end-members. the Gibbs energy of an end-member is dependent on pressure and temperature via the enthalpy (H), entropy (S) and volume (V) of the phase. At pressure (P, in bars) and temperature (T, in K) and at enthalpy and entropy at 1 bar, G(P,T), is given by:

$$G(P,T) = H(1,T) - TS(1,T) + \int_1^P V(P,T)\,\mathrm{d}P \tag{2.1}$$

The unit for Gibbs energy is kJ. However Gibbs energy of an end-member can only be defined by comparing to a reference state, in this case the energy of the elements in their most stable state at a given P–T. Thus Equation 2.1 can be written with the terms for entropy, enthalpy and volume represented by a change from this reference state:

$$\Delta_f G(P,T) = \Delta_f H(1,T) - T\Delta_f S(1,T) + \int_1^P \Delta_f V(P,T)\,\mathrm{d}P \tag{2.2}$$

Entropy can be related to temperature by considering the heat capacity (C_p) of the end-member of a phase at constant pressure, so that:

$$S(1,T) - S(1,0) = \int_0^T \frac{\Delta C_p(1,T)}{T}\mathrm{dT}$$

As an end-member approaches absolute zero, it becomes more ordered so that at absolute zero the entropy of the end-member is zero. Therefore,

$$S(1,T) = \int_0^T \frac{\Delta C_p(1,T)}{T}\mathrm{dT} \tag{2.3}$$

Thermodynamic properties are usually tabulated at 1 bar and 298 K (25°C). As such, Equation 2.3 can be written as:

$$\begin{aligned} S(1,T) &= \int_0^{298} \frac{\Delta C_p(1,T)}{T}\mathrm{dT} + \int_{298}^{\mathrm{T}} \frac{\Delta \mathrm{C_p}(1,\mathrm{T})}{\mathrm{T}}\mathrm{dT} \\ &= S(1,298) + \int_{298}^{T} \frac{\Delta C_p(1,T)}{T}\mathrm{dT} \end{aligned} \tag{2.4}$$

Enthalpy, H, refers to the energy directly related to heat. The change of enthalpy resulting from varying the temperature from 298 K to any value of T K – the heat content $H_T - H_{298}$ – is calculated again from the heat capacity, C_p by:

$$H_T - H_{298} = \int_{298}^{T} C_p(1,T)\mathrm{dT} \tag{2.5}$$

Unlike entropy, enthalpy is tabulated with respect to a reference state – the heat energy associated with forming the end-member from its pure elements at a certain pressure and temperature. This gives an 'enthalpy of formation', $\Delta_f H$.

Equation 2.2 can be expanded using Equations 2.4 and 2.5 to give:

$$\begin{aligned} \Delta_f G(P,T) = \Delta_f H(1,298) - T\Delta_f S(1,298) &+ \int_{298}^{T} \Delta_f C_p(1,T)\mathrm{dT} \\ - \int_{298}^{T} \frac{\Delta_f C_p(1,T)}{T}\mathrm{dT} &+ \int_1^{\mathrm{P}} \Delta_\mathrm{f} \mathrm{V(P,T)dP} \end{aligned} \tag{2.6}$$

Equation 2.6 gives the Gibbs energy of formation of an end-member at 1 bar and 298 K using the associated enthalpy of formation, the entropy and heat capacity as a function of temperature and the volume as a function of temperature and pressure. For use in equilibrium calculations, ΔG° is calculated for balanced chemical reactions, allowing cancelling of terms in Equation 2.6, so that:

$$\begin{aligned}\Delta G^\circ = \Delta(\Delta_f H(1,298)) - T\Delta S(1,298) + \int_{298}^{T} \Delta C_p(1,T)\mathrm{dT} \\ -T\int_{298}^{T} \frac{\Delta C_p(1,T)}{T}\mathrm{dT} + \int_{1}^{\mathrm{P}} \Delta \mathrm{V(P,T)dP}\end{aligned} \tag{2.7}$$

2.2.2 A system at equilibrium

Alternative to minimising Gibbs energy of a system, equilibrium of a chemical system can be defined using chemical potential, where the chemical potential of component 1 in phase A is written as μ_{1A}. Chemical potentials are intensive variables, like pressure and temperature, and are constant in an equilibrium. So, the equilibrium relations for the coexistence of phase A and phase B in a binary system are:

$$\begin{aligned}\mu_{1A} &= \mu_{1B} \\ \mu_{2A} &= \mu_{2B}\end{aligned} \tag{2.8}$$

In general for a system at equilibrium, the change in chemical potential of reactions amongst the end-members of the phases must be zero, written as:

$$\Delta\mu = 0\,, \tag{2.9}$$

where $\Delta\mu$ is the change in chemical potential for the sum of μ involved in the product and the sum of μ involved in the reactant of a balanced reaction between end-members.

For a metamorphic rock with many phases in an equilibrium assemblage, there will be many $\mu = 0$ expressions, corresponding to all the reactions between the end-members of the phases. This includes phases that are preserved in the rock as well as phases such as melt that were part of the equilibrium assemblage but have since been lost.

Relating chemical potential to P, T, and X

In the same way that Gibbs energy is a function of pressure, temperature and composition, so too are the derived chemical potentials, given that for a phase, $G = \sum_k p_k\,\mu_k$, where p_k is the proportion of the end-member k in the phase. Chemical potential can be written as a function of P, T, and X and can be be broken down into a term that is:

1. composition-independent (μ°_{1A} – the standard chemical potential of end-member 1 in phase A)

2. composition-dependent ($RT\ln a_{1A}$ – where a_{1A} is the activity of end-member 1 in phase A, R is the gas constant, and T is the temperature in K.)

Thus,

$$\mu_{1A} = \mu^\circ_{1A} + RT\ln a_{1A} \tag{2.10}$$

When the phase of interest, μ_{1A}, is in its standard state, the activity, a_{1A}, equals 1, and therefore the term $RT\ln a_{1A}$ equals 0. When μ_{1A} is outside of the standard state, $RT\ln a_{1A}$ accounts for the difference.

The standard state for end-member of solids is the pure end-member at P–T. Then the standard chemical potential, μ°_{1A}, is equal to the Gibbs energy, where the pure end-member A at 1 bar and 298 K is equivalent to the Gibbs energy of phase A containing only that end-member (G_{1A}) so that,

$$\mu^{\circ}_{1A} = \mu_{1A}|_{x_{1A}=1} \equiv G_{1A} \tag{2.11}$$

in which x_{1A} is the mole fraction of 1 in A. Equations 2.10 and 2.11 give the way to relate activity of an end-member in a phase to composition, pressure and temperature. Creating activity-composition (a–x) relations is an important aspect in the application of equilibrium thermodynamics to rocks.

Composition dependence of chemical potential in a binary system

A number of standard states can be defined depending on whether the reaction contains solids or liquids. For the purposes of this thesis, we will use the above standard state which is used for end-members of solids as well as CO_2 and H_2O in aqueous fluids; and end-members of silicate liquids.

For a composition ranging from pure end-member 1 in phase A (the situation in Equation 2.11 where $\mu_{1A}|_{x_{1A}=1}$ so $\ln a_{1A} = 0$) to a composition mixed with end-member 2, a linear relationship is observed where the slope is defined as RT within a μ_{1A} - $\ln x_{1A}$ plot. The line follows the equation:

$$\mu_{1A} = G_{1A} + RT \ln x_{1A} \tag{2.12}$$

This equation only holds true for compositions near the pure end-member 1 with a small dilution with end-member 2 (this region is termed the 'Raoult's law region').Here, $a_{1A} = x_{1A}$.

The a–x relations where the phase consists mainly of end-member phase 2 with a small dilution by end-member 1, have an additional term which is termed the Henry's law constant ($h_{1A(2)}$) for end-member 1 in phase A diluted by end-member 2:

$$\begin{aligned} \mu_{1A} &= G_{1A} + RT \ln x_{1A} + RT \ln h_{1A(2)} \\ &= G_{1A} + RT \ln x_{1A} h_{1A(2)} \end{aligned} \tag{2.13}$$

Here, $a_{1A} = x_{1A} h_{1A(2)}$.

There is an intermediate region which deals with mixing between end-member 1 and end-member 2 outside of the regions covered by Raoult's and Henry's law. This intermediate involves the activity coefficient, γ_{1A}:

$$\mu_{1A} = G_{1A} + RT \ln x_{1A} \gamma_{1A} \tag{2.14}$$

Equation 2.14 can be used as a general equation to find the the chemical potential of end-member 1 in phase A, where $\gamma_{1A} \to 1$ when $x_{1A} \to 1$ (Rauolt's law) and $\gamma_{1A} \to$ constant when $x_{1A} \to 0$ (Henry's law).

Activity coefficients and the regular mixing model

The activity coefficient of component 1 in phase A, γ_{1A}, reflects the difference between atoms or molecules in a solid solution mixture. The greater the difference, the larger the activity coefficient, reflected by the degree of interactions between adjacent atoms or molecules. Looking at phase A, where there are two atoms, 1 and 2, mixing on the same site, there are interactions between them. The interactions change depending on whether atom 1 is next to another atom 1, or next to an atom 2. If atoms 1 and 2 are of different size or charge, then the differences in interactions will be

greater, which is also reflected in the magnitude of the activity coefficients. An 'ideal solution' is when the interactions are weak between atom 1 and atom 2, thus $\gamma_{1A} = 1$ and $\gamma_{2A} = 1$. When the interactions are strong there is a tendency to unmix at lower temperatures resulting in the formation of separate phase consisting of atom 1 and a phase consisting of atom 2. This creates a solvus.

Equations that relate the activity coefficient γ to composition x are called mixing models as they involve the mixing of end-members within a phase. In a binary system for phase A with mixing between end-members 1 and 2, the 'regular solution model' can be used, where w is the interaction energy of the end-members 1 and 2 being mixed in the phase:

$$\begin{aligned} RT \ln \gamma_{1A} &= w_{1,2}(1 - x_{1A})^2 \\ RT \ln \gamma_{2A} &= w_{1,2}(1 - x_{2A})^2 \end{aligned} \tag{2.15}$$

Equilibrium condition

Returning to the equilibrium constraint so that $\Delta\mu = 0$ for a balanced reaction, we can express each chemical potential of a phase in terms of standard chemical potentials and activities. Then, using r_i as the reaction coefficient of i in the reaction between the end-members, the standard Gibbs energy of reaction is

$$\Delta G^\circ = \sum r_i \mu_i^\circ \tag{2.16}$$

and the equilibrium constant is

$$\ln K = \sum r_i \ln a_i \tag{2.17}$$

giving the general equation for an equilibrium relation of a balanced reaction to be:

$$\Delta\mu = 0 = \Delta G^\circ + RT \ln K \tag{2.18}$$

One way of calculating mineral equilibria involves solving a set of simultaneous non-linear equations consisting of the equilibrium relations of reactions between end-members of phases considered in the equilibria. This is described in detail below in the context of calculating P–T projections.

2.2.3 Modelling thermodynamic data

In order to do calculations using thermodynamic equations, the thermodynamic data that must be collated are:

- those required by Equation 2.7 at standard state conditions in order to calculate ΔG° as a function of P and T ('dataset')
- the activity and composition relationships of the end-members involved in order to calculate the equilibrium constant of the reaction ('a–x relations').

At the time of modelling, the most comprehensive published thermodynamic dataset available is the 6.2 update of Holland and Powell (2011), termed **ds62** for the remainder of this work, which includes values for $\Delta_f H(1, 298)$, S(1, 298), V(1, 298), and the P–T dependence of C_p and V, for the end-members of phases. The thermodynamic dataset is put together through either the direct measurement of these values, or through experiments that constrain phase stability. The dataset is termed 'internally-consistent' as the thermodynamic data are constrained together to be consistent with the experimental data used for calibration.

2.2.4 Application

Activity–composition (a–x) relations for phases are created in order to apply equilibrium thermodynamics to natural systems. These are also termed 'thermodynamic models' and are used in conjunction with a thermodynamic dataset to model the behaviour of metamorphic rocks. Chapter 4 applies a new thermodynamic model for sapphirine to an oxidised terrane, as a response to the availability of a new dataset and thus necessitating a new set of a–x relationship for sapphirine end-members. Chapter 3 presents a recalculation of the a–x relations for the ilmenite–hematite solid solution, also as a response to new experimental data.

2.3 Phase diagrams

Calculations on mineral equilibria undertaken in this study make use of the modelling software THERMOCALC. The software is comprised of two aspects – an internally-consistent dataset of thermodynamic properties, and the code that uses this dataset to calculate equilibrium mineral assemblages (including melt/fluid), mineral compositions and modes at equilibrium. There are two main approaches utilised in solving mineral equilibria; direct Gibbs energy minimisation (Connolly, 1990; de Capitani & Petrakakis, 2010) and solving simultaneous non-linear equations. THERMOCALC employs the latter approach. An alternate program, Perple_X, which calculates the energy of all possible phases over a compositional grid in order to select for a combination of minimum energies to display fields on a phase diagram, was considered, however there are shortcomings to this method, despite being quicker and arguably more user-friendly than THERMOCALC. Perple_X has been found to omit small fields and introduce artefacts into the resulting phase diagrams, however it would be useful for a first-pass approach (R. Powell, pers. comm.). It is also difficult at this stage to calculate grids and compatibility diagrams with Perple_X, and as such THERMOCALC was chosen for this study. The calculations presented in Chapters 3 and 4 utilise the THERMOCALC software version tc340i and the *drawpd* program (version dr116i; available online at http://www.metamorph.geo.uni-mainz.de/thermocalc/dataset6/index.html). Chapter 5 use THERMOCALC software version tc350i using an updated version of the Holland & Powell 2011 data set (**ds633**, July 2019; file tc-ds633.txt).

The Holland and Powell (2011) updated dataset contains the thermodynamic properties of 254 end-members. In addition to adding more end-members, there have been major methodological changes since the earlier datasets of Powell and Holland (1985) and Holland and Powell (1990, 1998). One of these is the way that thermodynamics of certain end-members are parameterised. Minerals with order–disorder were previously treated with a Landau tricritical model as it allowed order–disorder to be represented in simple stoichiometric phases. Some solid-solutions are still parameterised with a Landau expansion (e.g.ilmenite and hematite in Table 2b in Holland & Powell, 2011), when a symmetric formalism (SF) model (where the order–disorder transitions are represented with a macroscopic Bragg-Williams model) would be more appropriate. The advantage of SF is that solid-solutions can be constructed using standard configurational entropies and activity–composition expressions. This allows calculation of phase equilibria in multi-component systems (Holland & Powell, 2011). Chapter 3 looks at reparameterising the ilmenite–hematite solid-solution with SF.

THERMOCALC requires manual input from the user to calculate phase diagram lines and boundaries which are subsequently assembled in the program *drawpd*. A script file is created containing information of projection planes, bulk compositions and 'starting guesses' depending on the diagram to be calculated – these are input by the user. Starting guesses are used for each defined

variable in an a–x model and are crucial in whether a solution to a line or point is found. A negative result – no line or point returned – could be due to an inappropriate starting guess, in which case the guess can be changed manually in the script file. Some equilibria are very sensitive to the degree of order within a mineral or when a reaction occurs close to the solvus, particularly affecting the composition of magnetite–spinel, ilmenite–hematite, and K-feldspar–plagioclase. The following subsections detail the method in which P–T projections, compatibility diagrams, and pseudosections are produced and discusses the value of diagrams that will be used throughout this thesis.

2.3.1 Chemical systems

In order to model metamorphism in rocks, a simplified chemical system incorporating the major rock forming minerals is utilised to represent the main chemical variants in the rock. The phase equilibria in these systems can be represented in a C + 1 dimensional space (the 'total phase diagram'), where C is the number of constituent components. The model system K_2O, FeO, MgO, Al_2O_3, SiO_2, H_2O (KFMASH) can be used for describing metapelites as this covers the main minerals in this composition as well as the Fe–Mg Tschermak's substitution, however does not include information on the oxidation state of the rock or consider Na and Ca bearing feldspars. The diagrams in Chapter 4 use the more geologically realistic chemical systems of KFMASHTO and NCKFMASHTO which allow the influence of the oxides K_2O, FeO, MgO, Al_2O_3, SiO_2, H_2O, TiO_2 and Fe_2O_3 to be represented in the former, with the addition of Na_2O and CaO in the latter. These components, as oxides, allow for description of the major chemical variants within minerals and melt of the rock system of interest.

Within a P–T-X variable space, phase diagrams reflect the Gibbs Phase Rule;

$$\mathrm{F} = \mathrm{C} - \mathrm{P} + 2 \tag{2.19}$$

which relates the number of phases in the system (P) and the number of components (C) to the variance (F), also referred to as 'degrees of freedom'. Often, one or more phases are considered 'in-excess' and therefore considered to be involved in all the reactions. When a phase is in-excess, the phase will be denoted as + x (e.g. + q + mu) in the diagram.

2.3.2 P–T projection

P–T projections, or 'petrogenetic grids', are diagrams that project all stable invariant points and univariant reaction lines in the total phase diagram for all bulk compositions within a system onto the P–T space (Powell, Holland & Worley, 1998). As the P–T projection is not reliant on a bulk composition to be constructed, only a chemical system, one diagram can be used for all rocks within that chemical system. THERMOCALC is used to calculate univariant lines and invariant points, however it does not give the relative stabilities of the reactions, requiring the user to determine whether a reaction is stable or metastable. Lines are labelled with the participating phases on each side of the univariant reaction. Invariant points are labelled based on the absent phases (where modes have gone to zero) with these phases given in square brackets (as per Powell et al., 1998). Figure 2.2 shows an example P–T projection for KFMASTHO for high temperature metapelites.

Determining stable or metastable reactions

THERMOCALC calculates the entire reaction line within a specified P–T range which will go through the relevant invariant point. It is up to the user to determine which extension past the invariant is the stable reaction. To determine which, the user must invoke *Schreinemakers' Rule* whereby around an invariant point the metastable extension of a reaction not involving i (denoted [i]) lies between i-producing reactions. Geological experience as to whether a phase will be found on the high or low pressure/temperature side of a reaction line is then applied to construct a reaction bundle (e.g. liq is stable on the side of high temperature). This process of determining which part of the reaction is metastable or stable is illustrated in Figure 2.1.

Figure 2.1 involves reactions around a spinel absent [sp] invariant point in the chemical system FMAS (C = 4). The phases stable at the invariant point are garnet, sapphirine, orthopyroxene, sillimanite, cordierite and quartz (when F = 0, P = 6). A univariant reaction (F = 1) will involve 5 phases. This invariant point is surrounded by a reaction bundle involving five univariant lines that appear on both sides of the point. One of these extensions will be stable, the other will be metastable. THERMOCALC outputs that a reaction is taking place, but does not determine which side of the reaction is stable. For the cordierite-absent reaction [cd], garnet and sapphirine are chosen to lie on the high temperature side as sapphirine is observed to form at high temperatures.

The sapphirine-absent reaction [sa] will be stable if it does not lie between two sapphirine producing reactions. As the [cd] line next to it has sapphirine forming up temperature, and thus within the potential [sa] absent reaction, this part of the reaction is metastable. This logic is then followed for each of the reactions involved (stable reactions shown in red). Once a stable reaction bundle is developed, it can be linked to another reaction bundle where connecting univariant reactions are both stable. Grids are assembled line-by-line through THERMOCALC output and drawn in *drawpd*.

P–T projections were first used by Bowen (1940) to provide a preliminary approach for identifying P–T conditions as reflected by observed mineral assemblages. Univariant equilibria are projected onto a P–T plane over a range of pressure and temperature. The crossing of a univariant line relates to a discontinuous change in stable mineral assemblage. An example of a P–T projection, such as the one presented in Chapter 4 is shown in Figure 2.2. The variance and number of phases present at each point and line follow the phase rule in Equation 2.19. KFMASHTO is an eight component system (C = 8). At an invariant point where F = 0, there are ten phases present (P = 10), remembering that there are five phases in-excess in this example. Each of the stable univariant lines which extend from an invariant point has a degree of freedom of one (F = 1). Therefore each univariant reaction involves four phases (in addition to the five in-excess phases) to make a total of nine phases (P = 9). Note that this diagram contains multiple reaction bundles, as described above where Schreinemakers' Rule has been applied and multiple stable univariant reactions combined.

These diagrams show the potential mineral assemblages via univariant equilibria for *all* bulk compositions, that is, they are independent of X. This means that some parts of the equilibria may not be experienced, or 'seen', by a particular bulk composition. The reactions within the KFMASHTO P–T grid are crucial in the interpretation of equilibrium reactions in rocks where use of a bulk composition is inappropriate – as seen in Chapter 4.

2.3.3 Compatibility diagrams

Exploration of the univariant reactions experienced by a rock in a simplified chemical system, independent of composition can be further investigated by examining a P–T grid at a specific P

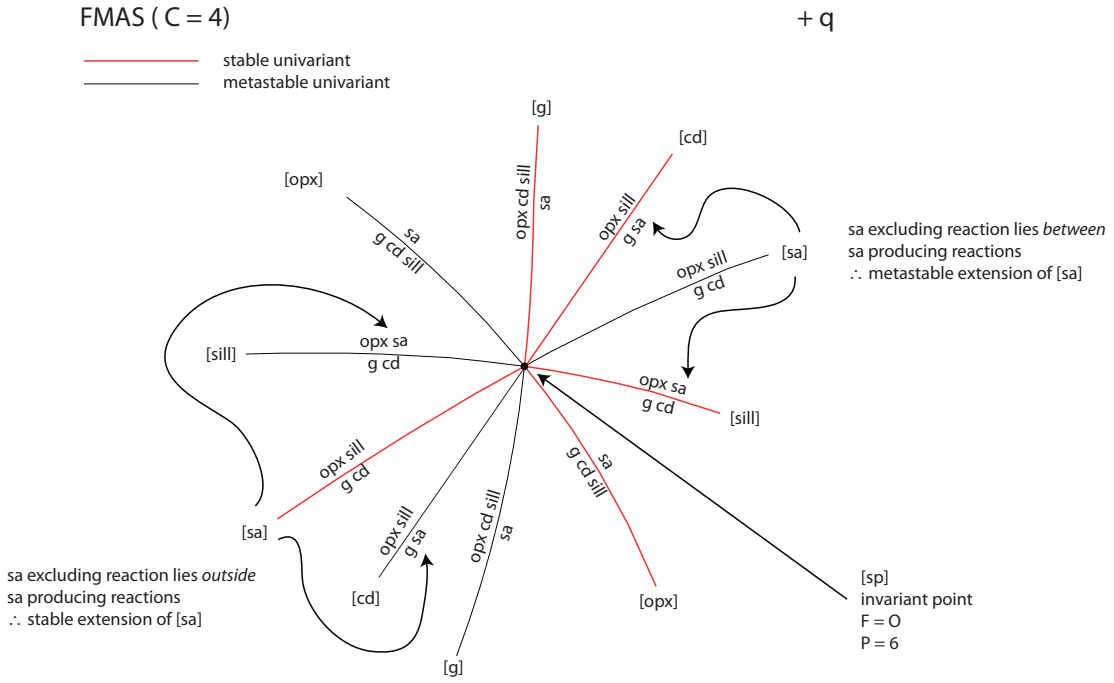

Figure 2.1. The spinel-absent invariant point within the FMAS system. Each univariant reaction line intersects the invariant point and continues to the opposite side. Red lines show the stable univariant lines as determined using Schreinemakers' Rule (described in text). Univariant lines are described using their absent phase [P].

and T. Compatibility diagrams provide a graphical way of showing the composition of phases as well as their respective stabilities with other phases at a given P–T.

Structure of a compatibility diagram

In order to reduce the system so that it can be represented in a two dimensional compatibility diagram, a number of phases must be taken as in-excess. The equilibria are then projected from these phases onto a projection plane, reducing the dimensionality of the system by one for each projected phase. The choice of projection plane is non-trivial as it affects which minerals can be plotted. Phases can be plotted at infinity (i.e. rutile in many of the diagrams) however this is only a reflection of geometry and does not affect the interpretation of the diagram.

Compatibility diagrams are composed of three main structural features – triangular divariant fields ('tie-triangle' – conventionally coloured white), trivariant tie line fields joining two phases plus those in-excess (lighter shade colour – here blue) and quadrivariant fields (darker shade of blue) which represent a field with a single phase in addition to those in-excess (e.g. sapphirine with liq + sill + q + ksp + ilm). Compatibility diagrams are most powerful when presented in series, for example reflecting changes along P or T paths. The series can show continuous and discontinuous reactions. A continuous reaction is manifested by a smooth transition of a tie triangle (divariant) across the diagram as the composition of solid solutions change. As each diagram is drawn so that it represents a singular point in P–T on a P–T grid, a continuous reaction shows the change in composition within a P–T field. A discontinuous reaction represents the reaction when crossing a univariant line of the P–T grid and is displayed as the breaking or formation of tie lines on the compatibility diagram.

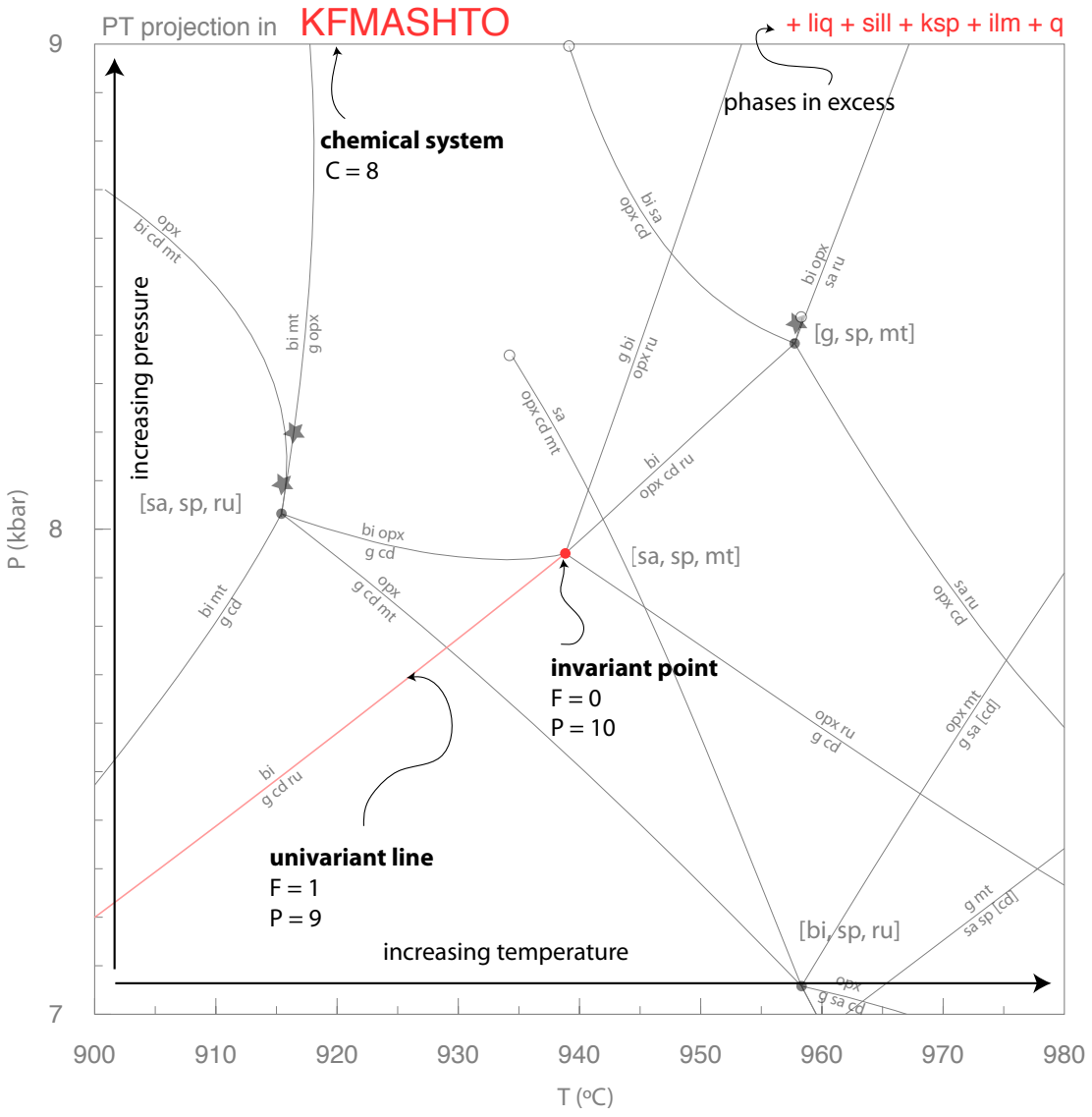

Figure 2.2. An explanatory P–T projection in KFMASHTO (+liq + sill + ksp + ilm + q). In-excess phases are not included in the labelling of univariant lines. This grid joins reaction bundles that have been calculated using Schreinemakers' Rule. Key features are labelled in red. Stars and open circles represent singularities and subsystem invariant points. F, C and P refer to variables in the Gibbs Phase Rule. See text for further explanation.

The most common way of displaying compatibility diagrams for metapelites is the AFM ternary compatibility diagram, however for the purposes of this study, an orthogonal compatibility diagram in KFMASHTO is utilised. In this diagram (Figure 2.3), sillimanite, quartz, potassium-feldspar and ilmenite are in-excess, in addition to either cordierite or liquid depending on the outcome of interest. This allows for possible stable mineral assemblages involving garnet, orthopyroxene, sapphirine, rutile, spinel and magnetite.

The projection plane of this orthogonal compatibility diagram is explained in Figure 2.3. The projection plane must lie between the projected phases and the phases from which they are projected. Projection from the ilmenite-hematite solid solution plane is successful if the projection plane corresponds to the Al-free spinel plane. This generates a compositional FeO-MgO-TiO_2-Fe_2O_3 (FMTO) compatibility diagram with the positions of the Al-free spinels, ülvospinel (ulv), magnetite (mt), magnesioferrite (mf) and magnesium titanate (mti) as the corners of the projection plane. The horizontal axis is in terms of MgO/(FeO+MgO) and the vertical axis corresponds to increasing Ti content from low y to high y where oxidation state decreases as y increases. Each border of the diagram corresponds to a subsystem mineral assemblage, a feature of decreasing combinations of MgO, FeO, TiO_2 and Fe_2O_3. For example the bottom left corner of the orthogonal diagram represents the subsystem KFASHO as MgO (M) and TiO_2 (T) have been lost from the total chemical system.

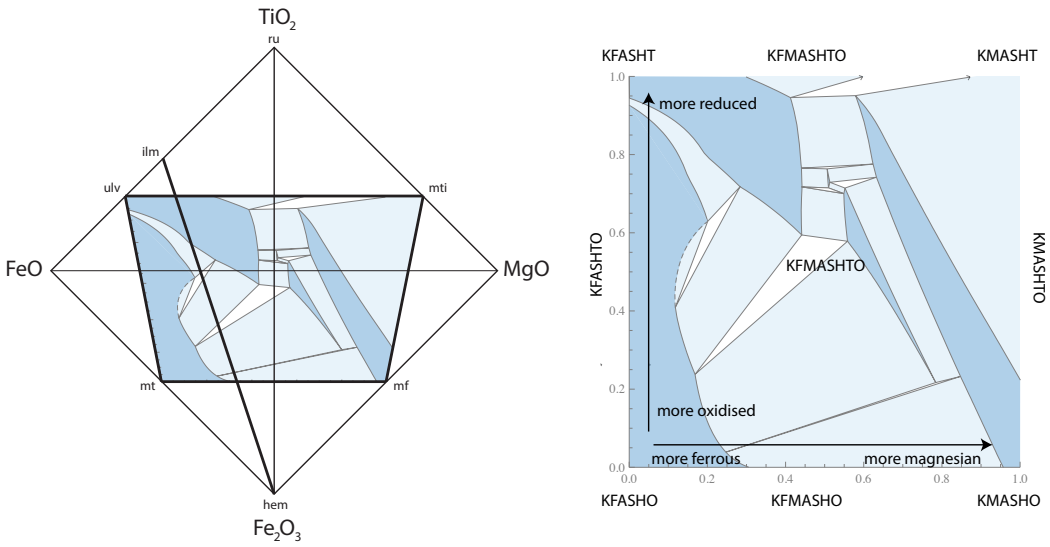

Figure 2.3. Left: Reference plane of FMTO projected from ilm-hem to construct a KFMASHTO orthogonal compatibility diagram (right) displayed here with the location of total system and subsystem assemblages. One phase fields are labelled by their respective phases. See text for further explanation. This compatibility diagram is calculated in Chapter 4

Calculations involving the magnetite-spinel solvus proved difficult, and would often result in both phases plotting on the same side of the solvus resulting in a degeneracy where both phases have the same composition. This is fixed by using vastly different starting guesses for each of mt and sp in order to calculate as close to the top of the solvus as possible. It was not possible to completely close the solvus in each of the involved compatibility diagrams, so an approximated best fit (dashed boundary line) is drawn as relevant.

Using a compatibility diagram

The strength of a compatibility diagram is in exploring how a stable mineral assemblage can change with different bulk compositions under the same imposed P–T regime. A bulk composition can

be plotted on a diagram (a point on a compatibility diagram in FMTO space) at a specific P–T and for example may plot within the one-phase field of sapphirine. If the bulk composition was more ferrous, then at the same P–T the bulk composition may plot in a tie-triangle containing sapphirine, garnet and magnetite. This is useful if a rock sample is thought to be domainal, as there may be two or more localised 'bulk compositions'.

The evolution of stable mineral assemblages with the same bulk composition over P–T can be explored over a series of compatibility diagrams. If a decompression path is being investigated, then a series of diagrams can be constructed at constant T with decreasing P. A useful way of doing this is to choose P intervals based on the crossing of univariant lines so that discontinuous reactions seen by the bulk composition can be investigated. Using petrological interpretations of textures in the prograde, at peak, and during retrograde, the compatibility diagrams can be used to investigate the reactions involved and at what pressure and temperature they occur.

2.3.4 Calculating P–T projections and compatibility diagrams

As mentioned above, solving mineral equilibria in THERMOCALC requires solving simultaneous non-linear equations. When calculating an invariant point for a P–T grid, say [sa, sp, mt] in Figure 2.2, the equilibrium for coexisting bi-opx-cd-ru-g-liq-sill-ksp-ilm-q is used. This can be extended to calculate all the equilibria of a particular variance in the system (F). This involves finding the different combinations of $F = C - P + 2$ (Equation 2.19). The [sa, sp, mt] point at around 8 kbar and 940°C (Figure 2.2), involves a set of non-linear equations consisting of the the equilibrium relationships between the end-members of the phases being considered (Equation 2.18):

$$\begin{aligned} 0 &= \Delta G_1^\circ + RT \ln K_1 \\ 0 &= \Delta G_2^\circ + RT \ln K_2 \\ &\vdots \end{aligned} \tag{2.20}$$

where ΔG° is a function of P–T and K is a function of P–T and of the compositions of all the phases involved in the reaction (Powell et al., 1998). Pressure, temperature and composition are unknowns and need to be solved for. For [sa, sp, mt] in Figure 2.2, the independent set of reactions is:

1. 4q = qL
2. 8sill = 5silL
3. qL + 2foL = 4en
4. qL + 2faL = 4fs
5. dilm = oilm
6. en + mgts = py
7. 8py + 3qL = 8en + 4crd
8. 20en + 15silL = 8py + 8crd
9. 8alm + 3qL = 8fs + 4fcrd
10. 20fs + 15silL = 8alm + 8fcrd
11. san = kspL
12. 2fm = en + fs
13. 2en + 4ru = qL + 4geik
14. 2fs + 4ru = qL + 4oilm
15. crd + h2oL = hcrd
16. 3en + 2hem = 2kho
17. east + 2en = py + phl
18. 4alm + 2kspL + 2h2oL = 2ann + fs + 2fcrd
19. py + 3obi = alm + 3phl
20. py + ann = alm + phl
21. 7phl + 10crd + 6geik = 7py + east + 6tbi + 6hcrd

22. py + 2fbi = kho + 2east
23. phl + 2fopx = kho + east

Each reaction has an equilibrium reaction, e.g. for reaction 7 and 8 above substituted into Equation 2.20;

$$\begin{aligned} 0 &= \Delta G^{\circ}_{7} + RT \ln \frac{(a^{opx}_{en})^{8}(a^{cd}_{crd})^{4}}{(a^{g}_{py})^{8}(a^{liq}_{qL})^{3}} \\ 0 &= \Delta G^{\circ}_{8} + RT \ln \frac{(a^{g}_{py})^{8}(a^{cd}_{crd})^{8}}{(a^{opx}_{en})^{2}(a^{liq}_{silL})^{3}} \\ &\vdots \end{aligned} \tag{2.21}$$

Activity expressions for each end-member are tabulated in the a–x relations for each mineral. These can then be substituted into Equation 2.21 for each of the 23 equilibrium relationships. The non-linear equations can be solved simultaneously for P, T and equilibrium conditions of the coexisting minerals. This gives the P–T coordinate of the invariant point and the equilibrium conditions of the stable minerals in the equilibrium assemblage. For [sa, sp, mt], the invariant is stable at 7.967 kbar at 938.82°C with the set of variables for each model phase as: x(g) = 0.3734, f(g) = 0.04615, x(bi) = 0.1807, y(bi) = 0.2000, f(bi) = 0.08802, t(bi) = 0.3478, Q(bi) = 0.06323, x(opx) = 0.2615, y(opx) = 0.1998, f(opx) = 0.05757, Q(opx) = 0.1180, x(cd) = 0.1017, h(cd) = 0.5564, q(L) = 0.2364, fsp(L) = 0.4082, ol(L) = 0.008641, x(L) = 0.5097, h2o(L) = 0.3151, i(ilm) = 0.3151, g(ilm) = 0.8207, Q(ilm) = 0.2657. These variables are used internally in THERMOCALC and are either compositional variables or order variables. The compositional variables are defined relating to their mineral analytical composition and definitions can be found at the beginning of the a–x coding for each phase in the THERMOCALC a–x file.

2.3.5 P–T, T–M_O, T–M_{H2O} pseudosections

Estimation of which reactions will be experienced by a *specific* bulk composition requires a more refined approach. This can be achieved with P–T pseudosections as the diagrams are equipped to represent natural mineral assemblage evolution through multi-variant equilibria (White & Powell, 2002). In contrast to P–T projections, pseudosections are calculated at a fixed bulk rock composition to simplify the interpretation of mineral equilibria. As pressure and temperature vary, the bulk composition is kept constant, allowing inferences on the evolution of a mineral assemblage through prograde and retrograde metamorphism. These diagrams display multi-variant stability fields of mineral assemblages through varying conditions and can be contoured for modal proportion of minerals and mineral compositions. As a line on a pseudosection is crossed, the variance of the field increases or decreases by one. Univariant reactions can be usefully considered as zero-width fields. For example, for a diagram in the chemical system NCKFMASHTO (C = 10), a divariant field (F = 2) will involve ten phases (P = 10). Assemblage fields are, by convention, shaded based on their variance, with higher variance assemblages shaded darker. More information on the construction of pseudosections are given in Powell and Holland (1988).

While the natural choice of variables to use as axes on a pseudosection are P and T, other variables can be chosen to represent the particular geological processes thought to be occurring in a mineral assemblage. *Intensive variables* are equalised within the system during equilibration (i.e. pressure by deformation; temperature by conduction and convection; and chemical potential by diffusion), while extensive variables depend on the amount of material present (Powell, Guiraud & White, 2005). Examples of intensive variables include pressure (P), temperature (T), and chemical potential (μ). Examples of extensive variables include volume (V), composition (X) and entropy

(S). Diagrams can be constructed interchanging conjugate pairs of intensive and extensive variables – that is P and V; T and S; and μ and X. When swapping conjugate variables, the corresponding extensive variable is now passive. A system is now able to be investigated where volume changes are important for reaction (Powell et al., 2005) or when oxidation state is an important variable (e.g. K. A. Evans, Powell & Frost, 2013; Wheller & Powell, 2014). A P–T diagram contoured for volume (isochors) can show the volume change associated with a reaction to be accommodated by deformation of the rock. However if a rock is not able to deform to accommodate the volume change, then a V–T pseudosection contoured for pressure can show what may happen in the evolution of that assemblage. In Chapter 5, a V–T pseudosection is calculated. In this example, the changes in mineral assemblage are investigated by stating that the system is not operating at a constant superimposed pressure (e.g Carmichael, 1987), and that reactions may continue down an isochor. This diagram allows investigation into mineral behaviour at constant volume with pressure gradients set up between mineral inclusions and hosts (Powell et al., 2005).

Choosing a bulk composition that represents the volume of equilibrium is an important factor in constructing a pseudosection. Bulk composition can be determined directly through crushing and subsequent analysis through X-ray fluorescence (XRF) if the equilibrium volume is large. The amount of H_2O (H) and the oxidation state (O) may be estimated using loss on ignition (LOI) value and Fe^{3+} titration respectively, but these are likely to be maximum values. Commonly, T–M_O and T–M_{H2O} are used to investigate the consequence of varying the amount of water or the oxidation state of the bulk composition. As both H_2O and O are not easily constrained by analysis, these diagrams are a necessity in identifying an appropriate value to use for a subsequent P–T pseudosection. The implications for the stable mineral assemblage at different bulk water content and oxidation state of the system are investigated in Chapter 4.

Chapter 3

An approach to the ilmenite–hematite solid solution

3.1 Introduction

Knowledge of the activity–composition (a–x) relationships for minerals is required for calculation of the conditions of formation of rocks. As further experimental data becomes available and new ways of creating a–x relationships developed, the need for re-calculation of the thermodynamic properties of minerals arises. This new thermodynamic description for ilmenite is designed so that it can be utilised for petrological calculations with all common phase modelling software.

The current a–x model (White, Powell & Johnson, 2014) for ilmenite, based on (White, Powell, Holland & Worley, 2000) is insufficient in how it deals with the substitution of magnesium and manganese into the mineral lattice as well as not incorporating relatively new time-of-flight neutron powder diffraction experimental data (Harrison, Becker & Redfern, 2000; Harrison, Redfern & Smith, 2000). These experiments allow new calculation of the critical temperature of ilmenite. The existing model is acceptable for petrological calculations at lower temperatures because the degree of disorder in solid solution is small. Disorder in mineral solid solutions is a contributing factor to mineral stability at higher temperatures and thus there is a need to incorporate order–disorder in ilmenite in calculations on rocks formed at higher temperature.

This chapter provides:

1. a revised critical temperature (T_c) for pure ilmenite;
2. a new estimate of the solvus for the ilmenite–hematite solid solution;
3. new values for macroscopic interaction energies between the ordered and disordered end-members of ilmenite and hematite; and
4. the incorporation of magnesium and manganese into the model.

The new a–x model for the ilmenite solid solution can be used to provide more geologically realistic estimations for calculations involving ilmenite in the system MnNCKFMASHTO.

3.2 Thermodynamic descriptions

A thermodynamic description of a mineral refers to the properties of its constituent end-members and the activity–composition (a–x) relations that represent the energetics of combining these end-

members within the mineral. Refinement of thermodynamic descriptions is essential to make petrological calculations on metamorphic assemblages.

The published thermodynamic descriptions of White, Powell and Holland (2007) have been widely used in thermodynamic modelling, allowing consideration of mineral assemblages in rocks to work with the internally-consistent dataset of thermodynamic properties compiled in Holland and Powell (1998) for mineral, fluid and melt end-members. An update of this dataset was made available in 2011 with the publication of Holland and Powell (2011). This dataset is referred to in the literature as **ds62**, and is a significant improvement on the Holland and Powell (1998) dataset, which, in its 2003 update form, is commonly referred to as **ds55**. The improvement is due to the inclusion of reliable calorimetric and experimental data published since the last major upgrade of the dataset in 1998, as this increases the reliability of the data as well as allowing the incorporation of new mineral end-members.

3.2.1 The current a–x file and what needs changing

As a consequence of the new dataset, the opportunity exists to create new a–x relations for minerals using a new set of principles for parameterising a–x relations (Powell, White, Green, Holland & Diener, 2014). White, Powell, Holland, Green et al. (2014) and Wheller and Powell (2014) present the most recent update to the a–x relations. An extension in the same series of papers (White, Powell & Johnson, 2014) investigates these relations with extension into a manganese-bearing system.

The ilmenite–hematite solid solution was chosen to be modelled in this study, as the previous models (White et al., 2000; White, Powell & Johnson, 2014) are inadequate in explaining behaviour at high temperatures. Experiments by Harrison, Becker and Redfern (2000), Harrison, Redfern and Smith (2000) provide some of the necessary data to build into the models.

The current downloadable ilmenite a–x model (tc-6axmn.txt accessed 01/02/2017) is from White et al. (2000), with a later addition allowing solid solution towards geikielite with Mg just on the A site. Previous models used the simplification of assuming that the interaction energies between Mg– and/or Mn–bearing end-members and other end-members are zero, however with White, Powell and Johnson (2014) the a–x relations involving Mg and Mn are given non-zero W. The model continues to allow magnesium and manganese to be present only on the A site with ferrous iron and titanium on both the A site and the B site, so the possibility of order–disorder for either cation is not considered. This current model can be found in the Appendix to this chapter.

White et al. (2000) use the temperature of convergent ordering of pure ilmenite, T_c, to be 1600°C; the enthalpy difference between the ordered and disordered ilmenite end-members, ΔH, to be 15.6; and the tricritical point to be 480°C (Ghiorso, 1990).The current interaction energies for ilmenite are presented in Table 3.1. Table 3.2 shows interaction energies required if we are to allow order–disorder for Mg and Mn.

Table 3.1. Interaction energies (W_{ij}) for ilmenite as per White, Powell and Johnson (2014)

	dilm	hem	geik	pnt
oilm	15.6	26.6	4	2
dilm		11	4	2
hem			36	25
geik				4

The new model will include interaction energies between the microscopic end-members oilm, dilm and hem with ogeik, dgeik, opnt, and dpnt (for formulae, see the following section) and will also refine the previously included interaction energies using new experimental data. The model

Table 3.2. All interaction energies (W_{ij}) for ilmenite, highlighting the W needed for the new model, given the order–disorder model adopted

	dilm	hem	ogeik	opnt	dgeik	dpnt
oilm	15.6	26.6	4	2	?	?
dilm		11	4	2	?	?
hem			36	25	?	?
ogeik				4	?	?
opnt					?	?
dgeik						?

will be in a format suitable for THERMOCALC using the process of creating an a–x model in light of the new regularisation approach, termed micro-ϕ, in Powell et al. (2014).

Previous work

Ghiorso and Evans (2008) present a model for the thermodynamic properties of the ilmenite–hematite solid solution calibrated from the Harrison, Becker and Redfern (2000), Harrison, Redfern and Smith (2000) data and experimental data by B. W. Evans, Scaillet and Kuehner (2006), Lattard, Sauerzapf and Käsemann (2005). The model aims to include the lower temperature magnetic aspects of the ilmenite–hematite system as well as do precise modelling of the available experimental data on order–disorder in this system. It does this by using thermodynamics up to quartic in compositional and order parameters. As a consequence the model is complex and cannot be coded for general petrological calculations in available software. An energetically simpler and more transparent model up to quadratic in compositional and order parameters is presented here which provides a reasonable fit of the available data. It also has the advantage of being able to be used in petrological calculations using THERMOCALC and other calculation software.

3.2.2 Creating an a–x model

Most minerals fall into the category of multi-component solid-solutions, in which the thermodynamics are usually only experimentally constrained within a few compositional dimensions. Minerals are described within a simplified chemical system of oxides to represent the main chemical variations within the rock system under consideration. For ferromagnesian minerals, data may be constrained in simple chemical systems like FMASH (FeO - MgO - Al_2O_3 - SiO_2 - H_2O) and KMASH (K_2O - MgO - Al_2O_3 - SiO_2 - H_2O), however for more geologically realistic calculations, extension into more complex systems such as KFMASHTO (K_2O - FeO - MgO - Al_2O_3 - SiO_2 - H_2O - TiO_2 - Fe_2O_3) must be undertaken.

In the case of ilmenite, available experimental data are in FTO (FeO - TiO_2 - Fe_2O_3) but extension into a system including MgO and MnO is necessary to accommodate common substitutions. The process of extending a system in the absence of experimental data is done using an approach called *regularisation* which involves use of heuristics to determine unknown parameters. Making thermodynamic descriptions involves:

formulation the algebraic expression of thermodynamic descriptions (a–x relations), involving use of ideal mixing on sites and the symmetric formalism (e.g. Holland & Powell, 1996b; Powell & Holland, 1993)

parameterisation thermodynamic descriptions (a–x relations). This involves fitting experimental data as well as regularisation when data are unknown. Micro-ϕ is a new regularisation technique (Powell et al., 2014).

Between the a–x relations for **ds55** and **ds62**, the expression of the algebra (*formulation*) has remained of the same structure, while the way in which thermodynamics descriptions are made (*parameterisation*) is completely new when *regularisation* is involved. Accordingly, the structure of the mineral with consideration of multi-component solid-solutions is key here.

The regularisation technique micro-ϕ relates the a–x relations for a different subsystem of a mineral to the better known a–x relations in the more commonly experimentally categorised Mg–Al subsystem, at least in silicates. For instance, the microscopic w for Mn–Fe^{3+} can be made proportional to the Mg–Al subsystem, where the proportionality is represented by ϕ (White, Powell & Johnson, 2014). To do this, the macroscopic interaction energies (W) are broken down into their constituent microscopic same-site and cross-site microscopic interaction energies (w) that come from pairwise interactions between cations on sites in the mineral (Powell & Holland, 1993). Subsequently, simplifications and approximations are made to the w before reassembling back to macroscopic W (see end of chapter).

The following sections look at the structure of unary ilmenite and the ilmenite–hematite binary before considering the extension of the thermodynamic description into the ilmenite–hematite–geikielite–pyrophanite quaternary system. Here the structure of ilmenite is investigated including;

1. end-member definitions;
2. the solvus;
3. order parameters; and
4. the effect of Landau versus symmetric formalism (see Holland & Powell, 1996b) as a way of accounting for mineral behaviour between ordered and disordered states.

3.2.3 Summary

Refinement of thermodynamic descriptions leads to more geologically realistic petrological calculations. A new dataset, termed **ds62** includes more reliable calorimetric and experimental data since the previous update. The opportunity for creating new thermodynamic descriptions based on this dataset has therefore risen, with the ilmenite–hematite solid solution being chosen for this study. The new ilmenite model will expand to include order–disorder within the Mg and Mn end-members and refine current model values with new experimental data to be used in petrological modelling using software such asTHERMOCALC. This involves extending the model to include common substitutions using a regularisation approach called micro-ϕ.

3.3 Considering ilmenite

Ilmenite and its associated members in solid-solution are found as accessory minerals in igneous and metamorphic rocks. When of an intermediate composition, the solid-solution exhibits exsolution. For practical application of an Fe-Ti oxide geothermometer and the use of the mineral in calculate pseudosections for application to mineral assemblages in rocks, constraints of thermodynamic properties between 700°C (973K) and 900°C (1173K) are most important.

Mineral composition is represented in terms of a linear combination of oxides. These oxides are termed *components* and make up the model chemical system in which calculations are undertaken (e.g. KFMASHTO). Within the chemical system are end-members of minerals which have a fixed composition and stoichiometry. There are three types of end-members: microscopic, macroscopic and compositional (Powell et al., 2014).

The internal organisation of the mineral is specified in terms of **microscopic end-members**. The majority of minerals in the Holland and Powell (2011) dataset do not have an internal organisation like order-disorder and so the microscopic end-member can be considered as macroscopic (see below). However others, such as ilmenite, have order-disorder to be considered.

Macroscopic end-members have an equilibrium internal organisation as a function of P–T. Ilmenite has a composition of $FeTiO_3$, with Fe^{2+} and Ti cations partitioned between alternating layers within an oxygen sub-lattice (Harrison, Becker & Redfern, 2000). At temperatures above the critical temperature (here T_c), cations are distributed randomly over both layers (disordered) while below T_c, the cations are progressively ordered into Fe^{2+}- and Ti layers (A and B respectively) to lower temperature. Ilmenite is a macroscopic end-member if its constituent microscopic end-members, ordered ilmenite (oilm)and disordered ilmenite (dilm), are in equilibrium proportion. For example, at higher temperatures a more disordered ilmenite will be in equilibrium. Macroscopic end-members have a changing order parameter (here Q) as a function of P–T.

Mineral composition is represented in terms of **compositional end-members**. These end-members have a specified composition, however their internal organisation and structure remain unspecified.

3.3.1 Unary ilmenite

For ilmenite, there are two microscopic end-members, here being;

1. the ordered ilmenite, oilm
$$\mathrm{Fe^A\,Ti^B\,O_3}$$
2. and the disordered ilmenite, dilm
$$\mathrm{Fe^A_{\frac{1}{2}}\,Ti^A_{\frac{1}{2}}\,Fe^B_{\frac{1}{2}}\,Ti^B_{\frac{1}{2}}}$$

The superscript show the site that the element is occupying and the subscript denotes the proportion of that element on the site. oilm has $Fe^{2+}$and Ti distributed on the A site and B site respectively, while in dilm, $Fe^{2+}$and Ti are split evenly between the two sites. Microscopic end-members have a fixed order parameter, Q (see next, and Figure 3.1).

In a two-site mineral such as ilmenite, the order parameter may be defined as (following Holland & Powell, 1996b),
$$Q = X^{\mathrm{A}}_{\mathrm{Fe^{2+}}} - X^{B}_{\mathrm{Fe^{2+}}} \tag{3.1}$$
where $X^{\mathrm{A}}_{\mathrm{Fe^{2+}}}$ is the proportion of Fe^{2+} on the A site (see Figure 3.1).

Before investigating the common substitutions within the mineral, the thermodynamics of ilmenite need to be represented in terms of its microscopic end-members (oilm–dilm) before it is combined with more complex end-members involving substitution reactions (see binary and quaternary ilmenite sections below).

Mass balance reactions are written as:

$$X^{\mathrm{A}}_{\mathrm{Fe^{2+}}} + X^{\mathrm{B}}_{\mathrm{Fe^{2+}}} = 1 \tag{3.2}$$
$$X^{\mathrm{A}}_{\mathrm{Ti}} + X^{\mathrm{B}}_{\mathrm{Ti}} = 1 \tag{3.3}$$
$$X^{\mathrm{A}}_{\mathrm{Fe^{2+}}} + X^{\mathrm{A}}_{\mathrm{Ti}} = 1 \tag{3.4}$$
$$X^{\mathrm{B}}_{\mathrm{Fe^{2+}}} + X^{\mathrm{B}}_{\mathrm{Ti}} = 1 \tag{3.5}$$

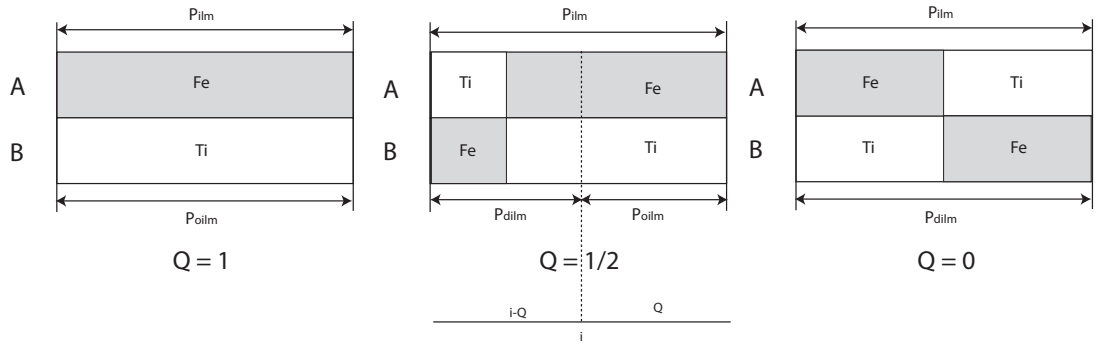

Figure 3.1. Site distributions and proportions for order–disorder in pure ilmenite. At $Q = 1$, ilmenite is fully ordered while at $Q = 0$, ilmenite is disordered. $\mathrm{P_{ilm}}$ refers to the proportion of the macroscopic end-member ilm, with $\mathrm{P_{ilm}} = 1$ in all such diagrams. $\mathrm{P_{oilm}}$ and $\mathrm{P_{dilm}}$ refer to the proportion of the microscopic end-members oilm and dilm respectively which vary with site occupancy.

Accordingly, the proportions of microscopic end-members within unary ilmenite as a function of the order parameter Q and the distribution of elements within the lattice are given as follows (see also Figure 3.1):

Proportions of end-members:

$$\begin{aligned} P_{\mathrm{oilm}} &= Q \\ P_{\mathrm{dilm}} &= 1 - Q \end{aligned}$$

Site distributions:

$$\begin{aligned} X^{\mathrm{A}}_{\mathrm{Fe^{2+}}} &= \tfrac{1}{2} + \tfrac{1}{2}Q \\ X^{\mathrm{A}}_{\mathrm{Ti}} &= \tfrac{1}{2} - \tfrac{1}{2}Q \\ X^{\mathrm{B}}_{\mathrm{Fe^{2+}}} &= \tfrac{1}{2} - \tfrac{1}{2}Q \\ X^{\mathrm{B}}_{\mathrm{Ti}} &= \tfrac{1}{2} + \tfrac{1}{2}Q \end{aligned}$$

3.3.2 Ilmenite-hematite binary

Ilmenite and hematite (Fe_2O_3) form a solid solution formed by the coupled substitution $2Fe^{3+} = Fe^{2+} + Ti^{4+}$. Partitioning of Fe and Ti onto alternating layers creates a cation-ordering phase transition through the space group $R\bar{3}$ to $R\bar{3}c$ at a tricritical point at the top of the solvus (see below). Through cooling, a loss of symmetry occurs and causes the formation of fine–scale twin domains (Harrison & Redfern, 2001). The assumption that there is no long-range ordering of Fe^{3+} over the A and B layers is supported by analysis of Burton, Chaka and Singh (2005).

As with unary ilmenite, the site structure of the solid-solution ilmenite–hematite can be considered with proportions of end-members and through site distributions (Figure 3.2). Note that the mole fraction of hematite is denoted by $1 - i$ with i the mole fraction of ilmenite.

Mass balance relations are written as:

$$X^{\mathrm{A}}_{\mathrm{Fe^{2+}}} + X^{\mathrm{B}}_{\mathrm{Fe^{2+}}} = i \tag{3.6}$$

$$X^{\mathrm{A}}_{\mathrm{Ti}} + X^{\mathrm{B}}_{\mathrm{Ti}} = i \tag{3.7}$$

$$X^{\mathrm{A}}_{\mathrm{Fe^{3+}}} + X^{\mathrm{A}}_{\mathrm{Fe^{2+}}} + X^{\mathrm{A}}_{\mathrm{Ti}} = 1 \tag{3.8}$$

$$X^{\mathrm{B}}_{\mathrm{Fe^{3+}}} + X^{\mathrm{B}}_{\mathrm{Fe^{2+}}} + X^{\mathrm{B}}_{\mathrm{Ti}} = 1 \tag{3.9}$$

The proportions of the end-members are:

$$\begin{aligned} P_{\text{oilm}} &= Q \\ P_{\text{dilm}} &= i - Q \\ P_{\text{hem}} &= 1 - i \end{aligned}$$

the site distributions are:

$$\begin{aligned} X^{\text{A}}_{\text{Fe}^{2+}} &= \tfrac{1}{2}i + \tfrac{1}{2}Q \\ X^{\text{A}}_{\text{Ti}} &= \tfrac{1}{2}i - \tfrac{1}{2}Q \\ X^{\text{B}}_{\text{Fe}^{2+}} &= \tfrac{1}{2}i - \tfrac{1}{2}Q \\ X^{\text{B}}_{\text{Ti}} &= \tfrac{1}{2}i + \tfrac{1}{2}Q \\ X^{\text{A}}_{\text{Fe}^{3+}} &= 1 - i \\ X^{\text{B}}_{\text{Fe}^{3+}} &= 1 - i \end{aligned}$$

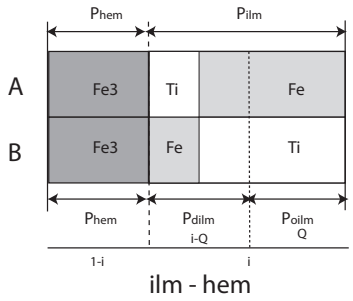

Figure 3.2. Site distributions and proportions of microscopic and compositional end-members for a given proportion of the ilmenite–hematite binary solid solution. P_{ilm} and P_{hem} refers to the proportion of the macroscopic end-members ilm and hem respectively, and P_{oilm} and P_{dilm} refers to the proportion of the microscopic end-members oilm and dilm respectively.

Tricritical point and the resulting solvus

An important constraint on the energetics of the ilmenite–hematite solid solution is the temperature and compositional dependent phase transition between ordered and disordered ilmenite. At high temperature the structure of the solid solution is disordered, with randomly distributed cations of Fe^{2+} and Ti^{4+} across the A and B sites ($R\bar{3}c$ where the A and B sites are symmetrically identical). At lower temperatures, the configurational entropy of the solution is lowered, and the Fe^{2+} and Ti^{4+} cations are ordered over the A and B sites ($R\bar{3}$ where the A and B sites are symmetrically distinct) (Ghiorso & Evans, 2008). The transition between the ordered space group $R\bar{3}$ and the disordered space group $R\bar{3}c$ occurs at a critical temperature (here T_c). This is an example of *convergent* cation-ordering where the phases can go from complete order to complete disorder. The solvus intersects the $R\bar{3}$ to $R\bar{3}c$ transition at a tricritical point (see Figure 3.3).

Previous work

Previous work on calculating the solvus in the ilmenite–hematite binary includes Monte Carlo simulations conducted by Harrison, Becker and Redfern (2000) to study order–disorder in ilmenite–hematite solid solution. This technique reproduces changing phase transitions by handling Fe^{2+}–Ti and Fe^{3+}–Ti interactions separately in each simulation. A tricritical point where the phase transition intersects a low–temperature miscibility gap occurs at $i(\text{ilm}) = 0.6$ and $T = 1073\,\text{K}$ (800°C), though it is highlighted that due to the small size of the Monte Carlo simulation cell, the temperature is likely to be overestimated. Ghiorso (1990, 1997) predict the position of the tricritical point to be at $i(\text{ilm}) = 0.55$ and $T = 1023\,\text{K}$ (750°C), in similar agreement with Harrison,

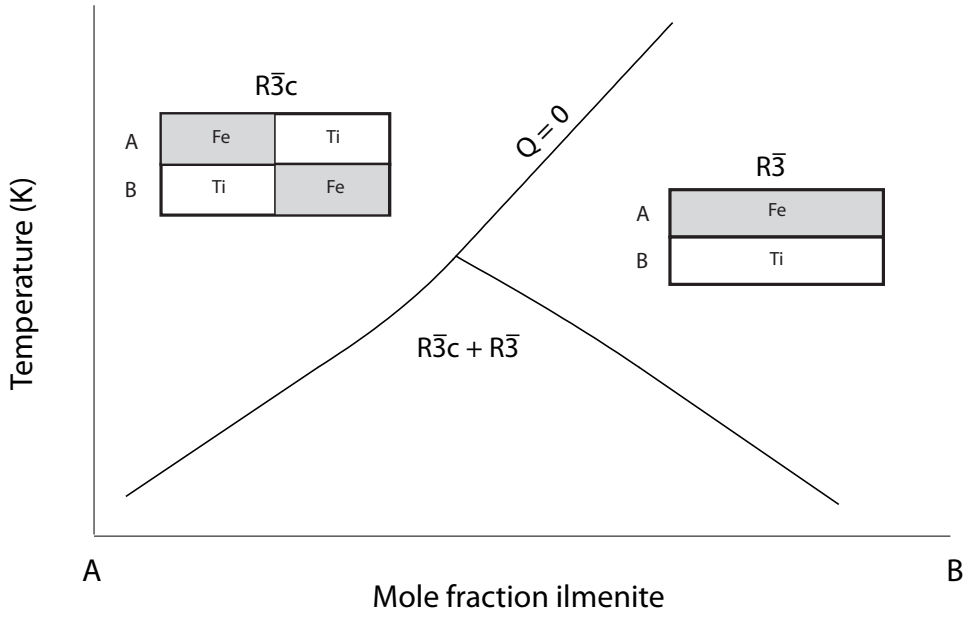

Figure 3.3. A schematic phase diagram (T(K)-i) for the Fe_2O_3–FeTiO system. A tricritical point for the ilmenite–hematite solid solution is formed from the intersection of the R$\bar{3}$ to R$\bar{3}$c transition with a low–temperature miscibility gap. At lower mole fractions of ilmenite, and at higher temperatures, ilmenite is disordered. At higher mole fractions of ilmenite and lower temperatures, ilmenite is ordered. The trace of Q = 0 represents the critical temperature (T_c) for each proportion of ilmenite.

Becker and Redfern (2000). Earlier theoretical studies by Burton (1984, 1985) place the tricritical point at the lower temperature of 987 K (714°C) and at $i(\text{ilm}) = 0.5$.

Of note is that solvi are highly sensitive to the thermodynamics. The Monte Carlo simulations are a forward modelling approach and the possibility for inaccuracy may be significant given that the precise setup of the simulations affects the results. The Ghiorso (1990, 1997) estimate of the solvus is a result of the assumptions made in formulating and calibrating the thermodynamics. An estimate for the tricritical point and resulting solvus using the preferred symmetric formalism approach is developed further in this chapter (Figure 3.9).

3.3.3 Ordering parameters

The aim of a thermodynamic description for the ilmenite–hematite solid solution is to accurately describe the enthalpy and entropy of the solid solution. As previously discussed, the prediction of phase transitions between ordered and disordered ilmenite as a function of temperature is crucial. This type of ordering is called 'long-range ordering'. In addition, a degree of 'short-range ordering' can affect the configurational entropy of the system when there is an interaction between nearest-neighbor cation occupancies.

Long-range ordering

In a mineral such as ilmenite showing cation order–disorder, there are s independent long-range order parameters which are required to describe the state of order. In an n–component system, there is a solid solution between an independent set of $n + s$ microscopic end-members.

For the binary system ilmenite–hematite, $n = 2$, so there are two compositional end-members $FeTiO_3$ and Fe_2O_3. The thermodynamic dataset includes the macroscopic end-member ilmenite involving cation order–disorder. This order–disorder is between oilm and dilm, so there is one order parameter, Q, represented by dilm. The final microscopic end-member of macroscopic ilmenite is oilm. This completes the set of independent microscopic end-members ($n + s = 3$). Figure 3.4 shows these relationships.

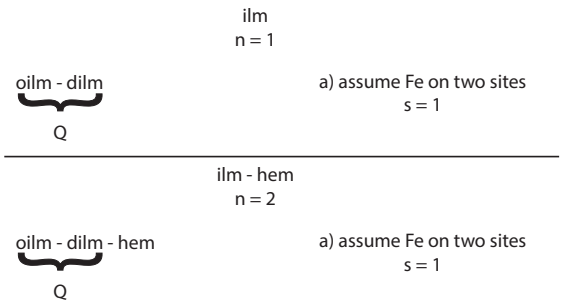

Figure 3.4. Explanation of the number of s independent order parameters to describe the state of order in an n–component system for pure ilmenite as well as a system expansion to solid solutions with hematite. Ilmenite has two microscopic end-members as it is a one-component system with one long-range order parameter assuming Fe on two sites. Ilmenite–hematite has three microscopic end-members as it is a two-component system, however there is only one long-range order parameter as Fe partitions into both the A and B sites equally.

Quantifying n is a geological choice relating to the substitutions in mineral structure. However, s is a microscopic choice relating to the chosen distribution of the elements between the sites, and controlled by internal equilibrium).

For a mineral to be completely ordered, $Q = 1$. Complete disorder corresponds to $Q = 0$. As the temperature increases, ilmenite becomes increasingly disordered. The temperature at which a mineral is completely disordered is termed the critical temperature (T_c). Minerals that are said to be 'non–convergent' cannot reach complete disorder. Cation ordering in ilmenite involves a change in symmetry of the crystal lattice, termed 'convergent' ordering (see above discussion on the tricritical point)

For the solid solution between ilmenite and hematite, the assumption is made that Fe^{3+} partitions into the A and B layers equally. When $Q = 1$, the solid solution is completely ordered with a mixture of Fe^{2+} and Fe^{3+} on the A site, and a mixture of Ti and Fe^{3+} on the B site. In later sections, the thermodynamic description expands to include long-ranger order in the Mg- and Mn-bearing TiO_3 end-members (geikielite–pyrophanite, Q_g and Q_m respectively).

Short-range ordering

In addition to long–range order, short–range order between cations is likely to be involved. Short–range order (SRO), as discussed in Powell and Holland (1993), involves the nearest–neighbour correlations between cation site occupancies. With no SRO, the probability of a Ti–Ti pair occurring on adjacent A–layer and B–layer sites is equal to the product of the concentration of Ti on the A- and B- layers. When there is full SRO, the probability is zero, and there is complete nearest–neighbour Ti–Ti avoidance (Harrison & Redfern, 2001).

As discussed in Powell and Holland (1993) commonly used a–x models use mixing-on-sites for the configurational entropy contribution to the energetics, and an *independent* enthalpic contribution via interaction energies. This is only an approximation, excluding SRO, but there are no existing models that adequately account for SRO. A crude, commonly-used way for accounting for SRO is by a proportional reduction in the configurational entropy term, as done for example in White, Powell, Holland, Green et al. (2014) for the tetrahedral site mixing in the pyroxenes.

3.3.4 Pressure dependence

The neutron diffraction experiments undertaken by Harrison, Becker and Redfern (2000) were performed under vacuum and thus the thermodynamic calculations in the study were restricted to zero pressure. A later study in 2006 (see Harrison, Stone & Redfern, 2006) finds that the degree of cation order is observed to increase with pressure, affecting the point at which the critical temperature for ilmenite is reached as a function of pressure. The new, higher pressure experiments were performed on a synthetic sample of $(FeTiO_3)_{0.65}(Fe_2O_3)_{0.35}$ at $T \leq 933$°C and $P \leq 0.64$ GPa and revealed an increase in the critical temperature from 911°C at atmospheric pressure to 1010°C at P = 0.64 GPa, with the the assumption that the observed increase of 100°C is caused by increased cation–cation interaction. For results relating to pressure dependence on the degree of cation order see Figure 3.10 later in the chapter.

3.3.5 A note on magnetic ordering

Burton (1984, 1985) calculated that below ≈550°C there is a 'magnetic' miscibility gap in the ilmenite–hematite series which would, for example, influence Fe–Ti oxide geothermometry significantly. It follows that for petrological accuracy, magnetic ordering should be included into thermodynamic models. However as this study is conducted above this temperature, modelling will only take into account chemical ordering while low temperature magnetic behaviour will be ignored.

3.3.6 Summary

The ilmenite structures considered to this point are unary ilmenite (allowing for order–disorder of Fe^{2+} and Ti on the A and B site) and the binary ilmenite–hematite binary solid solution (assuming no order–disorder of Fe^{3+}). Microscopic end-members specify internal organisation – oilm and dilm – which refer to fully ordered and disordered ilmenite respectively. A macroscopic end-member has an equilibrium internal organisation, and has an order parameter, Q, a function of P–T. Microscopic end-members have a specified composition and internal organisation and structure. The effects of short-range order and magnetic ordering have been assumed to be negligible for the temperatures of interest, however the degree of long-range cation order with changing pressure will be discussed.

3.4 Modelling approach

In order to create a more geologically realistic activity–composition model for ilmenite, such model must be parameterised in a multi-component system and calibrated using experimental data. This requires transforming the formulation of the ilmenite model from an insufficient approach ('Landau'), into symmetric formalism; calculating the macroscopic interaction energies corresponding to within-site and cross-site terms; and using recent experimental data on cation order and temperature to constrain the terms required to create a complete thermodynamic description of the ilmenite–hematite solid solution.

3.4.1 Landau and symmetric formalism

Programs such as THERMOCALC, Theriack Domino (de Capitani & Petrakakis, 2010), and PerpleX (Connolly, 1990) use the information within the Holland and Powell (2011) dataset to calculate the equilibrium state of order at specified P and T for macroscopic end-members.

In the dataset (Holland & Powell, 2011), the configurational order–disorder in ilmenite is currently parameterised by **Landau theory** (Powell et al., 2014). Landau theory is often used for macroscopic end-members which display magnetic ordering, configurational ordering and rotational ordering, however it becomes less well-defined when generalising to multi-component systems ($n > 1$).

While Landau theory is used to parameterise some macroscopic end-members, others are calculated in terms of the **symmetric formalism**, which can be used to generalise to multi-component systems (Holland & Powell, 1996a; Powell & Holland, 1993). The symmetric formalism is identical in form to the generalised Bragg-Williams models for convergent ordering (e.g. Holland & Powell, 1996a; Sack, 1980; Thompson, 1967).

In the *symmetric formalism*, the enthalpy of ordering between the disordered and ordered state as a function of Q is given by;

$$\Delta H_{\mathrm{SF}}^{\mathrm{ord}} = Q\,(W - \Delta H_{\mathrm{R}}) - Q^2\,W \tag{3.10}$$

where ΔH_{R} is the standard enthalpy of the reaction oilm = dilm. As ilmenite shows convergent ordering, $W = \Delta H_{\mathrm{R}}$,where W is the macroscopic interaction energy for the binary oilm and dilm.

In *Landau theory*, the Gibbs energy of ordering is given by a series expansion in the order parameter Q;

$$\Delta H_{\mathrm{Landau}}^{\mathrm{ord}} = -H\,Q - \frac{1}{2}\,a\,T_{\mathrm{c}}\,Q^2 + \frac{1}{4}\,b\,Q^4 + \frac{1}{6}\,c\,Q^6 \ldots \tag{3.11}$$

where a and b and c are constants for a given composition, and n is an even integer required by symmetry (Harrison, Becker & Redfern, 2000; Holland & Powell, 1996a). Values for a, b, c are derived from fitting experimental data. The field term H allows for the possibility of non-convergent ordering. For the purposes here, H is zero, as ilmenite undergoes convergent ordering. Differences in the heat capacity behaviour with experiments fitted to Landau theory result from the higher order terms in Equation 3.11 compared to Equation 3.10. These higher polynomials (e.g. in Q^6) produce a sharp gradient in heat capacity and more pronounced curvature in Q–T relationships.

Currently, in Holland and Powell (2011) **ds62**, ilmenite is parameterised by Landau theory, using a critical temperature T_c of 1900°C for pure ilmenite; S_{max} of 12.00 and a V_{max} of 0.0200. With ilmenite exhibiting order–disorder in solid solution, the Landau approach does not adequately fit the heat capacity behaviour exhibited by the solid solution as it does not incorporate the configuration entropy associated with cation ordering. The new dataset has endeavoured to update the parameterisation of end-members exhibiting solid solution, such as sillimanite, gehlenite, cordierite, albite, K-feldspar, anorthite, spinel, hercynite, dolomite, and ankerite, into the symmetric formalism model, however ilmenite remains in Landau.

One step in creating a thermodynamic description for the ilmenite–hematite solid solution is to *remove* the effect of the Landau representation of the long-range order and *replace* it with an equivalent symmetric formalism formulation (Holland & Powell, 1996a). The difference in energetics between the symmetric formalism and Landau theory when applied to experimental data is small (as per Landau second–order and Landau tricritical behaviour in Figure 3 in Holland & Powell, 1996a). After replacing Landau by symmetric formalism, ilmenite end-members can be combined properly with the other end-members and will allow the ilmenite end-members to be constructed incorporating configurational entropies and activity–composition expressions.

3.4.2 a–x formulation

Gibbs Energy is made up of a mechanical mixing term, an entropic term, and an enthalpic term, where the entropic and enthalpic terms are taken to be uncorrelated (Powell & Holland, 1993). The entropic part is written as ideal mixing on sites, where a decision as to what elements reside on what sites is made. Once a decision is reached, the entropic part is completely specified. The enthalpic part is written using the symmetric formalism (Holland & Powell, 1996b) to describe the interactions between elements on each site.

In each i–j binary, there is a **macroscopic interaction energy**, $W_{\mathrm{i\,j}}$, corresponding to within-site and cross-site terms (Powell & Holland, 1993). For a complete thermodynamic description of the ilmenite–hematite solid solution handled using symmetric formalism, $W_{\mathrm{oilm\,dilm}}$, $W_{\mathrm{dilm\,hem}}$ and $W_{\mathrm{oilm\,hem}}$ must be constrained. Combining this binary system with geikielite (Mg end-member, $MgTiO_3$) and pyrophanite (Mn end-member, $MnTiO_3$), new values for $W_{\mathrm{oilm\,ogeik}}$, $W_{\mathrm{oilm\,dgeik}}$, $W_{\mathrm{oilm\,opnt}}$, $W_{\mathrm{oilm\,dpnt}}$, $W_{\mathrm{dilm\,ogeik}}$, $W_{\mathrm{dilm\,dgeik}}$, $W_{\mathrm{dilm\,opnt}}$, $W_{\mathrm{dilm\,dpnt}}$, $W_{\mathrm{hem\,ogeik}}$, $W_{\mathrm{hem\,dgeik}}$, $W_{\mathrm{hem\,opnt}}$, $W_{\mathrm{hem\,dpnt}}$, $W_{\mathrm{ogeik\,dgeik}}$, $W_{\mathrm{ogeik\,opnt}}$, $W_{\mathrm{ogeik\,dpnt}}$, $W_{\mathrm{dgeik\,opnt}}$, $W_{\mathrm{dgeik\,dpnt}}$, and $W_{\mathrm{opnt\,dpnt}}$ must also be evaluated.

Symmetry rules state that the microscopic interaction energy between elements on the A site is equal to the microscopic interaction energy between the same elements on the B site. The same is true for cross-site terms.

Experimental work

The first parameters that must be solved involve order–disorder within unary ilmenite, where Fe is assumed to mix between two sites. Experiments by Harrison, Becker and Redfern (2000), Harrison and Redfern (2001), Harrison, Redfern and Smith (2000) allow calculation of a revised $W_{\mathrm{oilm\,dilm}}$ and thus a determination of the internal energy involved in the equilibrium statement oilm=dilm. Using this value, a high-temperature solvus for the ilmenite–hematite solid solution can be devised. This leads to new interaction energies between oilm–hem and dilm–hem.

3.4.3 Summary

A new thermodynamic description of the ilmenite–hematite solid solution must be parameterised in symmetric formalism in order to be used in modeling a geological realistic multi-component system. This will involve removing the effect of Landau on long-range order and replacing with the equivalent symmetric formalism. Order–disorder experimental work on the ilmenite–hematite solid solution will help constrain the model and estimate answers to the following;

- what is the critical temperature for pure ilmenite?
- where is the top of the ilmenite-hematite solvus?
- what are the interaction energies in the ilmenite–hematite–geikielite–pyrophanite system?

3.5 Constraining experimental data

3.5.1 ilmenite

Calculating the critical temperature for pure ilmenite

Harrison, Becker and Redfern (2000), Harrison, Redfern and Smith (2000) and Harrison and Redfern (2001) conducted time-of-flight neutron diffraction studies of the ilmenite–hematite solid solution at temperatures up to 1300°C and over a compositional range of i(ilm) of $0.6 < i \leq 1$. Table 2 of the supplementary material (deposit #AM-00-033) from Harrison, Redfern and Smith (2000) and Table 3 from Harrison and Redfern (2001) provide Q_h values as a function of temperature for varying ilmenite compositions (i) in the $(FeTiO_3)_i(Fe_2O_3)_{1-i}$ solid solution. The results of these experiments are in Table 3.3 of this chapter. The experiments found that the degree of order decreased smoothly at high temperatures with decreasing i. Critical temperatures (T_c where Q or $_h = 0$ for each proportion of ilmenite i) are 818, 918, 1000, 1175, 1325°C for ilm60, ilm 65, ilm70, ilm80, and ilm90 respectively.

Harrison, Becker and Redfern (2000) define the long-range interlayer order parameter, Q_h as:

$$Q_h = \frac{X^{\mathrm{B}}_{\mathrm{Ti}} - X^{\mathrm{A}}_{\mathrm{Ti}}}{X^{\mathrm{B}}_{\mathrm{Ti}} + X^{\mathrm{A}}_{\mathrm{Ti}}} \tag{3.12}$$

Q_h is used by Harrison so that the ordered ilmenite in any proportion with hematite has a Q_h of 1. Here, the Q_h values are normalised with the proportion of ilmenite in the ilmenite–hematite solution, conforming to the order parameter definition in Equation 3.1. These data have been extracted (Table 3.3) and the Q_h value adjusted for each composition of ilmenite (i) using:

$$Q = i\,Q_{\mathrm{h}}\,, \tag{3.13}$$

in order to align with the Q definition in Equation 3.1 following Holland and Powell (1996b).

Table 3.3. Results of time-of-flight neutron diffraction studies of the ilmenite–hematite solid solution at temperatures up to 1300°C and over a compositional range of i(ilm) of $0.6 < i \leq 1$ by Harrison, Becker and Redfern (2000) and Harrison and Redfern (2001). Original Q_h values are calculated as a function of temperature for varying ilmenite compositions. Q_h is normalised to i(ilm) and converted to Q for this study. The temperature where $Q = 0$ is the critical temperature for each proportion of ilmenite. Q–T(°C) results are displayed in Figure 3.5 (black circles).

T(°C)	Q_h	T(K)	Q	T(°C)	Q_h	T(K)	Q	T(°C)	Q_h	T(K)	Q
ilm60				**ilm65**				**ilm70**			
697	0.64	970.15	0.416	697	0.763	970.15	0.4578	700	0.829	973.15	0.5803
721	0.59	994.15	0.3835	745	0.726	1018.15	0.4356	750	0.803	1023.15	0.5621
745	0.537	1018.15	0.34905	794	0.649	1067.15	0.3894	800	0.769	1073.15	0.5383
769	0.463	1042.15	0.30095	818	0.594	1091.15	0.3564	850	0.706	1123.15	0.4942
793	0.36	1066.15	0.234	843	0.52	1116.15	0.312	900	0.614	1173.15	0.4298
818	0	1091.15	0	868	0.415	1141.15	0.249	925	0.546	1198.15	0.3822
844	0	1117.15	0	893	0.283	1166.15	0.1698	950	0.454	1223.15	0.3178
921	0	1194.15	0	918	0	1191.15	0	975	0.314	1248.15	0.2198
999	0	1272.15	0	945	0	1218.15	0	1000	0	1273.15	0
				994	0	1267.15	0	1025	0	1298.15	0
								1050	0	1323.15	0
								1100	0	1373.15	0
ilm80				**ilm90**				**ilm100**			
700	0.937	973.15	778.52	700	0.971	973.15	0.8739	700	0.976	973.15	0.976
800	0.912	1073.15	858.52	800	0.958	1073.15	0.8622	800	0.976	1073.15	0.976
900	0.873	1173.15	938.52	900	0.94	1173.15	0.846	900	0.972	1173.15	0.972
1000	0.757	1273.15	1018.52	1000	0.913	1273.15	0.8217	1000	0.964	1273.15	0.964
1100	0.57	1373.15	1098.52	1100	0.869	1373.15	0.7821	1100	0.95	1373.15	0.95
1150	0.267	1423.15	1138.52	1150	0.831	1423.15	0.7479	1200	0.9	1473.15	0.9
1175	0	1448.15	1158.52	1200	0.771	1473.15	0.6939	1250	0.86	1523.15	0.86
1200	0	1473.15	1178.52	1225	0.731	1498.15	0.6579	1300	0.794	1573.15	0.794
1225	0	1498.15	1198.52	1250	0.68	1523.15	0.612	1325	0.732	1598.15	0.732
1250	0	1523.15	1218.52	1275	0.538	1548.15	0.4842				
1275	0	1548.15	1238.52	1300	0.322	1573.15	0.2898				
1300	0	1573.15	1258.52	1325	0	1598.15	0				
1325	0	1598.15	1278.52	1350	0	1623.15	0				

The degree of cation–ordering, Q, as a function of temperature (°C) from Table 3.3 is plotted in Figure 3.5 as black circles.

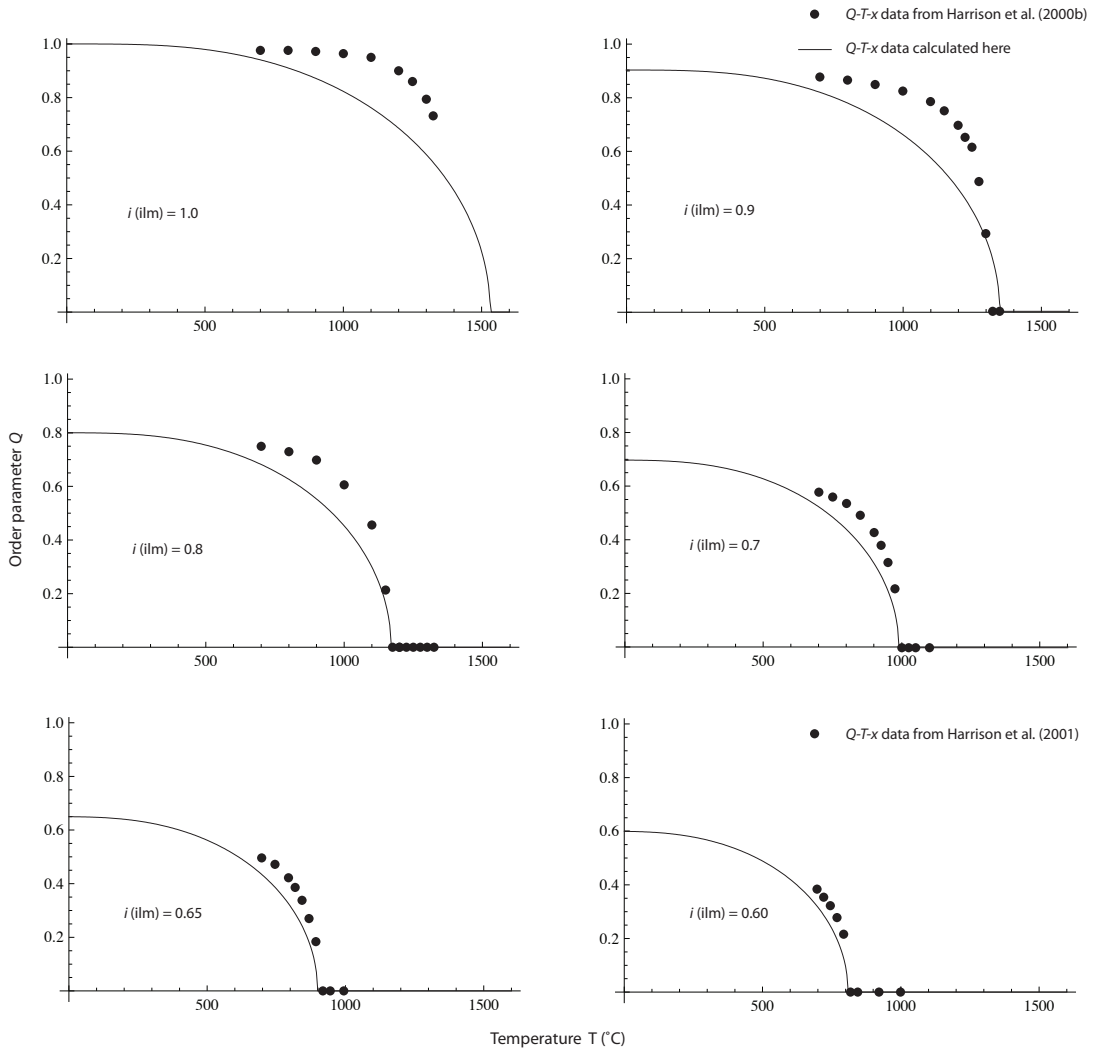

Figure 3.5. Q–T(°C) plots for different proportions of ilmenite. Black dots are experimental data from Table 3.3, Harrison, Redfern and Smith (2000) and Harrison and Redfern (2001), fitted to a fourth-order Landau theory polynomial (Equation 3.11). Solid lines are the same data fitted to symmetric formalism (Equation 3.23). The critical temperature for each proportion of ilmenite occurs at $Q = 0$ (convergent ordering).

Pure ilmenite where i(ilm) = 1 does not record a phase transition as the experiment did not reach the temperature required for complete disorder. By finding the average temperature for complete disorder for other proportions of ilmenite, the critical temperature (in Kelvin, Q = 0) for pure ilmenite can be estimated according to

$$T_{\mathrm{c}} = a\, i \tag{3.14}$$

where a is a constant. Figure 3.6 shows a for each ilmenite proportion, with an average value of $a = 1800$. The linear relationship between T_c and the proportion of ilmenite is also shown, and shows the critical temperature for pure ilmenite to be 1800K according to Equation 3.14 (with $a = 1800$ and $i = 1$). Therefore, using the data from Harrison, Redfern and Smith (2000) and Harrison and Redfern (2001) this has shown that pure ilmenite undergoes a change in symmetry from R$\bar{3}$ to R$\bar{3}$c at a critical temperature at 1800K (1526°C). This is similar to an estimate by Burton (1985)

and Harrison, Redfern and Smith (2000) who conclude the transition temperature is close to 1673 K (1400°C).

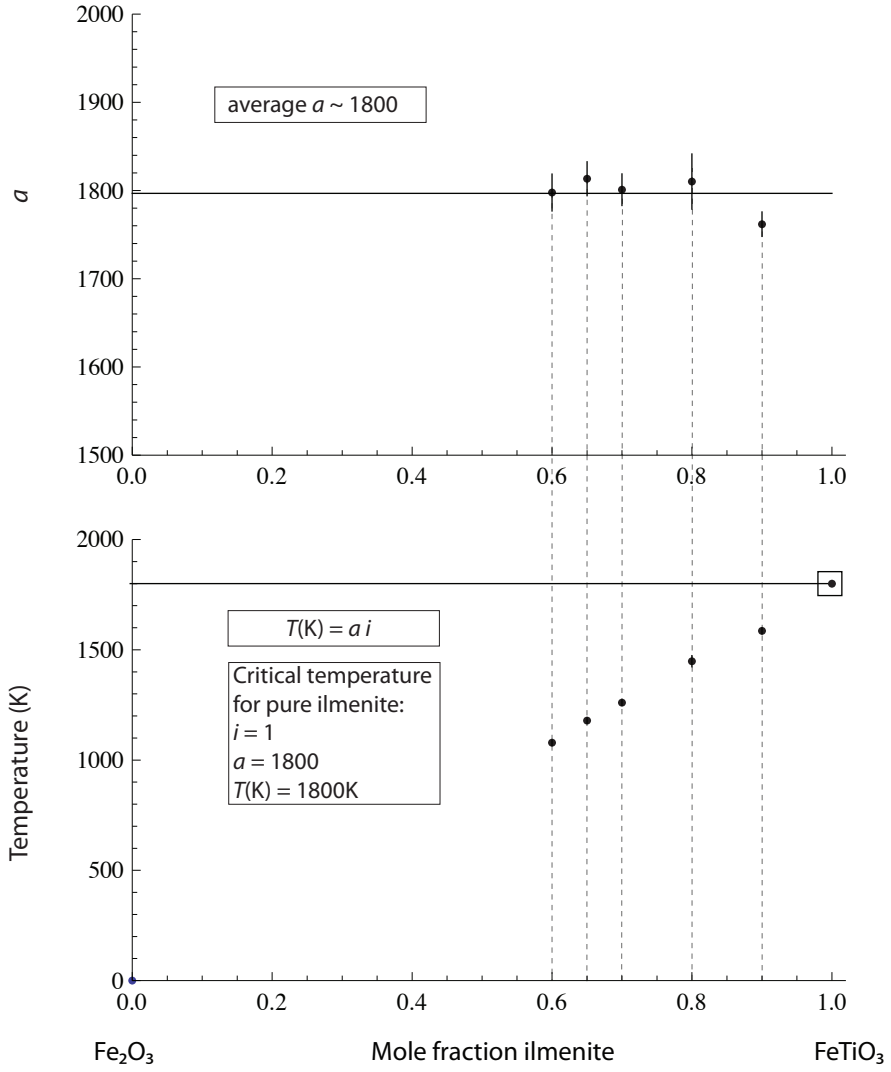

Figure 3.6. Relationship between a, i and T_c. An average a was calculated from the five ilmenite proportions (top) and then used in the function $T_c = a\ i$ to extrapolate a critical temperature for pure ilmenite (square box; bottom).

Calculating the interaction energy between ordered and disordered ilmenite

The ideal mixing-on-sites (as per Holland & Powell, 1996a) give the activities of the end-members as such:

$$\alpha_{\text{oilm}}^{\text{ideal}} = X_{\text{Fe}}^{\text{A}} X_{Ti}^{B} = \frac{1}{4}(1+Q)^2$$
$$\alpha_{\text{dilm}}^{\text{ideal}} = 4(X_{\text{Fe}}^{\text{A}}\, X_{Ti}^{\text{A}}\, X_{\text{Fe}}^{B}\, X_{Ti}^{B})^{1/2} = (1+Q)(1-Q) \tag{3.15}$$

where 4 is a normalisation constant so that dilm is completely disordered, and $\frac{1}{2}$ is an exponential because Fe and Ti each occupy half a site within the disordered end-member. The activity coeffi-

cients are given by the expression for a regular solution (Equation 2.15) (Powell, 1978; Thompson, 1967);

$$\begin{aligned} \mathrm{R}T \ln \gamma_{\mathrm{oilm}} &= W_{\mathrm{oilm\,dilm}}(1-P_{\mathrm{oilm}})^2 = W_{\mathrm{oilm\,dilm}}(1-Q)^2 \\ \mathrm{R}T \ln \gamma_{\mathrm{dilm}} &= W_{\mathrm{oilm\,dilm}}(1-P_{\mathrm{dilm}})^2 = W_{\mathrm{oilm\,dilm}}Q^2 \end{aligned} \tag{3.16}$$

To find the equilibrium value of Q at any temperature, the reaction between ordered and disordered ilmenite can be used;

$$\mathrm{Fe^A Ti^B O_3\,(oilm)} = \mathrm{Fe^A_{\frac{1}{2}} Ti^A_{\frac{1}{2}} Fe^B_{\frac{1}{2}} Ti^B_{\frac{1}{2}} O_3\,(dilm)} \tag{3.17}$$

for which the equilibrium relation is:

$$\mu_{\mathrm{oilm}} = \mu_{\mathrm{dilm}} \tag{3.18}$$

At equilibrium the $\Delta\mu$ is zero, for which the equilibrium condition is:

$$\Delta\mu = 0 = \Delta G^0 + \mathrm{R}T \ln K \tag{3.19}$$

Substituting the activities from Equations 3.15 into the equilibrium condition in Equation 3.19 gives

$$\begin{aligned} 0 &= \Delta H_{\mathrm{R}} - T\Delta S_{\mathrm{R}} + P\Delta V_{\mathrm{R}} + \mathrm{R}T \ln \frac{1-Q}{1+Q} + \mathrm{R}T \ln 4 + (2Q-1)W_{\mathrm{oilm\,dilm}} \\ &= \mathrm{A} + BQ + \mathrm{R}T \ln \frac{1-Q}{1+Q} \end{aligned} \tag{3.20}$$

where $\mathrm{A} = \Delta H_{\mathrm{R}} - W_{\mathrm{oilm\,dilm}} + P\Delta V_{\mathrm{R}}$ and $\mathrm{B} = 2W_{\mathrm{oilm\,dilm}}$. The $-T\Delta S_{\mathrm{R}}$, which represents the difference in entropy between ordered and disordered ilmenite is cancelled by the activity of oilm (Equation 3.15) which contributes the factor $\frac{1}{4}$ in the form of $\mathrm{R}T \ln 4$. ΔV_R is here on assumed to be zero. The standard enthalpy of the reaction oilm = dilm, ΔH_{R}, represents the enthalpy difference between completely ordered and completely disordered ilmenite (Holland & Powell, 1996b). When $\Delta H_{\mathrm{R}} = W_{\mathrm{oilm\,dilm}}$, or $A = 0$, convergent behaviour occurs. Q rapidly decreases to zero at a critical temperature, T_c. This reduces the equation to the convergent Bragg-Williams model;

$$0 = B\,Q + \mathrm{R}T \ln \frac{1-Q}{1+Q} \tag{3.21}$$

Symmetric formalism is identical in form to the Bragg-Williams model (Holland & Powell, 1996a). Using symmetric formalism as a microscopic approach, ilmenite can be written in terms of regular solutions on the A and B sites (w^{A}, w^{B}) with a cross-site interaction energy ($w^{\mathrm{A,B}}_{\mathrm{cross-site}}$) representing the internal reaction $\mathrm{Fe^A\,Ti^B} = \mathrm{Ti^A\,Fe^B}$. Substituting the individual terms into the equilibrium condition $0 = \Delta G^0 + \mathrm{R}T \ln K$ gives;

$$\begin{aligned} 0 &= \frac{\Delta H_{ex}}{2} + \mathrm{R}T \ln \frac{1-Q}{1+Q} + \frac{(w^{\mathrm{A,B}}_{\mathrm{cross-site}} - w^{\mathrm{A}} - w^{\mathrm{B}})}{2}\,Q \\ &= \mathrm{A} + B\,Q + \mathrm{R}T \ln \frac{1-Q}{1+Q} \end{aligned} \tag{3.22}$$

which is identical in generalised form to Equation 3.20. In this expression, ΔH_{ex} is the enthalpy of exchange for the internal reaction $\mathrm{Fe^A Ti^B} = \mathrm{Ti^A Fe^B}$.

For convergent ordering, the relationship between the critical temperature and the macroscopic interaction energy for the binary ilm–hem is found by solving Equation 3.21 for temperature as

$Q \to 0$ (Appendix 2 Holland & Powell, 1996a). Starting with

$$0 = 2WQ + \mathrm{R}T \ln \frac{1-Q}{1+Q} \tag{3.23}$$

rearranging gives

$$T = -\frac{2\,WQ}{\mathrm{R} \ln \frac{1-Q}{1+Q}} \tag{3.24}$$

As $Q \to 0$

$$T_\mathrm{c} = T\,|_{Q\to 0} = -\left.\frac{\frac{\partial(2\,WQ)}{\partial Q}}{\frac{\partial\left(\mathrm{R} \ln \frac{1-Q}{1+Q}\right)}{\partial Q}}\right|_{Q\to 0} = \frac{W_{\mathrm{oilm\,dilm}}}{\mathrm{R}} \tag{3.25}$$

The energetics between ordered and disordered ilmenite can be calculated from this relation. Therefore, with ilmenite (ilm100) exhibiting convergent behaviour with a critical temperature at 1800K and substituting R = 0.0083144 kJ K^{-1}, the interaction energy between oilm and dilm ($W_{\mathrm{oilm\,dilm}}$) is = 15 kJ.

Landau to symmetric formalism

With $W_{\mathrm{oilm\,dilm}}$ = 15 kJ, an equilibrium expression for oilm = dilm can be determined by substituting this value into Equation 3.23. Therefore, to determine the equilibrium value of Q as a function of temperature for each proportion of ilmenite (i), we solve

$$0 = 30Q + \mathrm{R}T \ln \frac{i-Q}{i+Q}, \tag{3.26}$$

where i is the proportion of ilmenite. The resultant curve in Q–T fits the critical temperature predicted by the Harrison data to a symmetric formalism approach plotted in Figure 3.5.

The Harrison, Becker and Redfern (2000) Q–T curves follow a fourth-order polynomial using a least-squares approach to fit the data using the Landau theory. The Landau fitted Q–T curves (black dots) are plotted against Q–T values fitted for symmetric formalism (solid line) for which oilm = dilm, with the resulting plots compared in Figure 3.5. An ideal result would see the calculated Q–T curves fitting the experimental data. One of the largest differences is observed in the steepness of the data as ordering gets underway with decreasing T. The fourth order polynomial creates this gradient; a feature that is not possible with the symmetric formalism which only allows a second–order polynomial. While this discrepancy may appear large from an ordering aspect, the difference in energetics between the Landau and symmetric formalism data is small.

3.5.2 ilmenite–hematite binary system

Constraining values for the interaction energy between ordered ilmenite–hematite, and disordered ilmenite–hematite

The interaction energy between dilm and hem, $W_{\mathrm{dilm\,hem}}$, is constrained by the temperature of the top of the solvus. A tricritical point occurs at the temperature at which the top of the solvus is reached. Harrison, Becker and Redfern (2000) calculated a phase diagram for the Fe_2O_3-$FeTiO_3$ system with the $R\bar{3}$ to $R\bar{3}c$ transition intersecting the solvus at a tricritical point at T = 800 °C (1073.15K) at x = 0.6. The study notes that temperatures may be overestimated in the study due to the small size of the Monte Carlo simulation cell. Ghiorso (1990, 1997) predict a similar position of T= 750 °C (1023.15K) at x = 0.55. Both of these estimates are higher than Burton (1984, 1985) who predicts the transition to occur at T = 714°C (987.15K) at x = 0.5.

Plotting the linear relationship between the temperature of the top of the solvus and $W_{\mathrm{dilm\,hem}}$ (Figure 3.7), we can constrain the maximum and minimum values for $W_{\mathrm{dilm\,hem}}$ within the range of likely solvus temperatures (1023K, 1073K; Ghiorso, 1997; Harrison, Becker & Redfern, 2000).

This gives a maximum $W_{\mathrm{dilm\,hem}}$ of 14.61 kJ and a minimum $W_{\mathrm{dilm\,hem}}$ of 12.23 kJ. For simplicity, we will use use the rounded median of 13 kJ. This corresponds to a tricritical point of 1041.8K (768°C). Following the symmetric formalism setup, where $W_{\mathrm{oilm\,hem}} = W_{\mathrm{oilm\,dilm}} + W_{\mathrm{dilm\,hem}}$, this corresponds to values $W_{\mathrm{oilm\,dilm}} = 15$ kJ; $W_{\mathrm{oilm\,hem}} = 28$ kJ; $W_{\mathrm{dilm\,hem}} = 13$ kJ.

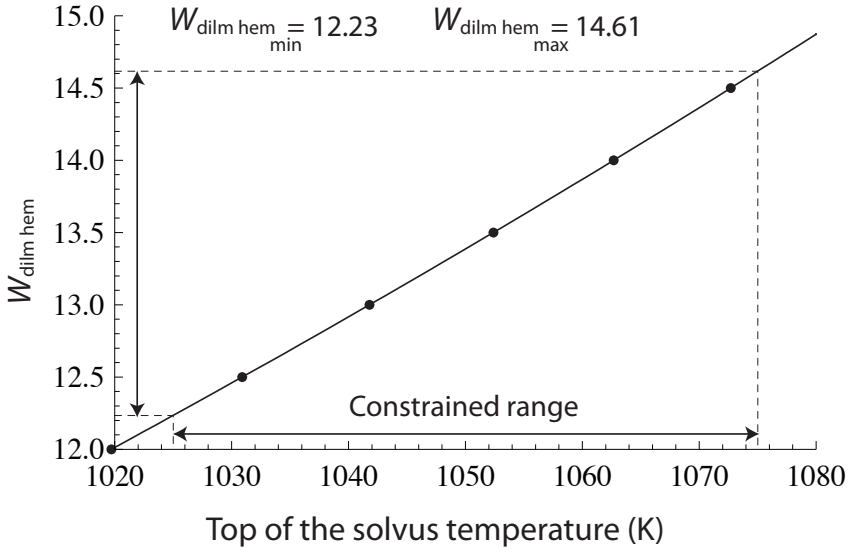

Figure 3.7. The linear relationship between the temperature of the top of the solvus for the ilmenite–hematite solid solution, and the interaction energy between disordered ilmenite and hematite. Previous temperature estimates for the top of the solvus (1023.15 and 1073.15K Ghiorso, 1997; Harrison, Becker & Redfern, 2000) constrain the maximum and minimum values of $W_{\mathrm{dilm\,hem}}$

.

Estimating the top of the solvus for the ilmenite–hematite solid solution

The top of the solvus ('tricritical point') for the ilmenite–hematite solid solution can be estimated in light of new experimental data in FTO by Harrison, Becker and Redfern (2000), Harrison, Redfern and Smith (2000). Using the new values of $W_{\mathrm{oilm\,dilm}} = 15$ kJ; $W_{\mathrm{oilm\,hem}} = 28$ kJ; $W_{\mathrm{dilm\,hem}} = 13$ kJ, a T–x diagram can be produced. The solvus can be calculated using the activity ratio:

$$f = \mathrm{R}T \ln \frac{a(\mathrm{ilm})}{a(\mathrm{hem})} \tag{3.27}$$

The aim is to find a value (see Figure 3.8) for i_1 and i_3 at a specified temperature whereby:

$$\int_{i_1}^{i_3} f \,\mathrm{d}i = \mathrm{d}(i_1 - i_3) \tag{3.28}$$

The values for i_1 and i_3, defining the solvus, can be calculated for a series of increasing temperatures until i_1 and i_3 converge at a specific temperature and composition – this is the top of the solvus. The trace of Q = 0, which is dependent on T_{c} for pure ilmenite (which is controlled by ΔH and $W_{\mathrm{oilm\,dilm}}$ – calculated to be 15 kJ) is:

$$i = \frac{\mathrm{R}T}{15} \tag{3.29}$$

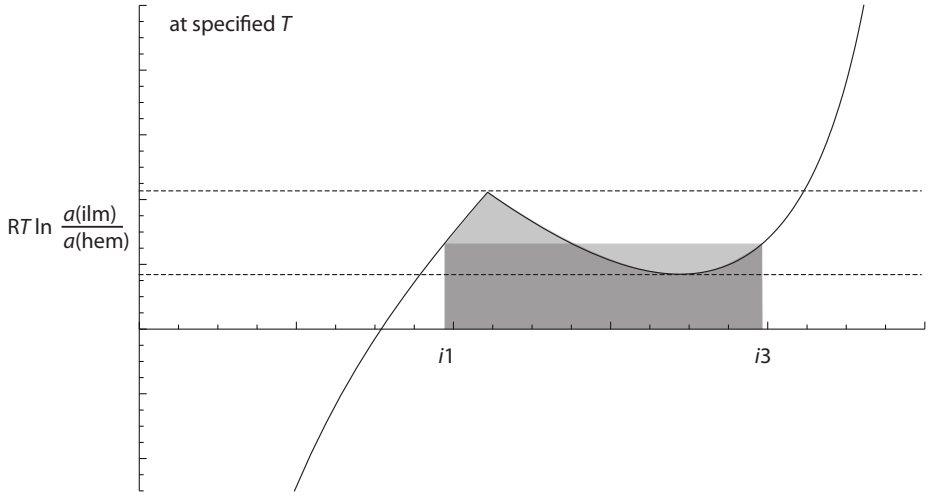

Figure 3.8. Schematic of method used to calculate the ilmenite–hematite solvus. Values for i_1 and i_2 are calculated for a series of increasing temperatures until they converge at a specific temperature and composition. There is a line which can be drawn so that the areas above and below the line are equal. Where this line crosses the curve defines the solvus (composition i_1 and i_3 at a specified temperature.)

The top of the solvus is estimated to be at 1041K (767°C) at i(ilm) of 0.58 as seen in Figure 3.9. This is in agreement with the predictions of modelling by Harrison, Becker and Redfern (2000) and Ghiorso (1990, 1997). Solid solutions which crystallise on either side of this tricritical point will crystallise differently upon cooling. A sample with an ilmenite composition greater than $i = 0.58$ that crystallised in the R$\bar{3}$c field will become progressively ordered with cooling prior to exsolution once it crosses the $Q = 0$ line. Exsolution will be of disordered phase. If the sample initially crystallised with an ilmenite composition less than $i = 0.58$, then it will undergo exsolution without prior ordering, but the phase that is exsolved will be ordered.

Is there a pressure dependence in the interaction parameters?

Harrison and Redfern (2001) describe $T_c = 911 \pm 20$ °C for ilm65 at 1 atm (0 GPa). Later experimental data from Harrison et al. (2006) at increased pressures yield $T_c = 1010 \pm 20$°C at 0.64GPa. Harrison et al. (2006) infers that the increase in T_c is due to an increase in the internal energy of the transition, reflecting a pressure dependence within the cation-cation interaction parameters. Looking at $W_{\text{oilm dilm}}$:
$W_{\text{oilm dilm}} = 15 + P\Delta v$
Δv = pressure dependence
where $i = 0.65$;
and $T = 1283$ K
and $P = 6.4$ kbar (0.64 Gpa)

Substituting pressure-dependent values into Equation 3.29:

$$i = \frac{\mathrm{R}T}{15 + P\Delta v} \tag{3.30}$$

$$0.65 = \frac{\mathrm{R}\,1283}{15 + 6.4\,\Delta v} \tag{3.31}$$

giving a pressure dependence of $\Delta v = 0.22$ kJ kbar^{-1}. The effect of pressure dependence with

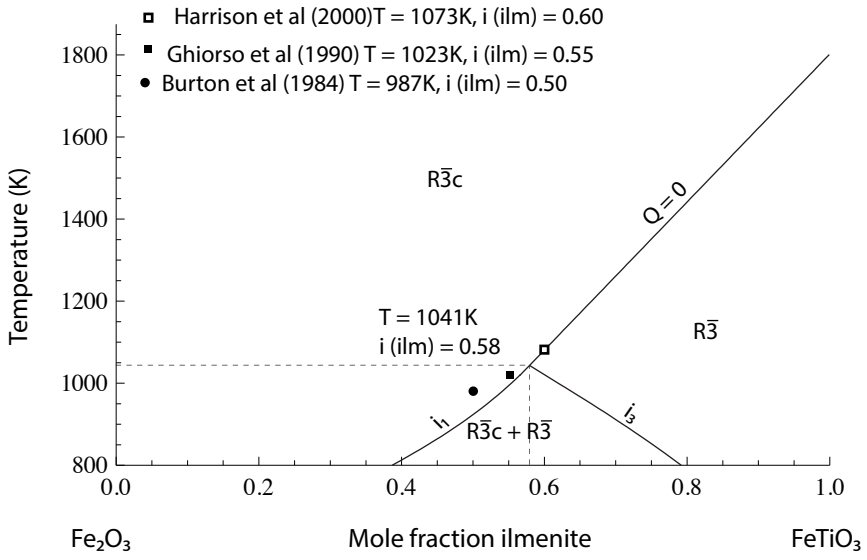

Figure 3.9. A T(K)-i diagram for the Fe_2O_3–FeTiO system. A tricritical point for the ilmenite–hematite solid solution is formed from the intersection of the R$\bar{3}$ to R$\bar{3}$c transition with a low–temperature miscibility gap at T - 1041K and i =0.58. Other estimates for the top of the solvus are shown. At lower i(ilm), and at higher T, ilmenite is disordered. At i(ilm) and lower T, ilmenite is ordered. The trace of Q = 0 represents the critical temperature (T_c) for each proportion of ilmenite.

proportion of ilmenite is visualised in Figure 3.10. The pressure dependence is then added to the interaction energy, so that $W_{\text{oilm dilm}} = 15 + 0.22\,P$ kJ.

3.5.3 The ilmenite–hematite–geikielite–pyrophanite quaternary system

In extending the system into a ilmenite–hematite–geikilite–pyrophanite solid solution, the potential for Mn and Mg to mix on the A and B sites must be accounted for, as well as Fe and Ti. This introduces two more order-disorder parameters – between ordered and disordered geikilite and ordered and disordered pyrophanite (see Figure 3.12 for relations between number of components, n, and number of independent order parameters, s). The site distributions for this scenario is given in Figure 3.11. Q_g is the ordering parameter for geikilite, where

$$Q_g = X^{\text{A}}_{\text{Mg}^{2+}} - X^{B}_{\text{Mg}^{2+}} \tag{3.32}$$

and Q_m is the ordering parameter for pyrophanite, where

$$Q_m = X^{\text{A}}_{\text{Mn}^{2+}} - X^{B}_{\text{Mn}^{2+}} \tag{3.33}$$

The ordering of titanium between A and B sites can now be defined with regards to all long-range ordering paramenters in the system;

$$Q + Q_g + Q_m = X^{\text{B}}_{\text{Ti}^{4+}} - X^{A}_{\text{Ti}^{4+}} \tag{3.34}$$

When only working with order–disorder between Fe and Ti on the A and B site, as was the case with the condition oilm=dilm, the only order–disorder parameter involved in the system was Q

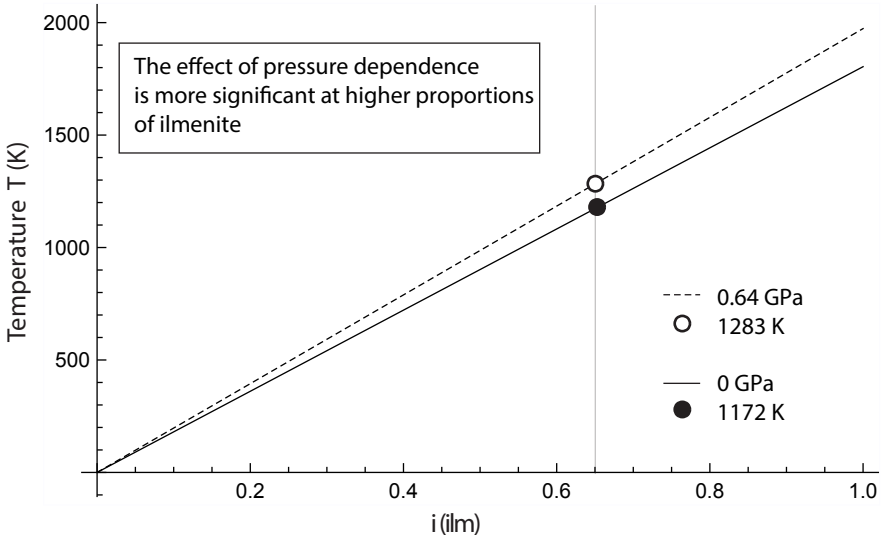

Figure 3.10. Pressure dependence of the ilmenite–hematite solid solution at different proportions on ilmenite (T(K)-i). The solid line follows Equation 3.30 for i where P = 0 kbar and the dotted line models the same equation at 6.4 kbar with a Δv of 0.22

(see Equation 3.26). The equilibrium relations for oilm–dilm now must involve Q_g and Q_m, just as the equilibrium relations for ogeik–dgeik and opnt–dpnt must involve all the ordering parameters. With the extension into an Mn- and Mg-bearing system, g denotes the bulk mole fraction of the $MgTiO_3$ component and m denotes the bulk fraction of $MnTiO_3$ component, in addition to i in Equation 3.6 denoting the bulk mole fraction of $FeTiO_3$ component.

Mass balances in Equations 3.8–3.9 are modified to include the contribution from Mg and Mn:

$$\begin{aligned}
X^{\mathrm{A}}_{\mathrm{Fe^{2+}}} + X^{\mathrm{B}}_{\mathrm{Fe^{2+}}} &= i \\
X^{\mathrm{A}}_{\mathrm{Mg^{2+}}} + X^{\mathrm{B}}_{\mathrm{Mg^{2+}}} &= g \\
X^{\mathrm{A}}_{\mathrm{Mn^{2+}}} + X^{\mathrm{B}}_{\mathrm{Mn^{2+}}} &= m \\
X^{\mathrm{A}}_{\mathrm{Fe^{3+}}} + X^{\mathrm{A}}_{\mathrm{Fe^{2+}}} + X^{\mathrm{A}}_{\mathrm{Mg^{2+}}} + X^{\mathrm{A}}_{\mathrm{Mn^{2+}}} + X^{\mathrm{A}}_{\mathrm{Ti}} &= 1 \\
X^{\mathrm{B}}_{\mathrm{Fe^{3+}}} + X^{\mathrm{B}}_{\mathrm{Fe^{2+}}} + X^{\mathrm{B}}_{\mathrm{Mg^{2+}}} + X^{\mathrm{B}}_{\mathrm{Mn^{2+}}} + X^{\mathrm{B}}_{\mathrm{Ti}} &= 1
\end{aligned}$$

Proportions of end-members:

$$\begin{aligned}
P_{\mathrm{oilm}} &= Q \\
P_{\mathrm{dilm}} &= i - g - m - Q \\
P_{\mathrm{hem}} &= 1 - i - g - m \\
P_{\mathrm{ogeik}} &= Q_g \\
P_{\mathrm{dgeik}} &= Q_g - i - g - m \\
P_{\mathrm{opnt}} &= Q_m \\
P_{\mathrm{dpnt}} &= Q_m - i - g - m
\end{aligned}$$

Site distributions:

$$\begin{aligned}
X^{\mathrm{A}}_{\mathrm{Fe^{2+}}} &= \tfrac{1}{2}i - \tfrac{1}{2}m + \tfrac{1}{2}Q - \tfrac{1}{2}g \\
X^{\mathrm{A}}_{\mathrm{Ti}} &= \tfrac{1}{2}i - \tfrac{1}{2}m - \tfrac{1}{2}Q - \tfrac{1}{2}g \\
X^{\mathrm{A}}_{\mathrm{Fe^{3+}}} &= 1 - i \\
X^{\mathrm{B}}_{\mathrm{Fe^{2+}}} &= \tfrac{1}{2}i - \tfrac{1}{2}m - \tfrac{1}{2}Q - \tfrac{1}{2}g \\
X^{\mathrm{B}}_{\mathrm{Ti}} &= \tfrac{1}{2}i + \tfrac{1}{2}m + \tfrac{1}{2}Q + \tfrac{1}{2}g \\
X^{\mathrm{B}}_{\mathrm{Fe^{3+}}} &= 1 - i \\
X^{\mathrm{A}}_{\mathrm{Mg^{2+}}} &= g \\
X^{\mathrm{A}}_{\mathrm{Mn^{2+}}} &= m
\end{aligned}$$

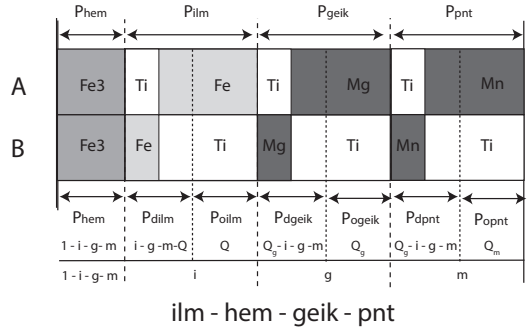

Figure 3.11. Site distributions and proportions of microscopic and compositional end-members for a given proportion of the ilmenite–hematite–geikielite and pyrophanite quaternary system. $P_{ilm/hem/geik/pnt}$ refer to the proportion of the macroscopic end-members ilm, hem, geik and pnt respectively, and $P_{oilm/dilm/hem/dgeik/ogeik/dpnt/opnt}$ refers to the proportion of the microscopic end-members oilm, dilm, hem, dgeik, ogeik, dpnt and opnt respectively.

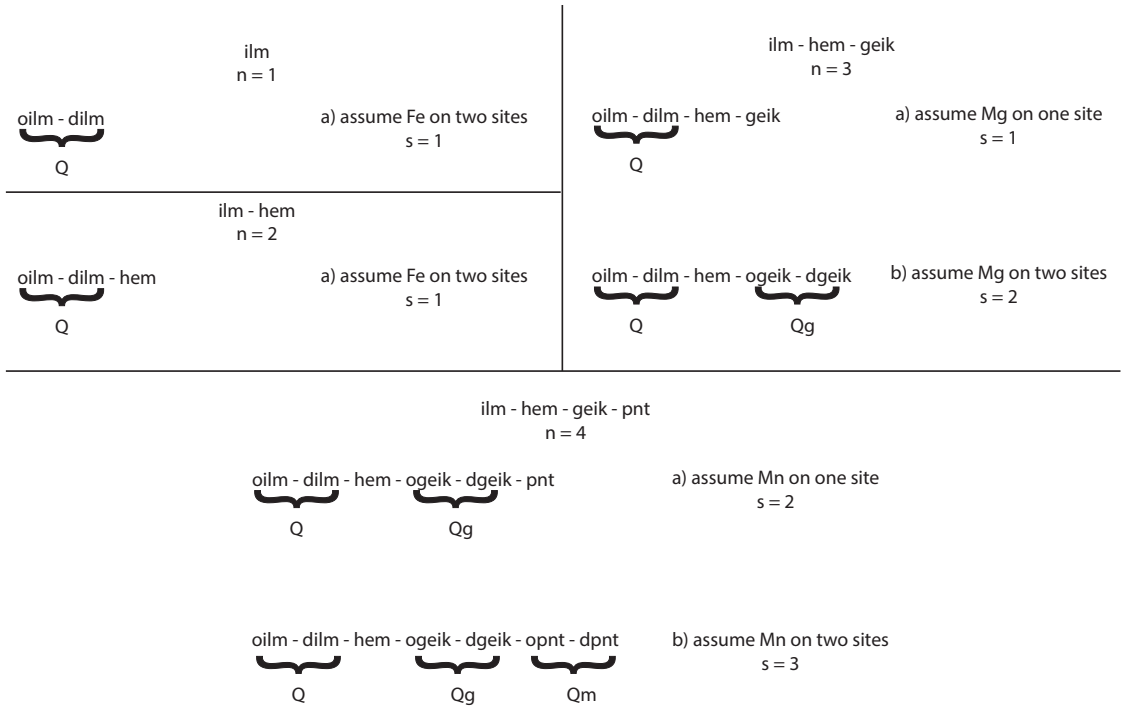

Figure 3.12. Explanation of the number of s independent order parameters to describe the state of order in an $n$component system for pure ilmenite as well as a system expansion to solid solutions with hematite, geikielite and pyrophanite. Explanation follows logic in Figure 3.4.

Using the strong symmetry relationships and the new equilibrium relations together with the W_{ij} values calculated in this study, we can produce a table of interaction values to be used in a new model. The macroscopic interaction energies (W_{ij}) between all the combinations of macroscopic end-members can be derived from their microscopic same-site and cross-site terms as follows. For convergent ordering, site A and site B need to be equivalent. This has strong symmetry implications in the same-site terms. The microscopic interaction energy between elements on the A site is equal to the microscopic interaction energy between the same elements on the B site. This same-site term is designated W_{FeMg}. It follows;

$$W_{\mathrm{FeMgA}} = W_{\mathrm{FeMgB}} \equiv W_{\mathrm{FeMg}},$$

$W_{\mathrm{FeMnA}} = W_{\mathrm{FeMnB}} \equiv W_{\mathrm{FeMn}}$,
$W_{\mathrm{FeFe3A}} = W_{\mathrm{FeFe3B}} \equiv W_{\mathrm{FeFe3}}$,
$W_{\mathrm{TiFe3A}} = W_{\mathrm{TiFe3B}} \equiv W_{\mathrm{TiFe3}}$,
$W_{\mathrm{FeTiA}} = W_{\mathrm{FeTiB}} \equiv W_{\mathrm{FeTi}}$,
$W_{\mathrm{MgTiA}} = W_{\mathrm{MgTiB}} \equiv W_{\mathrm{MgTi}}$,
$W_{\mathrm{MnTiA}} = W_{\mathrm{MnTiB}} \equiv W_{\mathrm{MnTi}}$,
$W_{\mathrm{MgFe3A}} = W_{\mathrm{MgFe3B}} \equiv W_{\mathrm{MgFe3}}$,
$W_{\mathrm{MgMnA}} = W_{\mathrm{MgMnB}} \equiv W_{\mathrm{MgMn}}$,
$W_{\mathrm{MnFe3A}} = W_{\mathrm{MnFe3B}} \equiv W_{\mathrm{MnFe3}}$

and in the cross-site terms:

$W_{\mathrm{Fe3Fe3MgTiAB}} = W_{\mathrm{Fe3Fe3TiMgAB}} \equiv W_{\mathrm{cr2}}$
$W_{\mathrm{Fe3Fe3FeTiAB}} = W_{\mathrm{Fe3Fe3TiFeAB}} \equiv W_{\mathrm{cr2}}$,
$W_{\mathrm{Fe3Fe3MnTiAB}} = W_{\mathrm{Fe3Fe3TiMnAB}} \equiv W_{\mathrm{cr2}}$,
$W_{\mathrm{Fe3Fe3FeMgAB}} = W_{\mathrm{Fe3Fe3MgFeAB}}$,
$W_{\mathrm{Fe3Fe3MgMnAB}} = W_{\mathrm{Fe3Fe3MnMgAB}}$,
$W_{\mathrm{Fe3Fe3FeMnAB}} = W_{\mathrm{Fe3Fe3MnFeAB}}$

Equivalences are used in simplifications, and the right hand sides of these are all taken to be equal, involving just the swapping of the divalent cations between the sites. These are designated W_{cr}.

$W_{\mathrm{Fe3Fe3MnFeAB}} - W_{\mathrm{Fe3Fe3TiFeAB}} - W_{\mathrm{Fe3Fe3TiMnAB}} + W_{\mathrm{Fe3Fe3TiTiAB}} = W_{\mathrm{TiTiFeMnAB}}$,
$W_{\mathrm{Fe3Fe3MgFeAB}} - W_{\mathrm{Fe3Fe3TiFeAB}} - W_{\mathrm{Fe3Fe3TiMgAB}} + W_{\mathrm{Fe3Fe3TiTiAB}} = W_{\mathrm{TiTiMgFeAB}}$,
$W_{\mathrm{Fe3Fe3MnMgAB}} - W_{\mathrm{Fe3Fe3TiMnAB}} - W_{\mathrm{Fe3Fe3TiMgAB}} + W_{\mathrm{Fe3Fe3TiTiAB}} = W_{\mathrm{TiTiMnMgAB}}$,
$W_{\mathrm{Fe3Fe3FeFeAB}} - W_{\mathrm{Fe3Fe3TiFeAB}} - W_{\mathrm{Fe3Fe3TiFeAB}} + W_{\mathrm{Fe3Fe3TiTiAB}} = W_{\mathrm{TiTiFeFeAB}}$,
$W_{\mathrm{Fe3Fe3MgMgAB}} - W_{\mathrm{Fe3Fe3TiMgAB}} - W_{\mathrm{Fe3Fe3TiMgAB}} + W_{\mathrm{Fe3Fe3TiTiAB}} = W_{\mathrm{TiTiMgMgAB}}$,
$W_{\mathrm{Fe3Fe3MnMnAB}} - W_{\mathrm{Fe3Fe3TiMnAB}} - W_{\mathrm{Fe3Fe3TiMnAB}} + W_{\mathrm{Fe3Fe3TiTiAB}} = W_{\mathrm{TiTiMnMnAB}}$

With these, via the macro→micro relationships, the macroscopic W become:

$W_{\mathrm{oilmdilm}} = \frac{W_{\mathrm{FeTi}}}{2} - \frac{W_{\mathrm{cr}}}{4}$,
$W_{\mathrm{oilmogeik}} = W_{\mathrm{FeMg}}$,
$W_{\mathrm{oilmdgeik}} = -\frac{W_{\mathrm{cr}}}{4} + \frac{W_{\mathrm{FeMg}}}{2} + \frac{W_{\mathrm{FeTi}}}{2}$,
$W_{\mathrm{oilmopnt}} = W_{\mathrm{FeMn}}$,
$W_{\mathrm{oilmdpnt}} = -\frac{W_{\mathrm{cr}}}{4} + \frac{W_{\mathrm{FeMn}}}{2} + \frac{W_{\mathrm{FeTi}}}{2}$,
$W_{\mathrm{oilmhem}} = W_{\mathrm{cr2}} + W_{\mathrm{FeFe3}} + W_{\mathrm{TiFe3}}$,
$W_{\mathrm{dilmogeik}} = -\frac{W_{\mathrm{cr}}}{4} + \frac{W_{\mathrm{FeMg}}}{2} + \frac{W_{\mathrm{MgTi}}}{2}$,
$W_{\mathrm{dilmdgeik}} = \frac{W_{\mathrm{FeMg}}}{2}$,
$W_{\mathrm{dilmopnt}} = -\frac{W_{\mathrm{cr}}}{4} + \frac{W_{\mathrm{FeMn}}}{2} + \frac{W_{\mathrm{MnTi}}}{2}$,
$W_{\mathrm{dilmdpnt}} = \frac{W_{\mathrm{FeMn}}}{2}$,
$W_{\mathrm{dilmhem}} = \frac{W_{\mathrm{cr}}}{4} + W_{\mathrm{cr2}} + W_{\mathrm{FeFe3}} - \frac{W_{\mathrm{FeTi}}}{2} + W_{\mathrm{TiFe3}}$,
$W_{\mathrm{ogeikdgeik}} = \frac{W_{\mathrm{MgTi}}}{2} - \frac{W_{\mathrm{cr}}}{4}$,
$W_{\mathrm{ogeikopnt}} = W_{\mathrm{MgMn}}$,
$W_{\mathrm{ogeikdpnt}} = -\frac{W_{\mathrm{cr}}}{4} + \frac{W_{\mathrm{MgMn}}}{2} + \frac{W_{\mathrm{MgTi}}}{2}$,
$W_{\mathrm{ogeikhem}} = W_{\mathrm{cr2}} + W_{\mathrm{MgFe3}} + W_{\mathrm{TiFe3}}$,

$W_{\mathrm{dgeikopnt}} = -\frac{W_{\mathrm{cr}}}{4} + \frac{W_{\mathrm{MgMn}}}{2} + \frac{W_{\mathrm{MnTi}}}{2}$,
$W_{\mathrm{dgeikdpnt}} = \frac{W_{\mathrm{MgMn}}}{2}$,
$W_{\mathrm{dgeikhem}} = \frac{W_{\mathrm{cr}}}{4} + W_{\mathrm{cr2}} + W_{\mathrm{MgFe3}} - \frac{W_{\mathrm{MgTi}}}{2} + W_{\mathrm{TiFe3}}$,
$W_{\mathrm{opntdpnt}} = \frac{W_{\mathrm{MnTi}}}{2} - \frac{W_{\mathrm{cr}}}{4}$,
$W_{\mathrm{opnthem}} = W_{\mathrm{cr2}} + W_{\mathrm{MnFe3}} + W_{\mathrm{TiFe3}}$,
$W_{\mathrm{dpnthem}} = \frac{W_{\mathrm{cr}}}{4} + W_{\mathrm{cr2}} + W_{\mathrm{MnFe3}} - \frac{W_{\mathrm{MnTi}}}{2} + W_{\mathrm{TiFe3}}$

Substituting $W_{\mathrm{cr}} = -60 + 2W_{\mathrm{FeTi}}$ and $W_{\mathrm{cr2}} = 28 - W_{\mathrm{FeFe3}} - W_{\mathrm{TiFe3}}$, to make sure that $W_{\mathrm{oilmdilm}} = 15$ and $W_{\mathrm{dilmhem}} = 13$, and using $W_{\mathrm{FeMg}} = 4$, $W_{\mathrm{FeMn}} = 2$, $W_{\mathrm{MgMn}} = 3$, $W_{\mathrm{FeTi}} = \phi W_{\mathrm{MgTi}}$, $W_{\mathrm{MnTi}} = \phi W_{\mathrm{MgTi}}$, $W_{\mathrm{FeFe3}} = \phi W_{\mathrm{MgFe3}}$, $W_{\mathrm{MnFe3}} = \phi W_{\mathrm{MgFe3}}$. Then with $\phi = 0.7$, $W_{\mathrm{MgFe3}} = 8$ and $W_{\mathrm{MgTi}} = 20$ (from Powell et al., 2014), and including aforementioned pressure dependence of 0.22 we get:

$W_{\mathrm{oilmdilm}} = 15 + 0.22P$,
$W_{\mathrm{oilmogeik}} = 4$,
$W_{\mathrm{oilmdgeik}} = 17 + 0.22P$,
$W_{\mathrm{oilmopnt}} = 2$,
$W_{\mathrm{oilmdpnt}} = 16 + 0.22P$,
$W_{\mathrm{oilmhem}} = 28 + 0.22P$,
$W_{\mathrm{dilmogeik}} = 20 + 0.22P$,
$W_{\mathrm{dilmdgeik}} = 2$,
$W_{\mathrm{dilmopnt}} = 16 + 0.22P$,
$W_{\mathrm{dilmdpnt}} = 1$,
$W_{\mathrm{dilmhem}} = 13$,
$W_{\mathrm{ogeikdgeik}} = 18 + 0.22P$,
$W_{\mathrm{ogeikopnt}} = 3$,
$W_{\mathrm{ogeikdpnt}} = 19.5 + 0.22P$,
$W_{\mathrm{ogeikhem}} = 30.4 + 0.22P$,
$W_{\mathrm{dgeikopnt}} = 16.5 + 0.22P$,
$W_{\mathrm{dgeikdpnt}} = 1.5$,
$W_{\mathrm{dgeikhem}} = 12.4$,
$W_{\mathrm{opntdpnt}} = 15 + 0.22P$,
$W_{\mathrm{opnthem}} = 28 + 0.22P$,
$W_{\mathrm{dpnthem}} = 13$

3.6 Discussion and Conclusions

For pure ilmenite (ilm100), Burton (1985) calculated a value of $T_{\mathrm{c}} = 1400$°C. While experiments by Harrison, Becker and Redfern (2000) did not reach a temperature where Q = 0 for ilm100, the trend in ordering behaviour within pure ilmenite points towards an agreement of a critical temperature at 1400 °C (1673K). This study places the T_{c} of pure ilmenite at $T_{\mathrm{c}} = 1800$K (1526°C) when parameterised in the symmetric formalism. This leads to the calculation of the top of the solvus at 1041K (767°C). New values for macroscopic interaction energies between the ordered and disordered end-members of ilmenite and hematite, as well those required to incorporate magnesium and manganese into the model are given in Table 3.4.

In the White et al. (2000), White, Powell and Johnson (2014) model (see Appendix), $W_{\mathrm{dilm\,hem}}$ was determined to be 11 kJ and $W_{\mathrm{oilm\,dilm}}$ to be 15.6 kJ with $W_{\mathrm{oilm\,hem}}$ at 26.6 kJ accordingly (as

Table 3.4. New o–d interaction energies (W_{ij}) for ilmenite (including pressure dependencies)

	dilm	hem	ogeik	opnt	dgeik	dpnt
oilm	15 + 0.22P	28 + 0.22P	4	2	17 + 0.22P	16 + 0.22P
dilm		13	20 +0.22P	16 + 0.22P	2	1
hem			30.4 + 0.22P	28 + 0.22P	12.4	13
ogeik				3	18 + 0.22P	19.5 + 0.22P
opnt					16.5 + 0.22P	15 + 0.22P
dgeik						1.5

used in White, Powell & Johnson, 2014). This would place T_c at 1880K (1606°C) and the top of the solvus at 996K (722°C), both of which are outside the experimentally constrained range here. The revised interaction energies, as below, have been constrained to experimental data, thus are more geologically realistic, and will feature in the new thermodynamic model for ilmenite. Our variables are:

$$\begin{aligned} i &= 1 - X_{\mathrm{Fe3A}}, \\ g &= \frac{x_{\mathrm{MgA}} + x_{\mathrm{MgB}}}{2}, \\ m &= \frac{x_{\mathrm{MnA}} + x_{\mathrm{MnB}}}{2}, \\ Q &= x_{\mathrm{FeA}} - x_{\mathrm{FeB}}, \\ Q_{\mathrm{g}} &= x_{\mathrm{MgA}} - x_{\mathrm{MgB}}, \\ Q_{\mathrm{m}} &= x_{\mathrm{MnA}} - x_{\mathrm{MnB}}, \\ x_{\mathrm{Fe3B}} &= x_{\mathrm{Fe3A}} \end{aligned}$$

The equilibrium relations are, for dilm-oilm

$$30Q + 31Q_{\mathrm{g}} + 29Q_{\mathrm{m}} + \frac{1}{2}\mathrm{R}T\ln\frac{(-2g+i-2m-Q)(i-Q-Q_{\mathrm{g}}-Q_{\mathrm{m}})}{(-2g+i-2m+Q)(i+Q+Q_{\mathrm{g}}+Q_{\mathrm{m}})}$$

for dgeik-ogeik

$$f_{\mathrm{g}} + 31Q + 36Q_{\mathrm{g}} + 31.5Q_{\mathrm{m}} + \frac{1}{2}\mathrm{R}T\ln\frac{(2g-Q_{\mathrm{g}})(i-Q-Q_{\mathrm{g}}-Q_{\mathrm{m}})}{(2g+Q_{\mathrm{g}})(i+Q+Q_{\mathrm{g}}+Q_{\mathrm{m}})}$$

and for dpnt-opnt

$$f_{\mathrm{m}} + 29Q + 31.5Q_{\mathrm{g}} + 30Q_{\mathrm{m}} + \frac{1}{2}\mathrm{R}T\ln\frac{(2m-Q_{\mathrm{m}})(i-Q-Q_{\mathrm{g}}-Q_{\mathrm{m}})}{(2m+Q_{\mathrm{m}})(i+Q+Q_{\mathrm{g}}+Q_{\mathrm{m}})}$$

with f_{g} and f_{m} being field terms, which contribute to the non-convergence of the system. If both these field terms are zero, then all of Q, Q_{g} and Q_{m} convergently disorder (at the same temperature) with increasing T. If the field terms are non-zero, then Q_{g} and Q_{m} are non-convergent with increasing T.

In the new a–x file, $f_{\mathrm{g}} = 10$ and $f_{\mathrm{m}} = 10$. This parameter makes very little difference to calculated results under normal circumstances, e.g. for the location of [sa,sp,mt] in KFMASHTO as seen in Figure 4.9 in Chapter 4 – $f_{\mathrm{g}} = 0$ gives $g = 0.0965$, $f_{\mathrm{g}} = 10$ gives $g = 0.0842$, $f_{\mathrm{g}} = 100$ gives $g = 0.0822$, for this invariant. Note that m here should be multiplied by 2 for comparison with the White et al. (2000), White, Powell and Johnson (2014) ilmenite a–x relations (see Appendix) in which all Mg was on the A site, arising from the variable definitions. The model created here

assumes Mn and Mg mixing between A and B sites.

This chapter presents a new thermodynamic description of the ilmenite–hematite solid solution. The a–x relations are extended into FMTMn to include order–disorder on the A and B sites for Fe^{2+}, Mg^{2+} and Mn^{2+}. As disorder in mineral solid solutions is a contributing factor to mineral stability at higher temperature, this model should be an improvement to use for calculations at higher temperature.

3.7 Appendix

3.7.1 The new thermodynamic model for ilmenite

```
% ================================================
% ------------------------------------------------
% ilmenite: FMTOMn
%
% Model allows order disorder for Fe, Mg and Mn (20-7-19)
%
%         A                              B
%         Fe    Ti    Mg    Fe3   Mn    Fe    Ti    Mg    Fe3   Mn
% oilm    1     0     0     0     0     0     1     0     0     0
% dilm    1/2   1/2   0     0     0     1/2   1/2   0     0     0
% hem     0     0     0     1     0     0     0     0     1     0
% ogeik   0     0     1     0     0     0     1     0     0     0
% dgeik   0     1/2   1/2   0     0     0     1/2   1/2   0     0
% opnt    0     0     0     0     1     0     1     0     0     0
% dpnt    0     1/2   0     0     1/2   0     1/2   0     0     1/2
%
% i -> 1 - xFe3A
%
% g -> (xMgA + xMgB)/2
%
% m -> (xMnA + xMnB)/2
%
% Q -> xFeA - xFeB
%
% Qg -> xMgA - xMgB
%
% Qm -> xMnA - xMnB
% ------------------------------------------------

ilmf  7  1

  i(ilmf)           0.9
  g(ilmf)           0.02
  m(ilmf)           0.05
  Q(ilmf)           0.85
  Qg(ilmf)          0.018
  Qm(ilmf)          0.048
% ------------------------------------------------

p(oilm)    1 1    0  1  1  Q

p(dilm)    1 1    0  4   1  i  -1  Q  -2  g  -2  m
```

```
p(ogeik)   1 1    0  1  1  Qg

p(dgeik)   1 1    0  2  -1  Qg  2  g

p(opnt)    1 1    0  1  1  Qm

p(dpnt)    1 1    0  2  -1  Qm  2  m

p(hem)     1 1    1  1  -1  i
% ------------------------------------
% ------------------------------------------------
sf
W(oilm,dilm)              15         0       0.22
W(oilm,ogeik)              4         0         0
W(oilm,dgeik)             17         0       0.22
W(oilm,opnt)               2         0         0
W(oilm,dpnt)              16         0       0.22
W(oilm,hem)               28         0       0.22
W(dilm,ogeik)             20         0       0.22
W(dilm,dgeik)              2         0         0
W(dilm,opnt)              16         0       0.22
W(dilm,dpnt)               1         0         0
W(dilm,hem)               13         0         0
W(ogeik,dgeik)            18         0       0.22
W(ogeik,opnt)              3         0         0
W(ogeik,dpnt)           19.5         0       0.22
W(ogeik,hem)            30.4         0       0.22
W(dgeik,opnt)           16.5         0       0.22
W(dgeik,dpnt)            1.5         0         0
W(dgeik,hem)            12.4         0         0
W(opnt,dpnt)              15         0       0.22
W(opnt,hem)               28         0       0.22
W(dpnt,hem)               13         0         0

% ------------------------------------------------
10

xFeA       1 1    0  4  1/2  i  1/2  Q  -1  g  -1  m

xMgA       1 1    0  2  1/2  Qg   1  g

xMnA       1 1    0  2  1/2  Qm   1  m

xTiA       1 1    0  4  1/2  i  -1/2  Q  -1/2  Qg  -1/2  Qm

xFe3A      1 1    1  1  -1  i
```

```
xFeB       1 1    0  4  1/2  i  -1/2  Q  -1  g  -1  m

xMgB       1 1    0  2  -1/2  Qg   1  g

xMnB       1 1    0  2  -1/2  Qm   1  m

xTiB       1 1    0  4  1/2  i  1/2  Q  1/2  Qg  1/2  Qm

xFe3B      1 1    1  1  -1  i
% ------------------------------------------------

oilm    1    2  xFeA 1  xTiB 1
  check 1  0  0  1  0  0
    make  1  ilm  1
    DQF ordered 0 0 0

dilm    4    4  xFeA 1/2  xTiA 1/2  xFeB 1/2  xTiB 1/2
  check 1  0  0  0  0  0
    make  1  ilm  1
    DQF disordered -0.2 0.00047 0.11  % to match W(oilm,dilm), making ilm convergent

hem     1    2  xFe3A 1  xFe3B 1
  check 0  0  0  0  0  0
  make  1      hem    1
  DQF   disordered  0  0  0

ogeik   1    2  xMgA 1  xTiB 1
  check 1  1/2  0  0  1  0
    make  1  geik  1
    DQF 0 0 0

dgeik   4    4  xMgA 1/2  xTiA 1/2  xMgB 1/2  xTiB 1/2
  check 1  1/2  0  0  0  0
  make  1      geik    1
  DQF 28 -0.01153 0.13                  % W gives 18, so for field = 10, 28 here

opnt    1    2  xMnA 1  xTiB 1
  check 1  0  1/2  0  0  1
    make  1  pnt  1
    DQF 0 0 0

dpnt    4    4  xMnA 1/2  xTiA 1/2  xMnB 1/2  xTiB 1/2
  check 1  0  1/2  0  0  0
    make  1  pnt  1
    DQF 25  -0.01153 0.13      % W gives 15, so for field = 10, 25 here
% ========================================================
```

3.7.2 Ilmenite–hematite thermodynamic description (tc-6axmn.txt accessed 01/02/2017) from White et al. (2000) and White, Powell and Johnson (2014)

```
% ilmenite
% Mn and Mg just on A
%
% coded by axe attack on 08 March 2011
%
%         A                                B
%         Fe    Ti    Mg    Mn    Fe3      Fe    Ti    Fe3
% oilm    1     0     0     0     0        0     1     0
% dilm    1/2   1/2   0     0     0        1/2   1/2   0
% hem     0     0     0     0     1        0     0     1
% geik    0     0     1     0     0        0     1     0
% pnt     0     0     0     1     0        0     1     0
%
% i -> 1 - xFe3A
%
% g -> xMgA
%
% m -> xMnA
%
% Q -> xFeA - xFeB
% ------------------------------------------------

ilm  5  1

  i(ilm)           0.9
  g(ilm)           0.02
  m(ilm)           0.02
  Q(ilm)           0.85  range -1 1
% ------------------------------------------------

p(oilm)    1 1    0  1  1  Q

p(dilm)    1 1    0  4  -1  g   1  i  -1  m  -1  Q

p(hem)     1 1    1  1  -1  i

p(geik)    1 1    0  1  1  g

p(pnt)     1 1    0  1  1  m
% ------------------------------------------------
sf
W(oilm,dilm)            15.6         0         0
W(oilm,hem)             26.6         0         0
```

```
W(oilm,geik)              4         0         0
W(oilm,pnt)               2         0         0
W(dilm,hem)              11         0         0
W(dilm,geik)              4         0         0
W(dilm,pnt)               2         0         0
W(hem,geik)              36         0         0
W(hem,pnt)               25         0         0
W(geik,pnt)               4         0         0
% ------------------------------------------------
8

xFeA       1 1    0  4  -1/2  g  1/2  i  -1/2  m  1/2  Q

xTiA       1 1    0  4  -1/2  g  1/2  i  -1/2  m  -1/2  Q

xMgA       1 1    0  1  1  g

xMnA       1 1    0  1  1  m

xFe3A      1 1    1  1  -1  i

xFeB       1 1    0  4  -1/2  g  1/2  i  -1/2  m  -1/2  Q

xTiB       1 1    0  4  1/2  g  1/2  i  1/2  m  1/2  Q

xFe3B      1 1    1  1  -1  i
% ------------------------------------------------

oilm    1    2  xFeA 1  xTiB 1
  check 1  0  0  1
    make  1  ilm  1
    DQF    -13.6075 0.009426 0  % DQF - dH + R Log[4]; dH = 15.6

dilm    4    4  xFeA 1/2  xTiA 1/2  xFeB 1/2  xTiB 1/2
  check 1  0  0  0
     make  1  ilm  1
     DQF     1.9928 -0.0021 0    % DQF = G(equil,Landau) - G(equil,SF)

hem     1    2  xFe3A 1  xFe3B 1
  check 0  0  0  0
  make 1 hem 1

geik    1    2  xMgA 1  xTiB 1
  check 1  1  0  0

pnt     1    2  xMnA 1  xTiB 1
  check 1  0  1  0
```

Chapter 4

An approach to modelling high-grade rocks with domainal textures

4.1 Introduction

When interpreting the metamorphic history of a rock using P–T pseudosections, it is assumed that the bulk-rock composition that is chosen for modelling is representative of the effective volume under which equilibration occurred. Choosing a bulk composition that is representative can be difficult, especially for variables such as H_2O content and oxidation state. A rock may also become domainal, which can be especially relevant for high-grade rocks that have equilibrated above the solidus and have involved melt loss. Small-scale composition variations in the rock can be created in the retrograde history as diffusion distances decrease in coarse-grained rocks with cooling. Petrological examination of samples in thin-section, especially if the assemblage seems to be low-variance, can reveal domains at the mm scale.

This study investigates the evolution of granulites in the Ihosy Formation of southern Madagascar. A sapphirine–quartz-bearing sample is texturally complex and is interpreted to have equilibrated domainally post peak. A KFMASHTO P–T grid and associated orthogonal compatibility diagrams are constructed in order to infer a P–T history of the rock where a traditional pseudosection method is difficult to apply. The peak and retrograde P–T history of non-sapphirine-bearing samples in the vicinity are able to be interpreted using the conventional pseudosection approach in order to further constrain the metamorphic history of the terrane.

This chapter also applies the new thermodynamic model for sapphirine (Wheller & Powell, 2014), which allows the more accurate representation of rocks formed at higher temperatures in oxidised metamorphic terranes. The sapphirine-bearing granulites of southern Madagascar were previously considered to be too oxidised for modelling to produce an accurate estimation of the conditions of formation. With the new sapphirine model accounting for Fe^{3+} in the mineral structure, the stability of sapphirine-bearing mineral assemblages to lower temperatures is expected, and thus the perceived peak temperature of the assemblage may be lower than previous estimates. These rocks provide the opportunity to throw light on high-temperature rock-forming processes in general, as well as to understand the geology of southern Madagascar in particular. The latter is significant given the involvement of Madagascar in the assembly of Gondwana.

4.2 Geodynamic setting

In its place at the centre of the Neoproterozoic/Cambrian East African Orogen, Madagascar is a unique location to investigate the final collision involved in the formation of the supercontinent Gondwana. This assembly was completed by $\sim$ 520 Ma (Tucker, Roig, Moine, Delor & Peters, 2014). Of the five tectonic domains in southern Madagascar – the Vohibory, Graphite, Androyen, Anosyen, and Ikalamavony domains – the Anosyen domain (Figure 4.1) contains rocks that record the highest metamorphic grade. The Anosyen domain is bounded by the Androyen domain to the west and the Ikalamavony domain to the north-east (Boger et al., 2019). Boger et al. (2015) propose a sequence of events leading to the collision and suturing of these domains, where at >650 Ma, the Vohibory is an intra-oceanic island arc, the Androyen is a micro-continent and the Anosyen is part of the Indian passive-margin. A collision at 630–610 Ma of the Vohibory and the Androyen is reflected in the Ampanihy high-strain zone and causes M_1 deformation and metamorphism in the two tectonic domains. At 580–520 Ma the Anosyen and the Androyen domains collide forming the Beraketa high-strain zone associated with the intrusion of syn- and post-tectonic granites in the east as well as the M_2 deformation and metamorphism.

There is a bimodal distribution of geochronological data (*ca.* 630 Ma and at 520 Ma) within the East African Orogen (Boger et al., 2015; Jöns & Schenk, 2011; Meert, 2003). The earliest metamorphic event associated with the formation of Gondwana is observed in the Vohibory and Androyen domains, to the west of the Beraketa shear zone (GAF-BGR, 2008). The majority of studies place the 630–610 Ma metamorphism exclusively in the west, while Horton, B., Kylander-Clark, R. and Jöns (2016) observe several samples from the western margin of the Anosyen with dates of around 600 Ma. Boger et al. (2015) uses the presence or absence of the 630–600 Ma (M_1) deformation and metamorphism to define the final suture in south-east Madagascar as occurring within the Beraketa shear zone. The dearth of a 630–600 Ma metamorphic signature in rocks in the Anosyen implies that the Indian Plate (pre-Gondwana) was spatially separate from the eastern Arabian Nubian Shield during this time. The metamorphic histories of the western (Vohibory, Androyen) and the eastern tectonic domains (Anosyen, Ikalamavony) are shared at 580–520 Ma, implying that by this time, the Indian, Azania and the Arabian Nubian Shield have been assembled (Boger et al., 2015).

The western most tectonic domains, separated from the Anosyen domain by the Bereketa shear zone record the earliest metamorphism (M_1), with peak conditions in the upper-amphibolite to granulite facies (GAF-BGR, 2008; Jöns & Schenk, 2008; Nicollet, 1989). The later event (M_2), producing the highest metamorphic grade in Madagascar, is found in the Anosyen domain, with conditions in the granulite-facies. Peak metamorphic temperatures in the Anosyen have been estimated to have reached >880°C (e.g. Boger, White & Schulte, 2012; Holder, Hacker, Horton & Rakotondrazafy, 2018; Horton et al., 2016). Jöns and Schenk (2011) record a northward decreasing metamorphic grade within the Anosyen. This study will focus on the M_2 event at 580–520 Ma as preserved in the granulite rocks in the Anosyen domain exposed within a lower crustal section in southern Madagascar.

4.2.1 Metamorphism in the Anosyen domain

The protolith rocks in the Anosyen domain are the Horombe and the Iakora Groups (Boger et al., 2008a, 2008b; GAF-BGR, 2008), the latter of which is discussed here in detail. The Iakora Group includes the diopside-scapolite calcsicilate rocks of the Tranomaro Formation, as well as the psammopelites and pelites of the Ihosy, Amparihy and Bakika Formations. The Ihosy Formation is the main metapelitic unit in southern Madagascar and outcrops in areas from Tranomaro to north

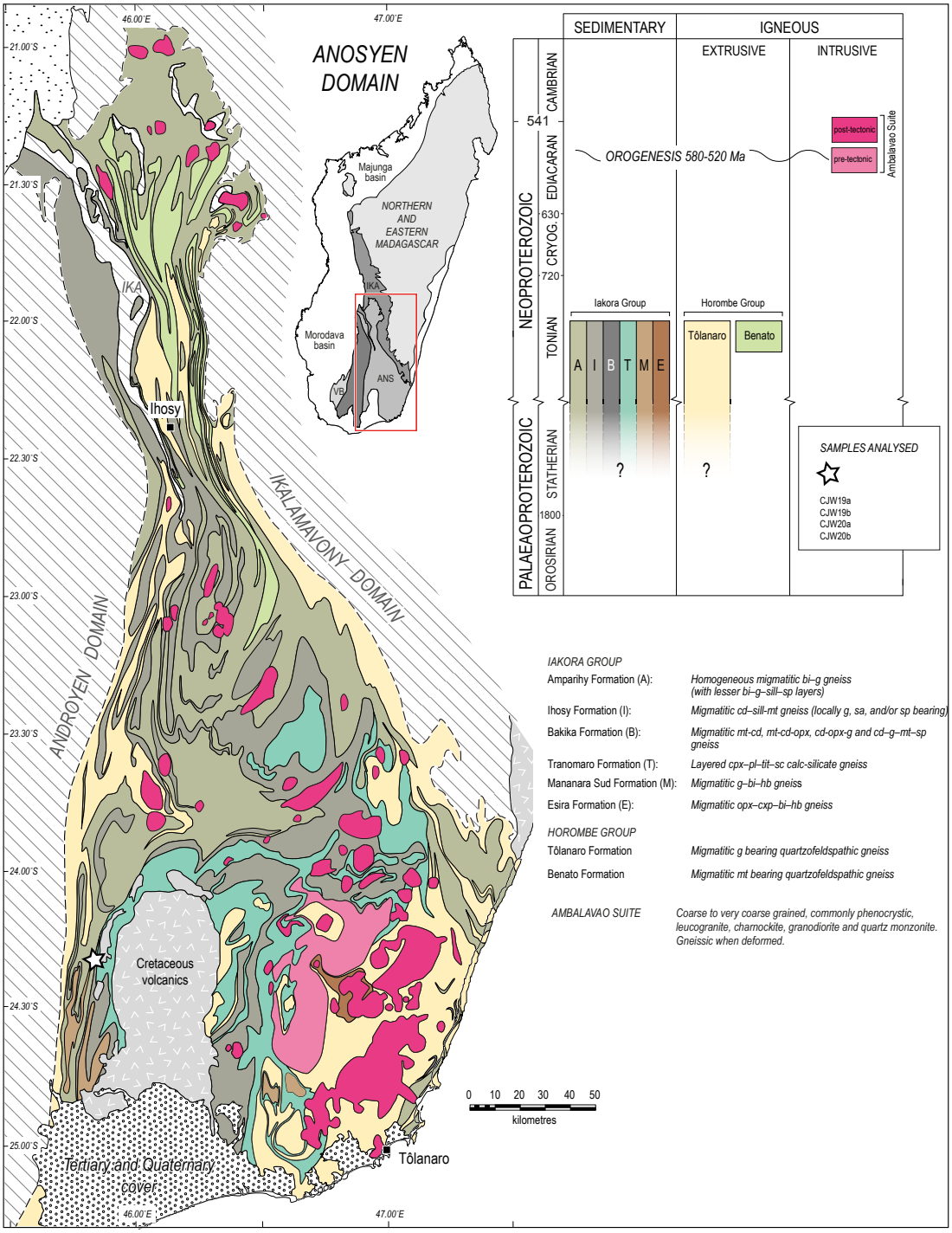

Figure 4.1. Geology of the Anosyen domain in southern Madagascar. Red box in top insert shows field area. The Ihosy Formation (I) is light grey. White star in the south-west is the location of samples CJW19a, CJW19b, CJW20a and CJW20b. (Map modified from Boger et al., 2019)

of Ihosy and is the focus of sample collection. It is intercalated with the Tranomaro Formation and can be found in its type locality in the quarries in the vicinity of Ihosy.

Metapelites tend to be the most useful rock type to investigate the P–T conditions imposed on a terrane. Derived from clay-rich sediments such as shales and mudstones, the variation in bulk composition and the strong pressure-temperature dependence of the minerals developed, results in the growth of characteristic mineral assemblages in geologically significant P–T intervals. Peak pressure and temperature conditions associated with the final collision at 580–520 Ma (M_2) are recorded in the metapelitic rocks of the Anosyen domain. They have previously been estimated to have been metamorphosed between 4 and 11 kbar, with most studies agreeing around 6 kbar. Estimated peak temperatures vary from >900°C in the south (area below Betroka down to Tôlanaro), to ∼800°C in the north (north of Ihosy, Horton et al., 2016).

Boger et al. (2012) suggest peak conditions of 880–920°C at 6–6.5 kbar in the south-east using pseudosection modelling of metapelitic granulites in the chemical system NCKFMASHTO. Slightly lower temperature estimates of ∼830–850 °C are calculated from granulites in the north, due to the observed preservation biotite. Using a range of mineral reaction textures, Boger et al. (2012) infer that a retrograde path involves a small degree of decompression with post peak cooling.

Temperature estimates based on exchange thermobarometry (700–800°C, 4.5–5.5 kbar Moine, Takotondratsima & Cuney, 1985), (750–950°C, 4.5–5.5 kbar Ackermand, Windley & Razafiniparany, 1989), (750–800 °C, 6kbar Kröner, Braun & Jaeckel, 1996) are lower than Boger et al. (2012), with the assumption that cation-exchange during cooling may explain the difference. Another study using phase diagrams estimated higher temperatures (e.g. 900–1050 °C, 5.5–6.5 kbar Rakotonandrasana, Arima, Miyawaki & Rambeloson, 2010). These temperatures are suggested to have been influenced by the underlying strongly oxidised rocks of the Ihosy Formation (the subject of this chapter). This further cements the importance of using thermodynamic models that account for the ferric iron substitution in minerals. Not accounting for ferric would lead to higher temperature estimates and perhaps lower the pressure at which garnet would become stable.

The highest temperature and pressure estimates are suggested by Jöns and Schenk (2011), placing the terrane firmly in a ultrahigh-temperature (UHT) metamorphic conditions (where peak metamorphic temperatures exceed 900°C). They use inferred coexisting osumilite–garnet and sillimanite–orthopyroxene assemblages to infer peak of temperatures of 950–1000°C and 8–11 kbar before decompression to 4–6 kbar. They also describe a sapphirine–quartz-bearing sample that is not included in their estimations due to the inability of the sapphirine model to account for the oxidation of the terrane (having found considerable Fe^{3+} and magnetite present in the rocks). However oxidation state was also not taken into account in their calculations for other assemblages. The stability of coexisting sill–opx can shift to lower temperatures if the rock contains Fe^{3+} (Carson & Powell, 1996; Diener, White & Powell, 2008; Harley, 2008). It is therefore plausible that the UHT P–T by Jöns and Schenk (2011) is overestimated. Note that Jöns & Schenk do not separate the Androyan and Anosyen domains, and that the rocks in question, though labelled Androyan, are from the new area designated the Anosyen.

Horton et al. (2016) analyse the same sapphirine–quartz-bearing sample as Jöns and Schenk (2011). Using 4+ Cation Thermometry, this sample yields a peak temperature of 865°C, using 10kbar, however they note that peak temperature may be underestimated given the proximity to higher temperature rocks. The study notes that Ti-in-quartz temperatures (after Thomas et al., 2010) are reduced by approximately 25°C per kbar.

The first direct observation of the supposed UHT mineral osumilite in the field area were made by Holder et al. (2018) and a sample of the rock was used for phase-equilibria modelling to determine peak P–T in the Ihosy Formation. The osumilite solution model used for thermodynamic

modelling was the Holland, Babu and Waters (1996) version, meaning that, as noted by Holder et al. (2018), the results are limited by the lack of Fe^{3+}, Mn, Ca, Na and Ti in the solution model. In conjunction with inherently-uncertain (due to the absence of good experimental data) feldspar thermometry, the study suggests that M_2 metamorphism occurred at 910–950°C at less than 6.5kbar.

This chapter uses four samples collected from the oxidised Ihosy Formation, collected in the south-west of the Anosyen domain (see Figure 4.1). This is from a same area as the sapphirine sample analysed by Jöns and Schenk (2011) and Horton et al. (2016). With the application of the new thermodynamic model for sapphirine (Wheller & Powell, 2014) that accounts for Fe^{3+} in the sapphirine lattice, the peak temperature for M_2 metamorphism is expected to be lower than previously estimated. As sapphirine+quartz is traditionally thought of as a UHT indicator assemblage, a decrease to below 900°C adds evidence that this may not be the case for oxidised terranes. The purpose of this study is not to reconstruct a metamorphic history of southern Madagascar; instead it is mostly focused on inferring P–T conditions of complex domainal mineral assemblages in high-temperature granulites, while applying the new sapphirine model to an oxidised metamorphic terrane.

4.3 Methodology

4.3.1 Samples

Samples locations are listed in Table 4.1, and indicated by the white star in the geological map of southern Madagascar in Figure 4.1. Specific mineral assemblages grow at different P–T conditions dependent on the bulk composition of the rock. Different mineral assemblages within a localised area (therefore experiencing the same P–T regime) from rocks with different bulk compositions can greatly constrain the P–T conditions of the area. The samples chosen for study are metapelites of the Ihosy Formation, and were collected within a small geographical area approximately 10km north of the village of Imanombo, and in the vicinity of the sample Md81-1-04 of Jöns and Schenk (2011). The samples collected in the Imanombo region contain different low variance peak assemblages within a small area, making them ideal for calculation of a peak P–T for the location. Samples CJW19a, CJW19b, CJW20a and CJW20b are chosen for petrographic analysis and phase equilibria modelling. Petrography involves analysis of peak and retrograde mineral assemblages based on the preserved grain sizes and microstructures. The observation of the development of microdomains in sample CJW20b provides an opportunity to explore using P–T grids and compatibility diagrams to constrain the peak metamorphic conditions experienced by the Ihosy Formation during M_2. Samples CJW19a, CJW19b, CJW20a are modelled using traditional pseudosections. Appropriate H_2O and O contents to use in modelling are identified using T–M_{H_2O} and T–M_O pseudosections.

Table 4.1. Sample locations

Samples	Tectonic domain	Formation	Rock type	Longitude	Latitude	Figures
CJW19a	Anosyen	Ihosy	Metapelite (-sa)	E45°49' 59.0304"	S24°19' 50.1132"	4.18
CJW19b	Anosyen	Ihosy	Metapelite (-sa)	E45°49' 59.0304"	S24°19' 50.1132"	4.19
CJW20a	Anosyen	Ihosy	Metapelite (-sa)	E45°49' 53.9178"	S24°19' 54.804"	4.20
CJW20b	Anosyen	Ihosy	Metapelite (+sa)	E45°49' 53.9178"	S24°19' 54.804"	4.9-4.14

4.3.2 Analytical procedures and abbreviations

Major element bulk rock analyses of samples were obtained at the Johannes Gutenberg University Mainz at the Institute of Geoscience using the Phillips Magix PRO XRF equipped with a Rh-tube

(75 μm Be-window) and using an accelerating voltage of 60kV. Mineral chemical analyses were undertaken using a Jeol JXA 8900 RL electron microprobe using an accelerating voltage of 15 kV, a beam current of 12 nA and a beam diameter of 2 μm.

Mineral abbreviations follow Powell & Holland usage and are as follows: g, garnet; opx, orthopyroxene; bi, biotite; sill, sillimanite; cd, cordierite; sa, sapphirine; q, quartz; pl, plagioclase; ksp, K-feldspar; liq, silicate liquid (melt); ilm, ilmenite; mt, magnetite; and sp, spinel. Alm = almandine content of garnet = $X_{\mathrm{alm}} = \mathrm{Fe}^{2+}/(\mathrm{Fe}^{2+} + \mathrm{Mg} + \mathrm{Ca} + \mathrm{Mn})$; Py = pyrope content of garnet = $X_{\mathrm{py}} = \mathrm{Mg}/(\mathrm{Fe}^{2+} + \mathrm{Mg} + \mathrm{Ca} + \mathrm{Mn})$; spss = spessartine content of garnet = $X_{\mathrm{spss}} = \mathrm{Mn}/(\mathrm{Fe}^{2+} + \mathrm{Mg} + \mathrm{Ca} + \mathrm{Mn})$; gr = grossular content of garnet = $X_{\mathrm{gr}} = \mathrm{Ca}/(\mathrm{Fe}^{2+} + \mathrm{Mg} + \mathrm{Ca} + \mathrm{Mn})$; an = anorthite content of plagioclase = $X_{\mathrm{an}} = \mathrm{Ca}/(\mathrm{Ca} + \mathrm{Na} + \mathrm{K})$;$X_{\mathrm{Fe}} = (\mathrm{Fe}^{2+} + \mathrm{Fe}^{3+})/(\mathrm{Fe}^{2+} + \mathrm{Fe}^{3+} + \mathrm{Mg})$; $X_{\mathrm{Mg}} = \mathrm{Mg}/(\mathrm{Mg} + \mathrm{Fe}^{2+} + \mathrm{Fe}^{3+})$; $X_{\mathrm{Mg*}} = \mathrm{Mg}/(\mathrm{Mg} + \mathrm{Fe}^{2+})$; $X_{\mathrm{Al}} = \mathrm{Al}/(\mathrm{Al} + \mathrm{Fe}^{2+} + \mathrm{Fe}^{3+} + \mathrm{Mg})$. For the oxides, $X_{\mathrm{ilm}} = \mathrm{Ti}/(\mathrm{Ti} + \mathrm{Fe}^{3+})$, $\mathrm{X_{herc}} = \mathrm{Fe}^{2+}/(\mathrm{Fe}^{2+} + \mathrm{Mg} + \mathrm{Zn})$, $\mathrm{X_{mt}} = \mathrm{Fe}^{3+}/(\mathrm{Fe}^{3+} + \mathrm{Al})$ and $\mathrm{X_{gah}} = \mathrm{Zn}/(\mathrm{Fe}^{2+} + \mathrm{Mg} + \mathrm{Zn})$.

4.4 Methodology of phase diagram calculation

In order to constrain the peak and retrograde history of the metapelites from the Ihosy Formation, a series of calculated phase diagrams are presented. These include *P–T* pseudosections to model the peak mineral assemblages preserved in homogeneous samples, as well as *P–T* projections and compatibility diagrams to investigate formation of 'microdomains' in samples that are interpreted to be inhomogeneous. Calculations were performed using THERMOCALC 3.40 using an updated version of the Holland & Powell 2011 data set (**ds62**, 2015; file tc-ds62.txt). The activity-composition (*a-x*) models are taken from White, Powell, Holland, Green et al. (2014) with the sapphirine model from Wheller and Powell (2014).

4.4.1 Choosing an appropriate chemical system

The pseudosections presented in this section are calculated in the Na_2O-CaO-K_2O-FeO-MgO-Al_2O_3-SiO_2-H_2O-TiO_2-Fe_2O_3 (NCKFMASHTO) chemical system. The inclusion of TiO_2 and Fe_2O_3 in the chemical system ensures the effect of these oxides on the stability of biotite, spinel and sapphirine at high temperatures and at increased oxidation states is accounted for (e.g. Sack & Ghiorso, 1991; Wheller & Powell, 2014) as well as allowing consideration of rutile and ilmenite. F and Zn also act upon biotite and spinel stability, respectively, increasing the stability of the former to higher temperature and the latter to lower temperature. At higher temperatures, these effects are larger, with the result being that the phase diagrams in NCKFMASHTO are likely to underestimate the stability of these minerals. Thus, inferred peak assemblages on the phase diagrams may be biotite and/or spinel absent, while the observed mineral assemblage may preserve small amounts at peak. The exclusion of MnO in the chemical system is justified by the low amounts of the oxide in the bulk composition. Thus, the manganese contribution is excluded for simplicity, but fluorine and zinc are excluded because the models to include them do not exist yet.

For non-pseudosection related modelling – i.e. the *P–T* petrogenetic grid and the compatibility diagrams – the system must be decreased in order to explore the extra dimension of multiple bulk compositions within one diagram. For these calculations, the chemical system KFMASHTO is used. By disregarding the C component (CaO) garnet is destabilised. In combination with dropping the CaO, disregarding the N component (Na_2O) means that plagioclase is not considered. Melt is also destabilised by the absence of Na_2O and CaO. This is important to note, as assemblages containing garnet and melt may be restricted to higher pressure and temperature conditions than geologically

realistic.

Phases that are included in calculations are garnet, biotite, sapphirine, cordierite, orthopyroxene, sillimanite, spinel, magnetite, ilmenite, K-feldspar, plagioclase, quartz and melt. The high-temperature metapelitic mineral osumilite, which is estimated to become stable at temperatures greater than 1000°C in these rocks, cannot be considered as a thermodynamic model is not yet available in KFMASHTO.

4.4.2 Choosing an effective bulk composition

A bulk composition is chosen to represent an equilibration volume of the mineral assemblage observed in thin section. For high-grade rocks such as the ones in discussion here, bulk composition measured from XRF is sufficient *if* the rocks are homogeneous and minerals are unzoned (Kelsey, White & Powell, 2005). At peak, diffusion distances are long and therefore equilibrium can be assumed, however in some cases, especially if there has been loss of fluid/melt during partial melting, the rock can become domainal at different scales. Guevara and Caddick (2016) observe the development of 'microdomains' which are seen in thin-section at the mm and <mm scale. The definition of a 'microdomain' is an 'area of a thin section that displays evidence of localised mineral reaction at the grain scale'.

Assemblages and textures evolve through P–T space over a length-scale, which gets smaller particularly with decreasing temperature and in the absence of fluid. Equilibrium is achieved through flattening chemical potential (μ) gradients. Diffusion to flatten chemical gradients can be accelerated through the later addition of fluid, effectively 'restarting' equilibration. Where there is effective intergranular transport between grain boundaries, equilibrium is maintained (Guiraud, Powell & Rebay, 2001). When fluid is lost through partial melting, microdomains that were in equilibrium at the grain boundaries lose their method for maintaining equilibrium. Diffusion distances are reduced over time, and only localised microdomains continue to progressively re-equilibrate. The reduction of equilibration length scale of chemical potential diffusion distances by temperature drop and/or loss of fluid or melt on grain boundaries can set up texturally distinct microdomains. This means that each separate microdomain must be treated with a different effective bulk composition, and in a pseudosection approach, by calculating separate pseudosections.

There are already successful ways to estimate the bulk compositions of microdomains (e.g. collecting EDS spectra of major elements for pre-defined areas using a scanning electron microscope, Guevara & Caddick, 2016). The effective bulk composition is then iteratively determined by calculating pseudosections for each estimated bulk composition and matching the resulting equilibrium assemblages with those observed from petrography in the microdomain. However, this thesis will explore domainal equilibration in a more qualitative sense. This explorative approach requires scrutiny of the P–T petrogenetic grid and associated compatibility diagrams as well as identification of univariant reactions that constrain assemblages observed in each microdomain.

Estimating water and oxidation state

Three samples in this study are modelled using whole rock analysis as effective bulk composition. This is because, unlike the sapphirine sample, petrological examination reveals that the mineral assemblage and texture is homogeneous. However, the Fe_2O_3 and H_2O content still need to be estimated. The H_2O content used in modelling is important because it dictates (along with Na_2O and K_2O) the location of the solidus (White, Powell & Holland, 2001).

Whole rock analyses report a value called loss-on-ignition (LOI), which is the amount of weight loss from the sample as it is heated and oxidised during analysis. For the following calculations,

H_2O is approximated by using the LOI value as a maximum and adjusted through T–M_{H_2O} pseudosections so that the rock reaches peak at temperatures not much greater than the solidus, as assemblages tend to be preserved when minimal melt is present (e.g. Diener, White & Hudson, 2014). The T–M_{H_2O} method assumes that a proportion of the composition will be partitioned into making a silicate melt.

Whole rock analyses only report total iron, with no determination on the oxidation state the iron cations. Quantification of the Fe^{3+}content of the effective bulk composition is estimated here by the titration method on dissolved rock powders and varied through T–M_O pseudosections predicting the observed mineral assemblage stability. To account for oxidation post peak, the titration results are considered a maximum for ferric iron content.

Within THERMOCALC Fe_2O_3 is specified in terms of a combination of FeO and O, thus 1 mole of Fe_2O_3 is formed by combining 1 mole O with 2 mole FeO. Modelling herein uses O as a measure of oxidation state, and is calculated in the bulk composition used in THERMOCALC and displayed on the x-axis of T–M_O diagrams. The effect that O has on mineral stability within a bulk assemblage can be investigated using a T–M_O diagram, whereby O is varied across the x-axis and the resulting assemblages at different temperatures calculated at a fixed pressure.

In order to provide comparison to oxidation states estimated by Boger et al. (2012) for previous modelling undertaken in the area, an 'oxidation ratio' is calculated. The calculation follows Chinner (1960), whereby a rock with wholly Fe^{2+}would have an oxidation ratio of 0, a rock with equal amounts $Fe^{2+}$and Fe^{3+}would have an oxidation ratio of 66.6, and a rock with all iron as Fe^{3+}would have an oxidation ratio of 100. An oxidation ratio in moles:

$$\frac{2Fe_2O_3 \cdot 100}{2Fe_2O_3 + FeO} \tag{4.1}$$

The following shows an example of quantifying oxidation state:

Sample CJW19a

Titration results:

Fe_2O_3: 3.63 mol%

FeO: 5.51 mol%

The titration value for Fe_2O_3 is then broken up into 2 mol of FeO and 1 mol of O. O is the 'oxygen number' and is the measure of oxidation state used in THERMOCALC.

$Fe_2O_3 = 2FeO + O$

1 mol of O = 3.63

2 mol of FeO = $2 \times 3.63 = 7.26$

O# = 3.63 mol.%

A corrected ferrous iron (FeO*) is therefore the titrated FeO value + the FeO in Fe_2O_3

FeO* = 5.51 + 7.26

FeO* = 12.77 mol.%

The oxidation ratio (following Chinner, 1960), substituting the above into Equation 4.1:

$$\frac{2(3.63) \cdot 100}{2(3.63) + 5.51} = 57$$

Oxidation ratio = 57

THERMOCALC input variables for oxidation state, as well as titration data for each sample are given in Table 4.2.

Table 4.2. Oxidation state from titration

Ihosy Formation	Sample	FeO (mol%)	Fe_2O_3 (mol%)	O	FeO*	Oxidation ratio
	CJW19a	5.51	3.63	3.63	12.77	57
	CJW19b	5.56	3.97	3.97	13.51	59
	CJW20a	4.68	2.37	2.37	9.41	50
	CJW20b	5.01	1.16	1.16	7.34	32

Boger et al. (2012) provides P/T–M_O pseudosections on a rock from the Ihosy Formation. A garnet-absent, magnetite-bearing assemblage is not predicted using a bulk composition with an estimated very low ferric content (O=0.01). Increasing the oxidation ratio at a given P or T to above 40 stabilises sill–cd–mt, with a slightly lower oxidation ratio stabilising garnet and increasing temperature stabilising spinel. The oxidation ratio calculated for Ihosy Formation samples in this study range from 32 to 59 and therefore agree with the increased oxidation state estimated for the modelling of these rocks in the Boger et al. (2012) study.

The loss-on-ignition (LOI) value provided in the analysis of the bulk composition is used as a maximum value for water content in the sample. The amount of water at peak is unknown, and thus the amount of H_2O in a bulk assemblage can be varied across the x-axis in a T–M_{H_2O} diagram to produce the interpreted topology. A value of 1 mol.% H_2O was chosen to model samples CJW19a, CJW19b and CJW20a, producing topologies whereby the peak metamorphic mineral assemblage is preserved during the last vestiges of melt present, just above the solidus. Table 4.3 details the bulk rock compositions for the non-sapphirine-bearing rocks in mol% used in quantitative phase modelling in THERMOCALC.

Table 4.3. Mol% composition used for phase diagram calculations

Figure	Sample	H_2O	SiO_2	Al_2O_3	CaO	MgO	FeO*	K_2O	Na_2O	TiO_2	O
4.18	CJW19a	1.00	61.12	16.36	0.56	5.37	12.77	0.96	0.88	1.11	3.63
4.19	CJW19b	1.00	58.15	18.19	0.73	6.14	13.51	1.32	0.77	1.17	3.97
4.20	CJW20a	1.00	67.39	14.97	0.99	3.90	9.41	1.91	1.22	0.78	2.37

4.5 Petrography, mineral chemistry and thermodynamic modelling

The four samples can be divided on their observed petrography, as 'sapphirine-bearing' and 'non-sapphirine-bearing'. This breakdown was chosen due to different techniques required in their P–T interpretations. A summary of the interpreted peak mineral assemblages is given in Table 4.4. Representative mineral compositions of the rocks are given in Tables 4.5 to 4.6. Calculated end-member proportions and cation ratios discussed below are X_{alm}, X_{py}, X_{spss} and X_{gr} for garnet, and X_{Fe} for sapphirine, orthopyroxene and garnet.

Table 4.4. Interpreted peak mineral assemblages

Sample	Interpreted peak mineral assemblage
CJW19a	g + sill + mt (+ q + pl + ksp + ilm + liq)
CJW19b	g + sill + mt (+ q + pl + ksp + ilm + liq)
CJW20a	g + sill + mt (+ q + pl + ksp + ilm + liq)
CJW20b	sa + q + mt + liq; opx + sill; opx + sill + liq (+ q + pl + ksp + ilm)

4.5.1 Sapphirine-bearing sample

The sapphirine-bearing sample (CJW20b) is a sapphirine–sillimanite–cordierite–orthopyroxene–magnetite–garnet metapelite. The sample is spatially inhomogeneous, with petrographic observations revealing at least three distinct mineral textures ('microdomains' - see definition above), with the ferromagnesian minerals distributed in distinct associations (Figure 4.2). It is postulated that the rock equilibrated domainally. For modelling purposes, three main microdomains are interpreted: sapphirine–quartz–magnetite–liq (sa–q–mt–liq); orthopyroxene–sillimanite (opx–sill); and (orthopyroxene–sillimanite–liquid (opx–sill–liq) in addition to quartz, plagioclase, K-feldspar and ilmenite.

Domain 1: sa–q–mt–liq (+ q + pl + ksp + ilm)

Domain 1 is defined by coarse-grained sapphirine with a pinitised cordierite corona, which separates the sapphirine from a quartz and perthitic K-feldspar matrix (Figure 4.3). Sapphirine contains inclusions of quartz rimmed by cordierite and is associated with magnetite, ilmenite, and exsolved hercynite-spinel (Figure 4.4). This texture shows the breakdown of formally co-existing sapphirine + quartz (with melt) to form cordierite and spinel after melt loss. The inferred peak equilibrium assemblage for Domain 1 is: sapphirine, magnetite, quartz, plagioclase, K-feldspar and melt.

Domain 2: opx–sill (+ q + pl + ksp + ilm)

Domain 2 is defined by coarse-grained orthopyroxene intergrown with prismatic sillimanite which is in direct contact with the quartz and perthitic K-feldspar matrix (Figure 4.5). Cordierite is absent from this microdomain. This texture shows that orthopyroxene + sillimanite continued to coexist without cordierite breakdown. The inferred peak equilibrium assemblage for Domain 2 is: orthopyroxene, sillimanite, quartz, plagioclase, K-feldspar and ilmenite.

Domain 3: opx–sill–liq (+ q + pl + ksp + ilm)

Domain 3 is similar to Domain 2 in that it is defined by orthopyroxene intergrown with prismatic sillimanite. The difference is that orthopyroxene is separated from sillimanite, late stage spinel, and the quartz-feldspar matrix by a monomineralic corona of cordierite (Figure 4.5). This texture shows the breakdown of formerly coexisting orthopyroxene + sillimanite into cordierite after melt loss. The inferred peak equilibrium assemblage for Domain 2 is: orthopyroxene, sillimanite, quartz, plagioclase, K-feldspar, ilmenite and liquid.

As well as occurring as a monomineralic corona around sapphirine and orthopyroxene (Figure 4.3 and Figure 4.7), cordierite is also preserved as pervasive symplectites with K-feldspar and quartz, which are interpreted to have replaced prograde/peak garnet (Figure 4.8).

Magnetite commonly occurs associated with sapphirine, sillimanite and contains exsolved hercynitic spinel. Ilmenite is almost pure ilmenite in this sample with an X_{ilm} of 0.97. Spinel has X_{herc} component of 0.49 with $X_{\mathrm{mt}} = 0.02$ and $X_{\mathrm{gah}} = 0.04$. Sapphirine is magnesian with a representative X_{Mg} of 0.66 (Table. 4.5). Through ideal analysis calculations (see Appendix in Taylor-Jones & Powell, 2010) on sapphirine, Fe^{3+} constitutes 0.27 cations pfu with Fe^{2+}, Al and Mg contents of 1.08, 8.17 and 2.62 respectively. Orthopyroxene in this sample is also significantly oxidised, containing 0.13 cations pfu of Fe^{3+}. Cordierite has an X_{Fe} of 0.29 and a calculated 0.06 cations pfu of Fe^{3+}. There are no porphyroblasts of cordierite, suggesting that cordierite was not present at the metamorphic peak, and is more likely to be a retrograde product with exsolved hercynite-spinel.

Table 4.5. Representative electron microprobe data for sample CJW20b from the Ihosy Formation.

	Silicates					Oxides		
Sample:	CJW20b	CJW020b	CJW020b	CJW020b	CJW020b	CJW020b	CJW020b	
Mineral:	sa	opx	cd (rim)	sill	pl	mt	ilm	sp
SiO_2	14.54	46.42	49.84	36.67	61.09	0.1	0.31	0.07
TiO_2	0.01	0.17	0.00	0.05	0.00	0.1	51.21	0.12
Al_2O_3	56.70	10.04	33.10	60.66	24.24	0.5	0.05	61.84
Cr_2O_3	0.12	0.00	0.00	0.04	0.06	0.4	0.04	0.43
FeO	10.60	16.08	2.49	0.12	0.06	31.2	38.97	21.25
Fe_2O_3	2.94	4.56	0.79	1.64	n.a	68.3	1.51	1.65
ZnO	0.00	0.00	0.00	0.00	0.02	0.1	0.02	1.92
MnO	0.68	1.28	0.30	0.00	0.00	0.1	7.26	1.40
MgO	14.38	21.34	11.36	0.02	0.00	0.1	0.04	11.41
CaO	0.01	0.08	0.00	0.00	0.26	0.0	0.00	0.00
Na_2O	0.01	0.03	0.06	0.00	8.17	0.0	0.00	0.04
K_2O	0.00	0.00	0.22	0.01	0.11	0.0	0.00	0.00
TOTAL	99.99	100.00	98.17	99.22	99.79	100.8	99.41	100.12
OXYGEN	20.00	6.00	18.00	5.00	8.00	4.0	3.00	4.00
Si	1.78	1.71	5.02	1.00	2.72	0.0	0.01	0.00
Ti	0.00	0.00	0.00	0.00	0.00	0.0	0.98	0.00
Al	8.17	0.44	3.93	1.96	1.27	0.0	0.00	1.95
Cr	0.01	0.00	0.00	0.00	0.00	0.0	0.00	0.01
Fe^{2+}	1.08	0.50	0.21	0.00	0.00	1.0	0.83	0.48
Fe^{3+}	**0.27**	**0.13**	**0.06**	**0.03**	0.00	**2.0**	**0.03**	**0.03**
Zn	0.00	0.00	0.00	0.00	0.00	0.0	0.00	0.04
Mn	0.07	0.04	0.03	0.00	0.00	0.0	0.16	0.03
Mg	2.62	1.17	1.71	0.00	0.00	0.0	0.00	0.46
Ca	0.00	0.00	0.00	0.00	0.29	0.0	0.00	0.00
Na	0.00	0.00	0.01	0.00	0.71	0.0	0.00	0.00
K	0.00	0.00	0.03	0.00	0.01	0.0	0.00	0.00
TOTAL	14.00	4.00	11.00	3.00	5.00	3.00	2.00	3.00
X_{Mg}	0.66	0.65	0.86	0.02		0.00	0.00	0.47
X_{Mg*}	0.71	0.70	0.89	0.24		0.00	0.00	0.49
X_{Fe}	0.29	0.30	0.11	0.76		1.00	1.00	0.51
X_{an}					0.29			

Representative value chosen (not mean). Cation ratios as described in text.
Fe^{3+} values from ideal analysis (sa, opx) and stoichiometric calculation (cd, sill, mt, ilm, sp)

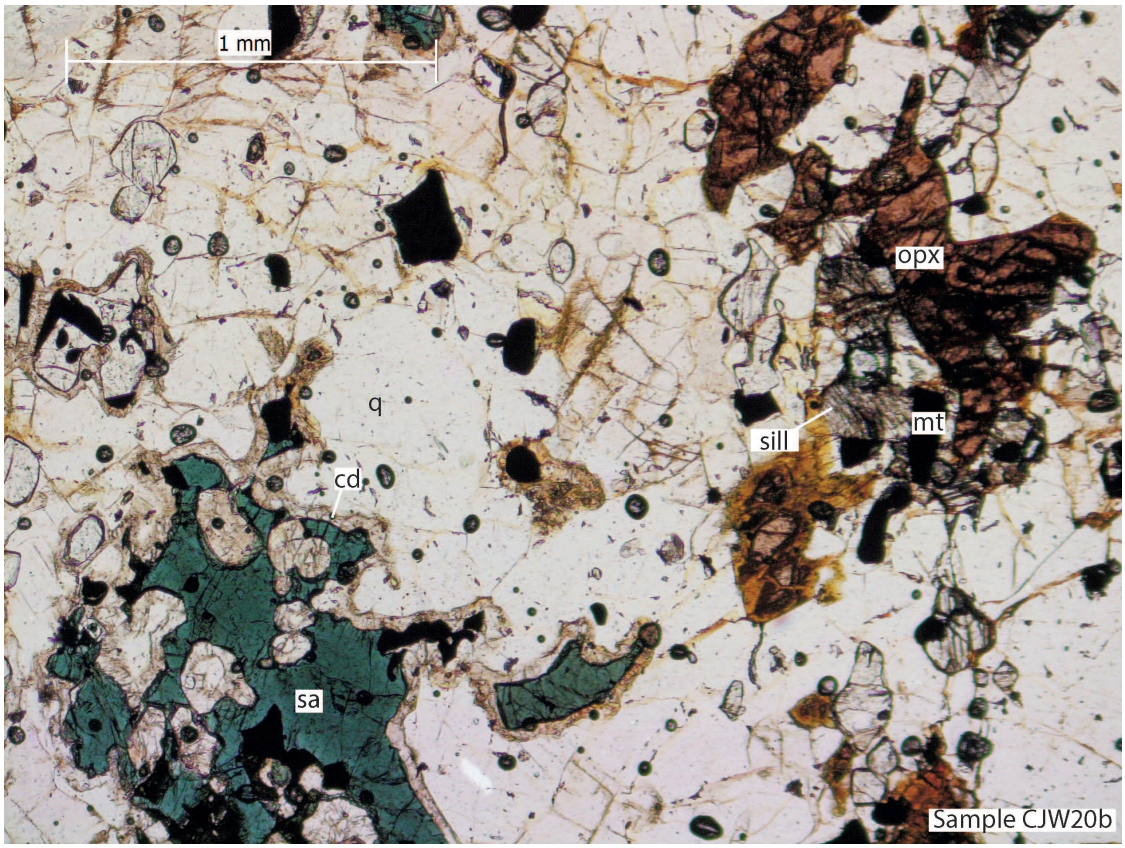

Figure 4.2. Textures in sample CJW20b. Spatial separation of the ferromagnesian minerals sapphirine and orthopyroxene. Minerals are separated by a quartz and feldspar matrix. Domain 1: sa–q–mt–liq; Domain 2: opx–sill.

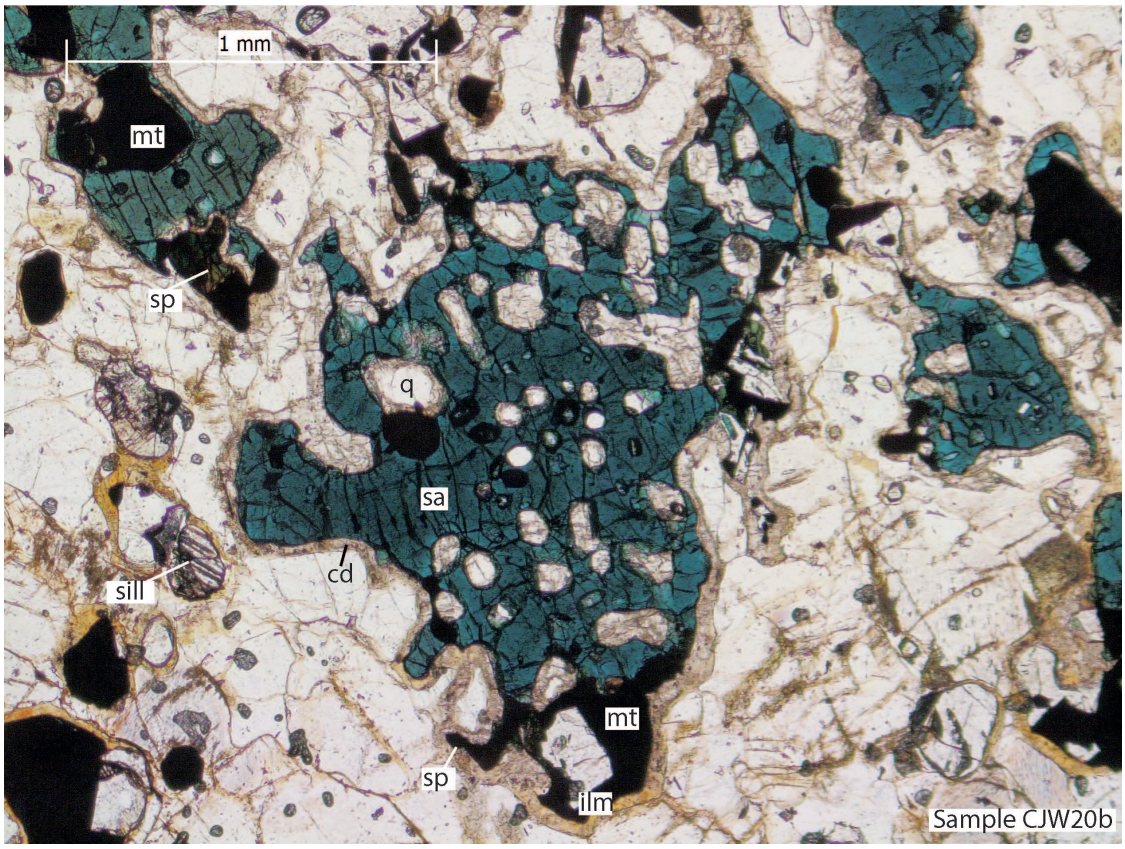

Figure 4.3. Textures in sample CJW20b. Sapphirine surrounded by a monomineralic corona of cordierite, separating the sapphirine from quartz. See BSE below for oxides. Domain 1: sa–q–mt–liq.

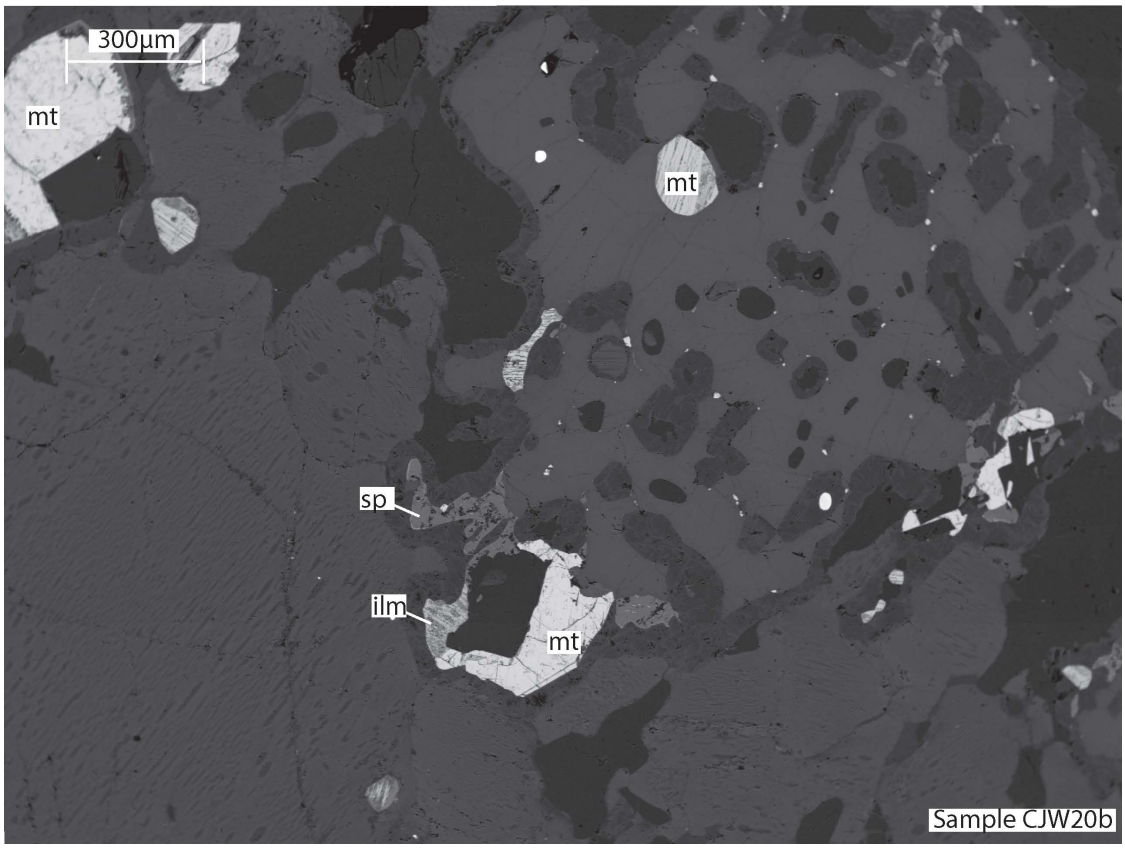

Figure 4.4. Back-scattered electron (BSE) image of sapphirine texture with a magnetite inclusion surrounded by monomineralic corona of cordierite from sample CJW20b. Other oxides include exsolved ilmenite and late-stage hercynite-spinel. Rotated view of Figure 4.3. Domain 1: sa–q–mt–liq.

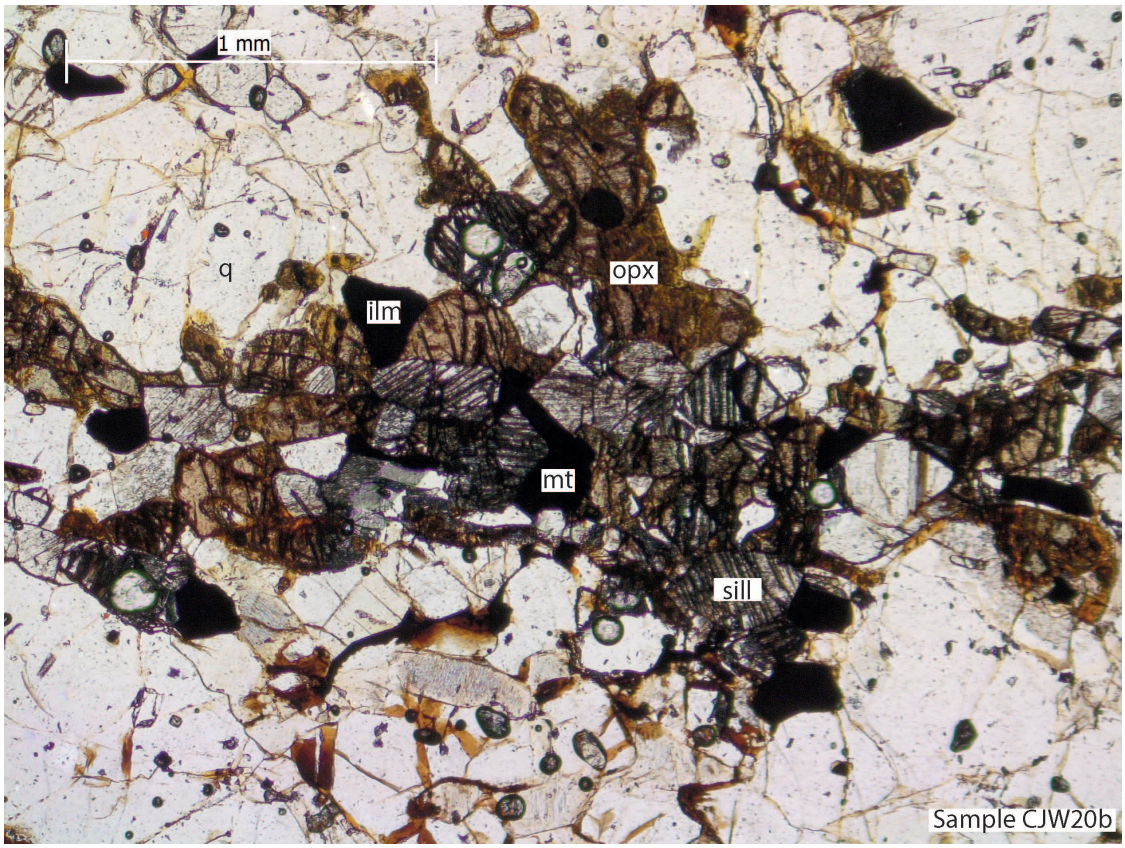

Figure 4.5. Textures in sample CJW20b. Orthopyroxene intergrown with prismatic sillimanite. Note that the coexisting opx and sill are not separated by cordierite, compared with the same texture in Figure 4.7. Oxides are magnetite. Domain 2: opx–sill

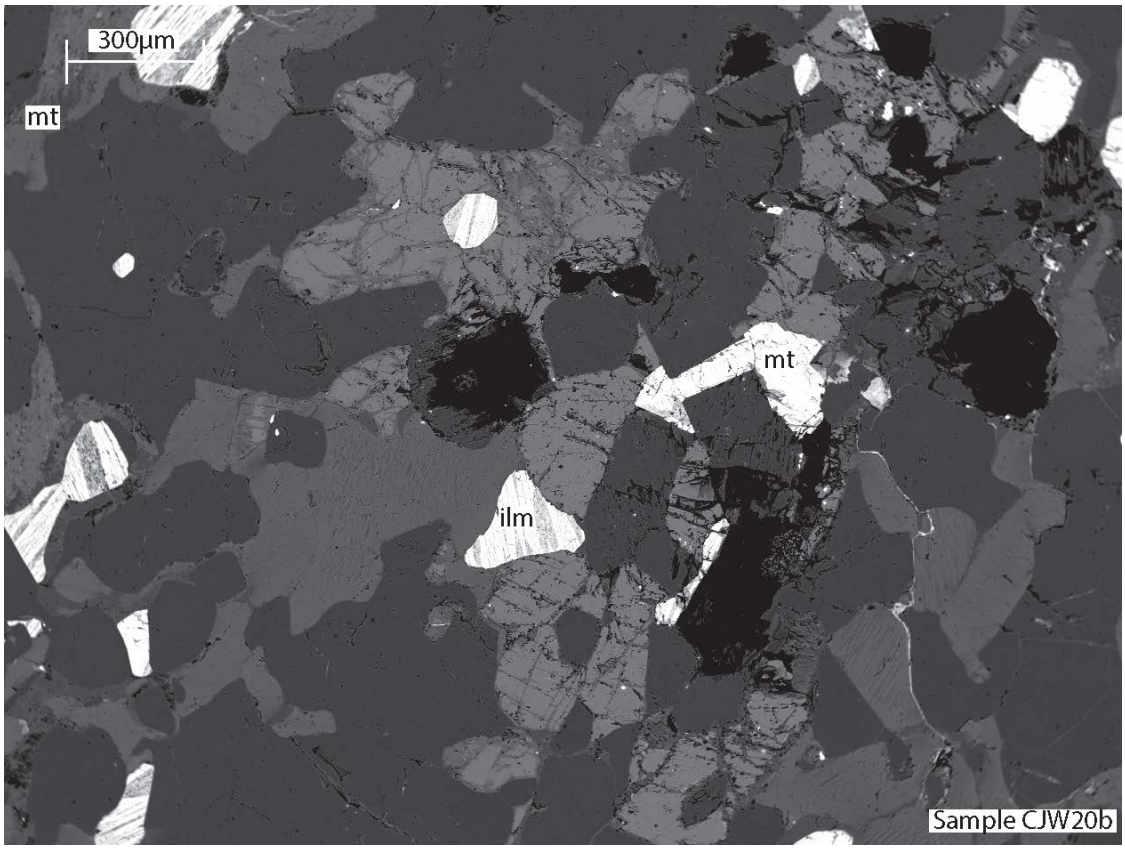

Figure 4.6. Back-scattered electron (BSE) image of orthopyroxene–sillimanite texture with a magnetite and exsolved ilmenite inclusion from sample CJW20b. Rotated view of Figure 4.5 Domain 2: opx–sill.

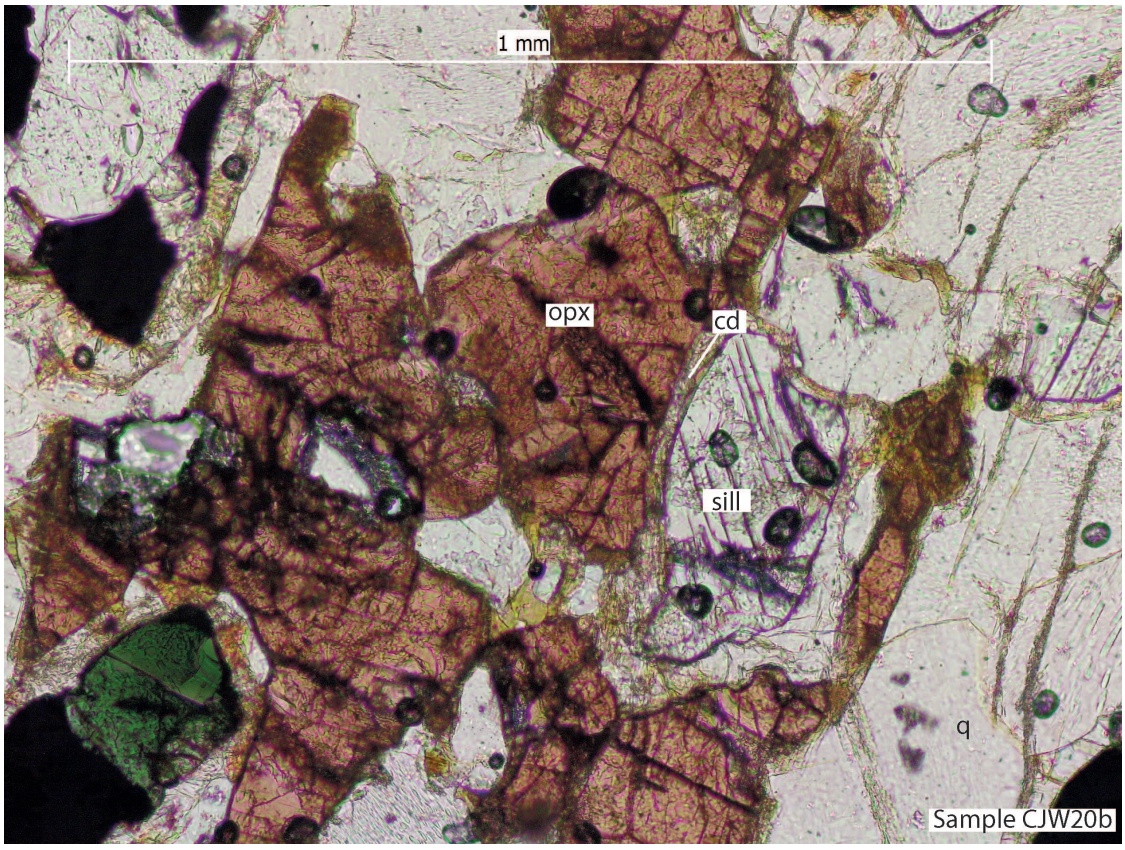

Figure 4.7. Higher magnification photomicrograph of orthopyroxene in sample CJW20b. In contrast to the orthopyroxene texture in Figure 4.5, orthopyroxene is separated from sillimanite and oxides by a monomineralic corona of cordierite. Domain 3: opx–sill–liq.

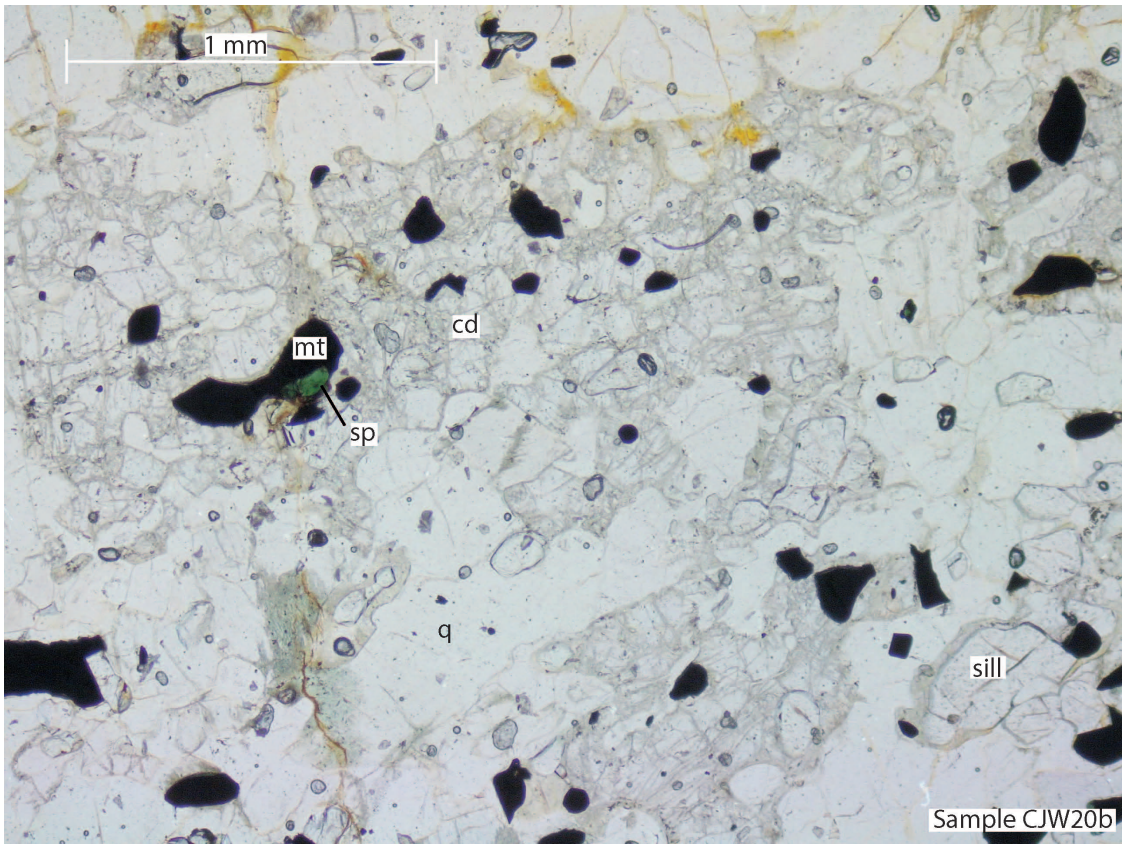

Figure 4.8. Textures in sample CJW20b. Cordierite is also preserved as pervasive symplectites with K-feldspar and quartz, which are theorised to have replaced prograde/peak garnet. Cordierite is also associated with magnetite, ilmenite and late-stage spinel.

.

4.5.2 Thermodynamic modelling of microdomains

The sapphirine-bearing sample can be used to constrain the *P–T* evolution of the Ihosy Formation. As this sample is spatially inhomogeneous, calculated phase equilibria for a crushed hand-specimen bulk composition will not accurately reflect the evolution of the preserved mineral assemblages. For modelling purposes, the key assemblages to be modelled are;

- Domain 1: sapphirine–magnetite–quartz–liq plus plagioclase + K-feldspar + ilmenite ('sa–q–mt–liq')
- Domain 2: orthopyroxene–sillimanite plus quartz + plagioclase + K-feldspar + ilmenite ('opx–sill')
- Domain 3: orthopyroxene–sillimanite–liquid plus quartz + plagioclase + K-feldspar + ilmenite ('opx–sill–liq')

with cordierite and exsolved spinel growing in the retrograde history.

The chemical system NCKFMASHTO is too complex for *P–T* petrogenetic grids and compatibility diagrams, and must be reduced to KFMASHTO. In this transition, plagioclase is lost and the stability of melt and garnet is restricted to higher pressure and temperature conditions as noted above. While less geologically realistic, this reduction in system allows an extra dimension of analysis to see what the effect of different *P–T* conditions has over multiple bulk compositions (and thus microdomains). For these calculations, the minerals sillimanite, plagioclase, quartz and K-feldspar are taken to be in-excess. For the compatibility diagrams, melt and cordierite are also (interchangeably) in-excess in order to investigate domainal behaviour involving these minerals.

A KFMASHTO *P–T* projection in Figure 4.9 presents the possible univariant reactions for rocks in this system between 780°C and 1020°C and over a range of 4.4 kbar to 9 kbar. Without taking bulk composition into account, the stable minerals on each side of univariant lines can give an indication of the conditions at which combinations of minerals are stable. If the rock sits on one side of a reaction line, then the possible stable mineral assemblages include all of the phases on that side of the reaction, plus all but one of the reactions on the opposite side (for a divariant assemblage in the model system). If not, the univariant cannot be seen by the assemblage and the information in the univariant is not relevant in interpreting a mineral assemblage (an example *P–T* grid is given in Figure 2.2 in Chapter 2).

To investigate the high-temperature assemblage, focus is drawn to between 900–1010°C and 6.5–7.5 kbar (Figure 4.10). As with the previous phase diagrams, sillimanite is in-excess for all the displayed univariant reactions, however the position of sillimanite on the side of the univariant (as determined using Schreinemakers' Rule for determining relative stabilities around an invariant point - see Figure 2.1 in Chapter 2) is given for key univariants discussed in the text. This is done in order to show the possible stable assemblages both involving sillimanite, and not involving sillimanite. A possible retrograde path for the sample is also drawn in Figure 4.10 which is explored further with application of compatibility diagrams. To illustrate this in the context of sample CJW20b, and to constrain where in *P–T* the sample attained its peak conditions, the following univariant lines are considered to provide petrological constraints:

opx+sill+mt=g+sa This reaction is degenerate, and in this case means that the presence or absence of melt does not affect whether this reaction is seen by the rock. Crossing this reaction up temperature results in the appearance of sapphirine. The possible assemblages on the high temperature side of the reaction are: g+sa+opx+sill; g+sa+sill+mt; and g+sa+opx+mt.

opx+sill+liq=g+sa+cd The sample must be on the high pressure side of this reaction as this is the low temperature limit in KFMASHTO for co-existing opx + sill + liq. On this side, the possible divariant assemblages are: opx+sill+liq+g+sa; opx+sill+liq+g+cd and opx+sill+liq+sa+cd. Cordierite has been interpreted as retrograde and overgrows orthopyroxene and sillimanite when in the presence of melt.

g+sill+mt=sa+sp It can be argued that the sample must be on the low temperature side of this reaction. This is another degenerate reaction (the presence or absence of melt does not factor). As spinel is interpreted to be a retrograde mineral, the rock must not have crossed this reaction to higher temperature to reach the peak.

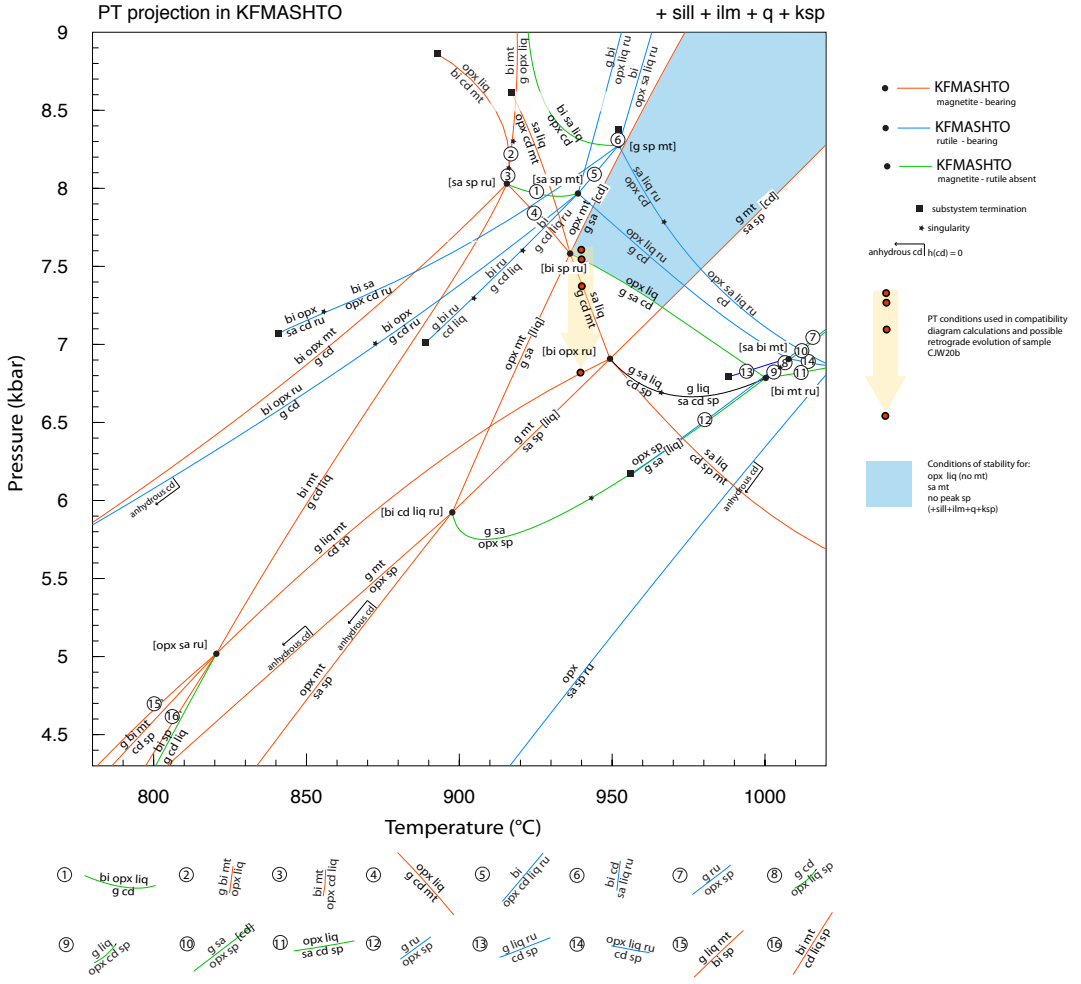

Figure 4.9. *P–T* projection calculated in KFMASHTO with sillimanite, ilmenite, quartz and K-feldspar in-excess. Univariant reactions in KFMASHTO are displayed, with terminations in sub-systems as solid squares. Reactions involving magnetite (red) and rutile (blue) are distinguished, as are reactions that are magnetite- and rutile- absent (green). Shaded blue is the inferred peak *P–T* conditions required to form the mineral assemblages observed in sample CJW20b. Yellow arrow shows a possible decompression path from peak for sample CJW20b and the red dots are the locations of the calculated compatibility diagrams in Figures 4.11 - 4.13. A larger scale version of this path is shown in Figure 4.10.

Within the boundary of these three univariant reactions, all the texturally distinct microdomains in sample CJW20b can be developed, with this field shown as a blue overlay in Figure 4.9 and zoomed in to higher *PT* in Figure 4.10. A compatibility diagram showing all the possible stable assemblages at a position within this boundary is shown in Figure 4.11. Mineral chemistry

can be used to further constrain the univariant line boundary for the peak mineral assemblage in a more realistic chemical system. The measured composition of plagioclase in this sample, ca(pl) of 0.29 (anorthite content from Table 4.5), can be input to see where the lowest P–T boundary plots in NCKFMASHTO. With this input, the assemblage is stabilised down P–T (see extension of blue field in Figure 4.10 and provides a lower temperature boundary for the formation of peak minerals for the bulk composition of this sample. This line can be added to the overlapping non-sapphirine-bearing stability fields to provide a down-temperature constraint for the Ihosy Formation metapelites, the summary of which is found in Figure 4.21.

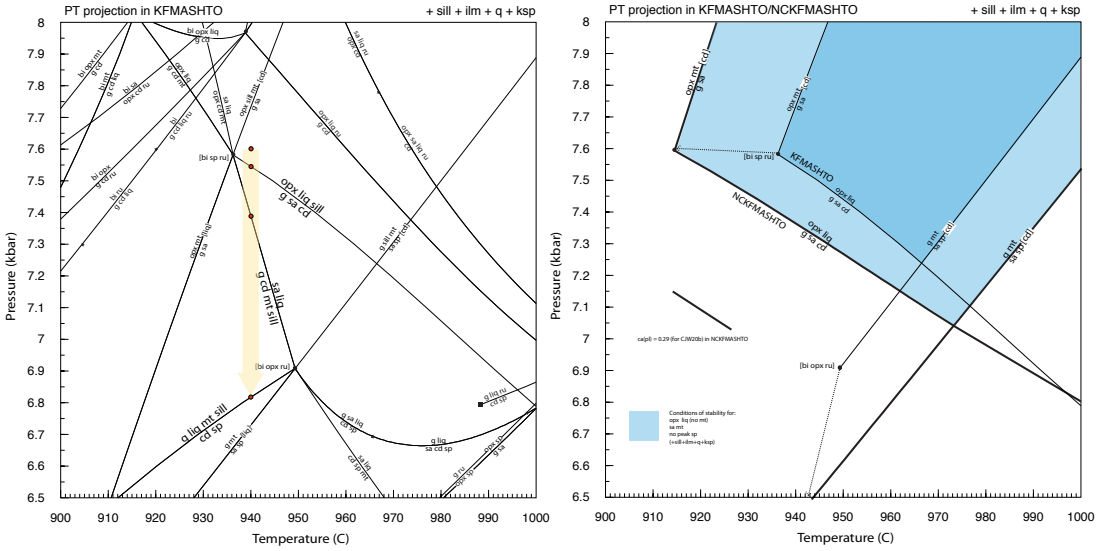

Figure 4.10. P–T projection calculated in KFMASHTO with sillimanite, ilmenite, quartz and K-feldspar in-excess. Univariant reactions in KFMASHTO are displayed, with terminations in sub-systems as solid squares. Left: A close-up view from Figure 4.9 showing a possible decompression path from peak for sample CJW20b and the red dots are the locations of the calculated compatibility diagrams in Figures 4.11 - 4.13. While sillimanite is deemed to be in-excess for the calculation of this figure, the position of sillimanite on the relevant side of the univariant reaction is added for key reactions (larger font). Right: The displacement in P–T of the key reactions bounding the inferred peak P–T conditions required to form the mineral assemblages observed in sample CJW20b when the system takes into account plagioclase (thus the chemical system of NCKFMASHTO). The NCKFMASHTO reactions are calculated for a ca(pl) of 0.29 (anorthite content from Table 4.5) and extends the stability of the peak assemblages down pressure and temperature.

Compatibility diagrams

Each of the microdomains relate to one or more of the peak metamorphic minerals that react in the retrograde path, effectively reacting in their own microdomain. Sapphirine and orthopyroxene are involved in separate reactions in the retrograde involving the assemblages sa+mt+liq+q (cd retrograde); opx+sill (no cordierite); opx+sill+liq (cd retrograde) – all with q+pl+ksp+ilm in-excess). These assemblages can be plotted on compatibility diagrams at the same P–T conditions.

Compatibility diagrams (Figures 4.11 to 4.14) have been calculated in KFMASHTO to demonstrate the stable mineral assemblages crossing key univariant reactions on the P–T projection in Figure 4.9. Sillimanite, quartz, K-feldspar and ilmenite are considered in-excess in all calculations. Melt is considered in-excess for the initial calculations at higher pressure, while at lower pressures the calculations are split into melt-present and melt-absent microdomains. Each compatibility diagram is calculated for a fixed P–T, allowing stable mineral assemblages to be investigated as

a function of composition. The compatibility diagrams are calculated at a peak *P–T* above the opx+sill+liq=g+sa+cd univariant. They then show the possible variation in mineral assemblage with decreasing pressure to model growth of cordierite rims in Domains 1 and 3.

The *P–T* evolution of the preserved assemblages in CJW20b is considered to start at peak *P–T* conditions where the rock has equilibrated in two microdomains. The first compatibility diagram (Figure 4.11) calculated at 940°C at 7.6kbar on the high pressure side of the opx+sill+liq=g+sa+cd univariant, allows stable microdomains involving the assemblages opx+liq+sill and sa+mt+q+liq. Minerals are less hydrous at high-temperature and there is no free H_2O.

Evolution of Domain 1:

sa–mt (+q +liq) is a stable trivariant assemblage at 7.6 kbar, 940°C with melt and an intermediate range of oxidation state and magnesian content. On decompression to the low pressure side of the opx+sill+liq=g+sa+cd reaction, cordierite can develop in the presence of melt. Upon further decompression beyond the sa+liq=g+cd+mt univariant, sapphirine disappears, however if the rock was to lose melt, then the system can move into a melt-absent microdomain where cordierite rims are preserved around peak sapphirine and magnetite. (Key compatibility diagrams are in Figure 4.11 and Figure 4.13).

Evolution of Domain 2:

opx (+sill) will form if the fluid is lost completely before the opx+sill+liq=g+sa+cd is reached on decompression. With no melt to provide H_2O to stabilise cordierite, no cordierite will grow. This is the first microdomain to 'freeze' in place (Key compatibility diagram in Figure 4.11).

Evolution of Domain 3:

opx (+liq +sill) is a stable univariant assemblage at 7.6 kbar, 940°C with melt in a small field that is more reduced than the sapphirine-bearing microdomain. On decompression to the low pressure side of the opx+sill+liq=g+sa+cd reaction, orthopyroxene disappears from the system. To retain an opx–sill texture, melt must be lost. If the rock was to lose melt, having already stabilised cordierite, then the system can move into a melt-absent microdomain where cordierite rims are preserved around peak orthopyroxene and sillimanite. (Key compatibility diagrams are in Figure 4.11 and Figure 4.12).

At this point, the rock is melt-absent at each microdomain, with each microdomain preserved at different *PT* points as melt is lost from the local assemblage. A final compatibility diagram, drawn upon further decompression shows that spinel can form in the absence of melt as the g+liq+mt+sill=cd+sp univariant is crossed (Figure 4.14) This could explain the exsolution textures from magnetite seen across the sample.

Summary

In summary, a possible path of isothermal decompression at 940°C from 7.6 kbar to 6.8 kbar produces an evolution of possible microdomains in agreement with those observed in sample CJW20b. However, this is only a minimum pressure and temperature as the opx+sill+sill=g+sa+cd univariant is only a low *PT* boundary. In this scenario the rock equilibrated post peak into multiple microdomains upon decompression with the loss of melt (i.e. the melt crystallised in a reaction relationship with the minerals with which it was equilibrating). The H_2O that was in the melt goes to stabilise cordierite in a retrograde reaction.

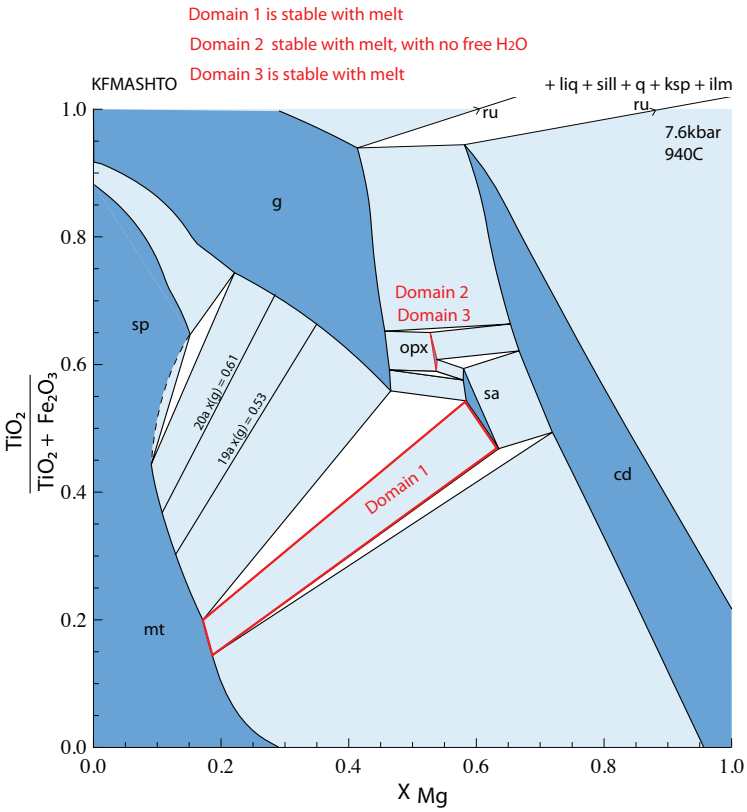

Figure 4.11. Compatibility diagram calculated in KFMASHTO with melt, sillimanite, quartz, K-feldspar and ilmenite in-excess. *P–T* of 7.6kbar and 940°C chosen as within the inferred peak field in Figures 4.9 and 4.10 for sample CJW20b. Red boxes show stable domainal assemblages. Changes in mineral assemblage through decompression at 940°C is shown in Figures 4.12 and 4.13.

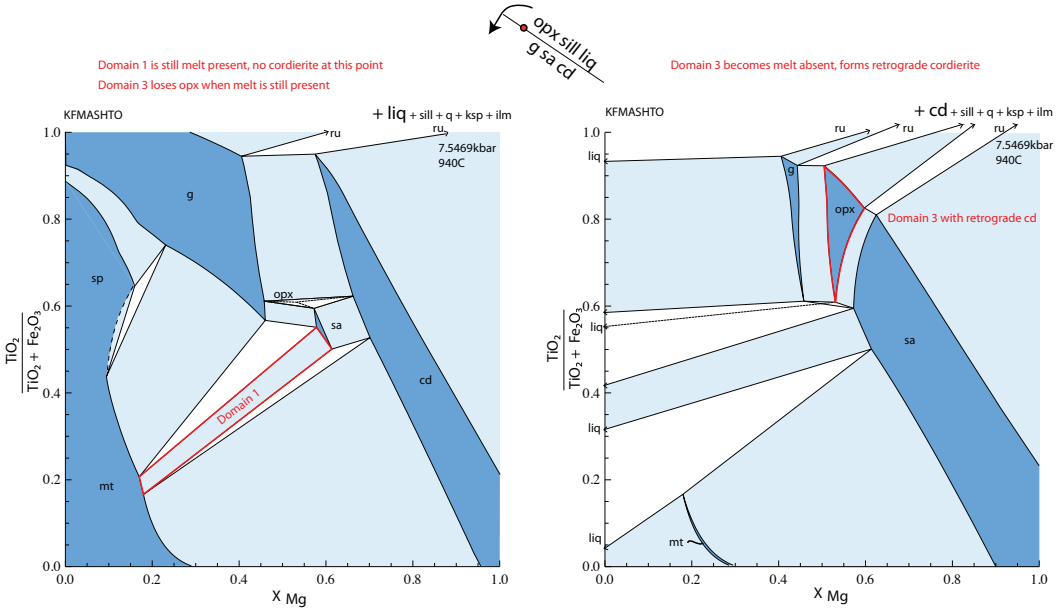

Figure 4.12. Compatibility diagram calculated in KFMASHTO with melt **or** cordierite, sillimanite, quartz, K-feldspar and ilmenite in-excess. As the rock is decompressed, orthopyroxene disappears from the system in favour of g-sa-cd (left image). However, as this diagram is calculated with melt and sillimanite in-excess, it only shows that we cannot have orthopyroxene with both these phases. As the univariant opx+sill+liq=g+sa+cd is crossed, opx can still be retained with either sill or liq (not both). To retain the opx+sill texture, melt must be lost and thus can have coexisting opx-sill-g-sa-cd. If the rock sees this reaction, cordierite will form as a replacement mineral (i.e. the cordierite corona texture) with water addition into cordierite occurring due to decreasing mode of melt. This brings the rock into melt absent with cordierite in-excess (right image). It is also possible for the melt to be completely lost before this reaction is reached down pressure. As melt is no longer in-excess, this reaction is not seen, and cordierite rims do not form. Fine-dotted line shows which tie-triangle disappears as the univariant is crossed down pressure.

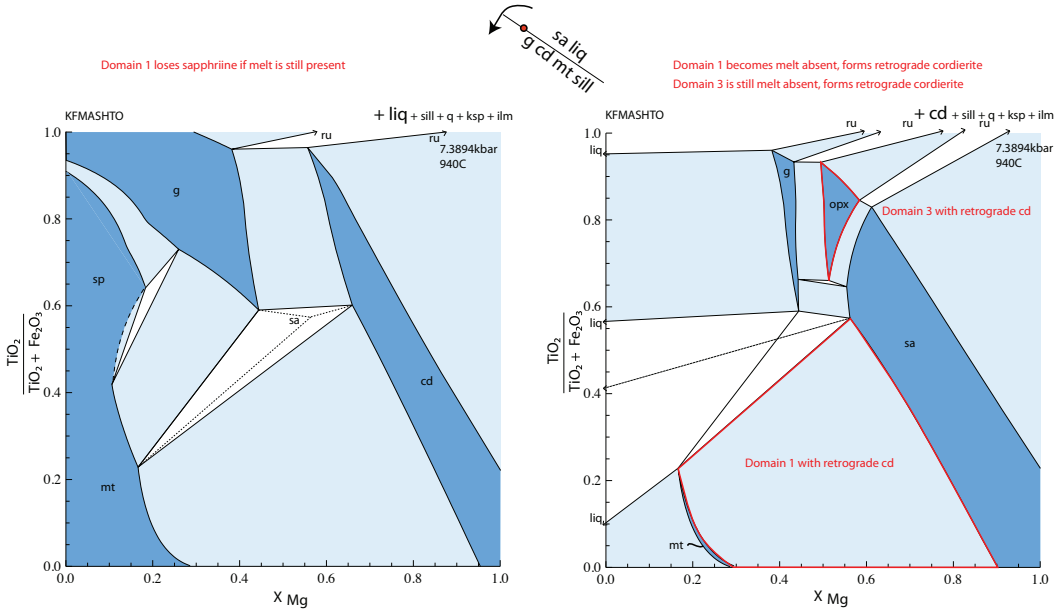

Figure 4.13. Compatibility diagram calculated in KFMASHTO with melt **or** cordierite, sillimanite, quartz, K-feldspar and ilmenite in-excess. The sa-mt-liq texture is stable during decompression until the univariant reaction sa+liq = g+cd+mt+sill is reached (left image). Prior to this, the tie-triangle involving sa-mt-cd-liq texture expands (continuous reaction), and can bring in cd as a replacement mineral. Decompression past the sa+liq=g+cd+mt+sill means that sapphirine is no longer stable with melt. Coexisting g-sa-cd-mt-sill is stable down pressure, and the system moves to melt absent with cordierite in-excess (right image). Fine-dotted line shows which tie-triangle disappears down pressure.

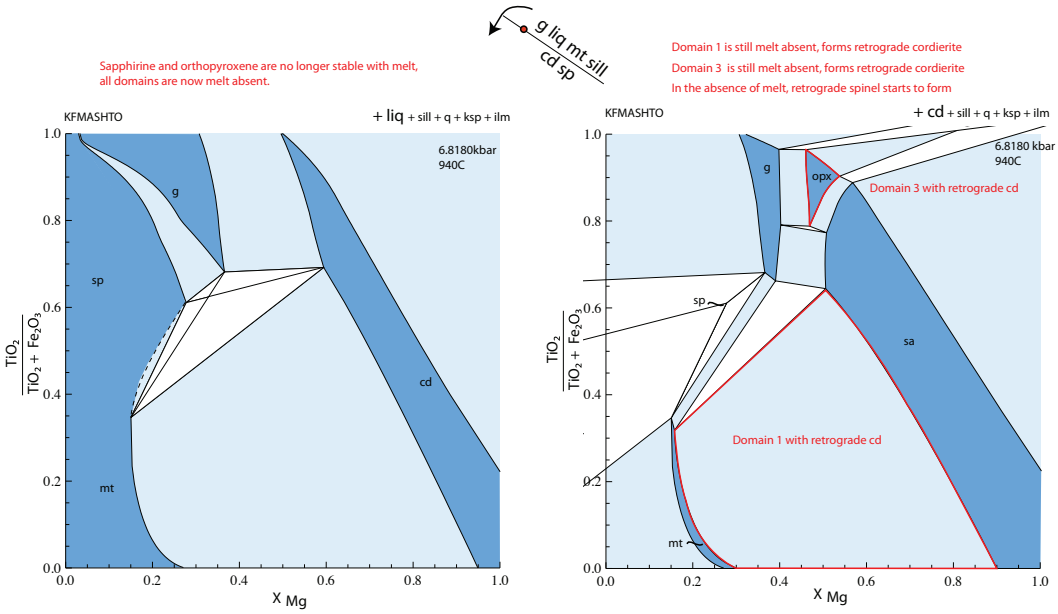

Figure 4.14. Compatibility diagram calculated in KFMASHTO with melt **or** cordierite, sillimanite, quartz, K-feldspar and ilmenite in-excess. By the time the rock decompresses beyond the g+liq+mt+sill = cd+sp univariant, neither orthopyroxene nor sapphirine with coexisting sillimanite can be present with melt. In a system with cordierite in-excess, spinel enters the assemblage for the first time, coexisting with garnet, melt and magnetite.

4.5.3 Non-sapphirine-bearing samples

The non-sapphirine-bearing metapelites (CJW19a, CJW19b, CJW20a) contain coarse-grained, irregularly shaped porphyroblasts of garnet evenly distributed throughout the rock, which are variably rimmed with coarse-grained cordierite coronae. Large cordierite 'clots' with coarse inclusions of garnet and sillimanite are optically continuous with the cordierite coronae. Minor biotite is apparent. Spinel is present occurring as single grains as well as intergrown and exsolved from magnetite (Figure 4.15 to Figure 4.17).

Representative mineral analyses for the non-sapphirine-bearing samples can be found in Tables 4.6 to 4.8. Spinel contains moderate X_{herc} of 0.57–0.60 with small contributions of X_{mt} of 0.03–0.04. Ilmenite is not as pure as in the sapphirine-bearing sample, with an X_{ilm} of 0.85–0.89. X_{alm} sits between 0.52 and 0.57, with X_{py} between 0.37 and 0.43. X_{gr} and X_{spss} are much lower, between 0.02–0.03 and 0.03–0.07 respectively. Fe^{3+} is measured at 0.00 to 0.11 cations pfu. Cordierite has an X_{Fe} of 0.08 to 0.18 and between 0.02 and 0.12 cations pfu of Fe^{3+}.

The interpreted peak mineral assemblage in samples CJW19a, CJW19b and CJW20a is garnet, sillimanite, magnetite, quartz, plagioclase, K-feldspar, ilmenite and melt. The timing of minor relicts of biotite is inconclusive. Biotite could be relicts of the prograde path not consumed via melting reactions, however may also be interpreted as a retrograde mineral. Spinel is interpreted as retrograde, as a result of exsolution from magnetite post peak.

Table 4.6. Representative electron microprobe data for sample CJW19a from the Ihosy Formation.

	Silicates			Oxides		
Sample:	CJW19a	CJW19a	CJW19a	CJW19a	CJW19a	CJW19a
Mineral:	g	cd (rim)	sill	mt	ilm	sp
SiO_2	39.71	50.38	37.01	0.25	0.19	0.20
TiO_2	0.00	0.03	0.02	0.02	48.59	0.00
Al_2O_3	22.28	33.60	60.90	0.30	0.08	61.08
Cr_2O_3	0.03	0.02	0.00	0.18	0.00	0.24
FeO	23.71	1.90	0.08	31.48	42.60	25.30
Fe_2O_3	1.93	1.65	1.66	67.96	7.21	3.08
ZnO	na	na	na	0.00	0.00	0.16
MnO	1.57	0.07	0.03	0.02	0.83	0.25
MgO	11.79	11.99	0.05	0.00	0.27	10.85
CaO	0.73	0.00	0.00	0.01	0.00	0.00
Na_2O	0.04	0.12	0.01	0.00	0.00	0.00
K_2O	0.01	0.05	0.03	0.00	0.00	0.00
TOTAL	101.81	99.81	99.79	100.21	99.77	101.16
OXYGEN	12.00	18.00	5.00	4.00	3.00	4.00
Si	2.97	4.99	1.01	0.01	0.00	0.01
Ti	0.00	0.00	0.00	0.00	0.93	0.00
Al	1.96	3.92	1.95	0.01	0.00	1.92
Cr	0.00	0.00	0.00	0.01	0.00	0.01
Fe^{2+}	1.48	0.16	0.00	1.01	0.90	0.56
Fe^{3+}	**0.11**	**0.12**	**0.03**	**1.96**	**0.14**	**0.06**
Zn	0.00	0.00	0.00	0.00	0.00	0.00
Mn	0.10	0.01	0.00	0.00	0.02	0.01
Mg	1.31	1.77	0.00	0.00	0.01	0.43
Ca	0.06	0.00	0.00	0.00	0.00	0.00
Na	0.01	0.02	0.00	0.00	0.00	0.00
K	0.00	0.01	0.00	0.00	0.00	0.00
TOTAL	8.00	11.00	3.00	3.00	2.00	3.00
X_{Mg}		0.86	0.05	0.00	0.01	0.41
X_{Mg*}	0.47	0.92	0.52	0.00	0.01	0.43
X_{Fe}	0.53	0.08	0.48	1.00	0.99	0.57
X_{alm}	0.52					
X_{gr}	0.02					
X_{py}	0.43					
X_{spss}	0.03					

Table 4.7. Representative electron microprobe data for sample CJW19b from the Ihosy Formation.

	Oxides			Silicates	
Sample:	CJW19b	CJW19b	CJW19b	CJW19b	CJW19b
Mineral:	g	cd	mt	ilm	sp
SiO_2	39.35	49.59	0.24	0.12	0.18
TiO_2	0.00	0.00	0.05	48.11	0.00
Al_2O_3	22.48	33.14	1.93	0.05	59.72
Cr_2O_3	0.05	0.02	0.20	0.00	0.24
FeO	23.91	3.31	31.75	41.19	26.18
Fe_2O_3	1.60	1.38	66.01	8.60	4.18
ZnO	0.00	0.00	0.02	0.00	0.21
MnO	3.31	0.18	0.02	1.87	0.62
MgO	10.34	11.07	0.00	0.18	9.84
CaO	1.06	0.04	0.01	0.00	0.00
Na_2O	0.00	0.08	0.00	0.00	0.00
K_2O	0.00	0.00	0.00	0.00	0.00
TOTAL	102.11	98.82	100.23	100.13	101.17
OXYGEN	12.00	18.00	4.00	3.00	4.00
Si	2.96	4.99	0.01	0.00	0.00
Ti	0.00	0.00	0.00	0.91	0.00
Al	1.99	3.93	0.09	0.00	1.90
Cr	0.00	0.00	0.01	0.00	0.01
Fe^{2+}	1.50	0.28	1.01	0.87	0.59
Fe^{3+}	0.09	0.10	1.89	0.16	0.08
Zn	0.00	0.00	0.00	0.00	0.00
Mn	0.21	0.02	0.00	0.04	0.01
Mg	1.16	1.66	0.00	0.01	0.40
Ca	0.09	0.00	0.00	0.00	0.00
Na	0.00	0.02	0.00	0.00	0.00
K	0.00	0.00	0.00	0.00	0.00
TOTAL	8.00	11.00	3.00	2.00	3.00
X_{Mg}		0.81	0.00	0.01	0.37
X_{Mg*}	0.44	0.86	0.00	0.01	0.40
X_{Fe}	0.56	0.14	1.00	0.99	0.60
X_{alm}	0.52				
X_{gr}	0.03				
X_{py}	0.38				
X_{spss}	0.07				

Table 4.8. Representative electron microprobe data for sample CJW20a from the Ihosy Formation.

	Silicates			Oxides		
Sample:	CJW20a	CJW20a	CJW20a	CJW20a	CJW20a	CJW20a
Mineral:	g	cd (rim)	sill	mt	ilm	sp
SiO_2	39.65	49.40	36.98	0.68	0.04	0.02
TiO_2	0.00	0.00	0.04	0.00	49.37	0.01
Al_2O_3	21.99	32.60	61.10	6.16	0.01	60.61
Cr_2O_3	0.03	0.04	0.11	0.18	0.01	0.24
FeO	26.91	4.17	0.04	32.54	43.17	26.60
Fe_2O_3	n.a	0.29	1.47	61.92	5.92	3.23
ZnO	0.00	0.01	0.00	0.05	0.00	0.20
MnO	1.48	0.09	0.00	0.02	0.78	0.15
MgO	9.80	10.77	0.04	0.57	0.21	9.78
CaO	0.97	0.01	0.00	0.01	0.00	0.00
Na_2O	0.01	0.07	0.02	0.04	0.02	0.00
K_2O	0.02	0.03	0.01	0.01	0.00	0.00
TOTAL	100.87	97.48	99.81	102.18	99.52	100.84
OXYGEN	12.00	18.00	5.00	4.00	3.00	4.00
Si	1.32	5.04	1.00	0.02	0.00	0.00
Ti	0.00	0.00	0.00	0.00	0.94	0.00
Al	0.65	3.92	1.96	0.26	0.00	1.93
Cr	0.00	0.00	0.00	0.01	0.00	0.01
Fe^{2+}	0.37	0.36	0.00	0.98	0.92	0.60
Fe^{3+}	**0.00**	**0.02**	**0.03**	**1.69**	**0.11**	**0.07**
Zn	0.00	0.00	0.00	0.00	0.00	0.00
Mn	0.02	0.01	0.00	0.00	0.02	0.00
Mg	0.24	1.64	0.00	0.03	0.01	0.39
Ca	0.02	0.00	0.00	0.00	0.00	0.00
Na	0.00	0.01	0.00	0.00	0.00	0.00
K	0.00	0.00	0.00	0.00	0.00	0.00
TOTAL	4.57	11.00	3.00	3.00	2.00	3.00
X_{Mg}		0.81	0.05	0.01	0.01	0.37
X_{Mg*}	0.39	0.82	0.66	0.03	0.01	0.40
X_{Fe}	0.61	0.18	0.34	0.97	0.99	0.60
X_{alm}	0.57					
X_{gr}	0.03					
X_{py}	0.37					
X_{spss}	0.03					

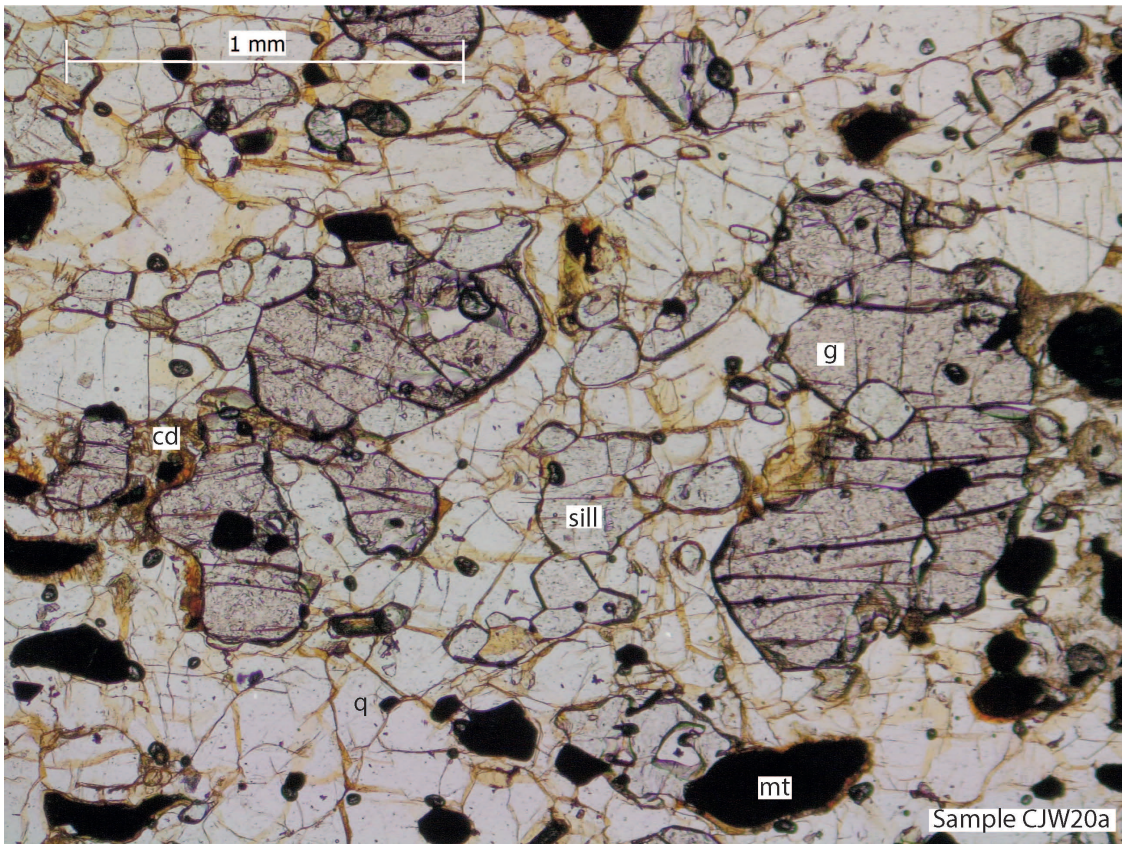

Figure 4.15. Textures in sample CJW20a. Garnet occurs as large porphyroblasts with inclusions of magnetite and ilmenite. Prismatic sillimanite occurs both in the quartz matrix and also sharing grain-boundaries with garnet. Cordierite develops variably around the edge of garnet.

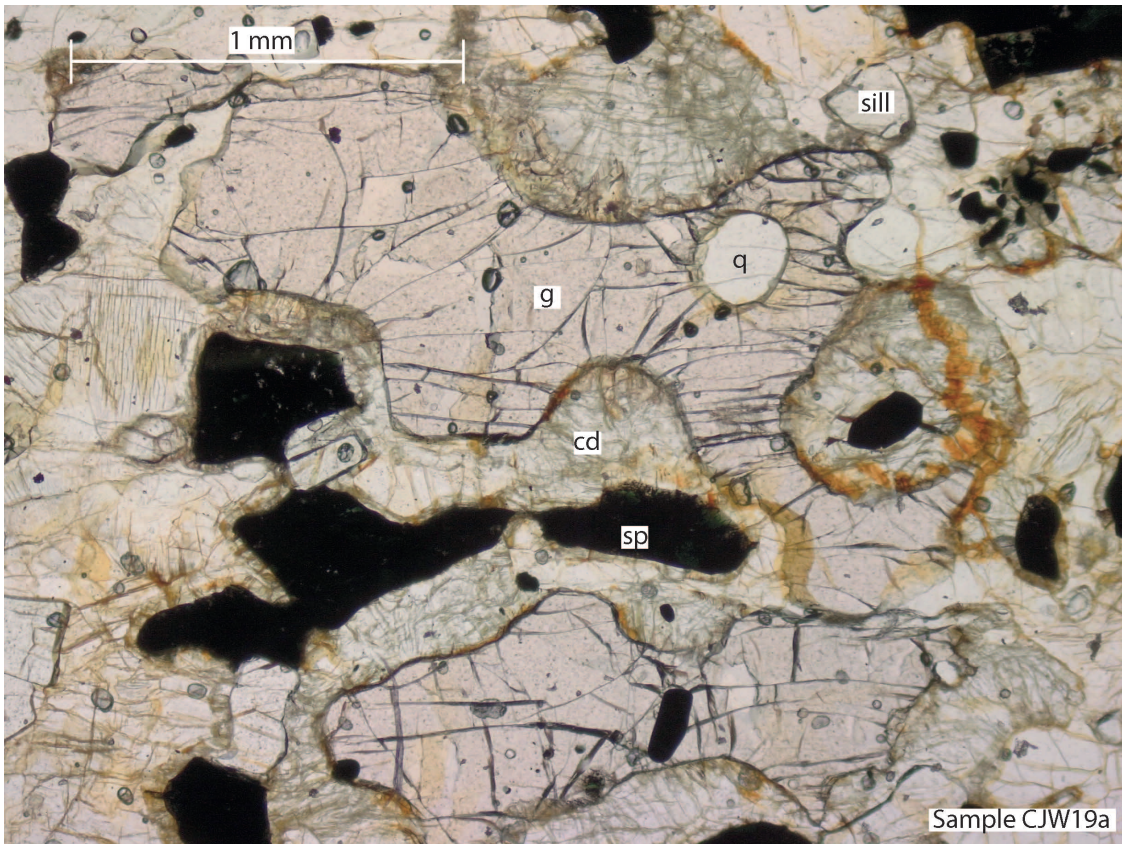

Figure 4.16. Textures in sample CJW19a. Garnet is surrounded by a monomineralic cordierite corona, separating garnet and spinel.

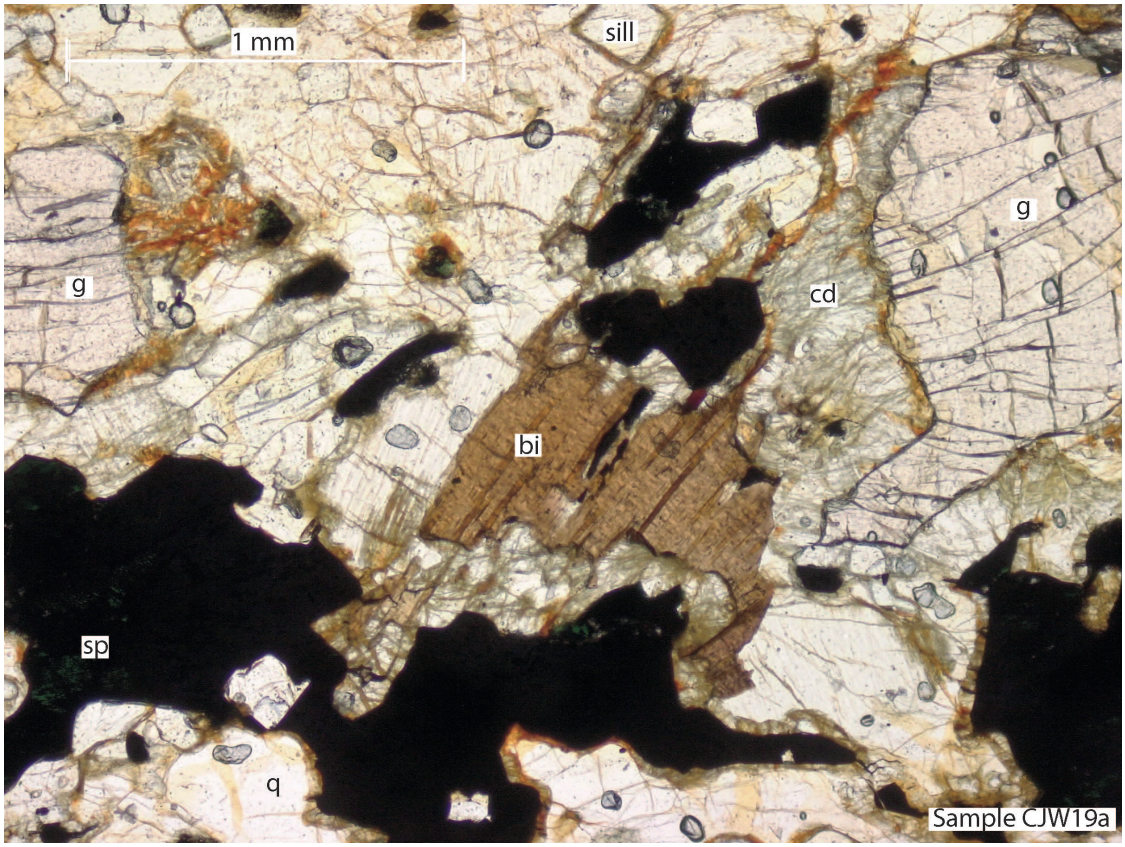

Figure 4.17. Textures in sample CJW19a. A rare grain of biotite surrounded by cordierite. Garnet is separated from biotite and spinel by cordierite.

4.5.4 Whole rock chemistry

XRF analysis was undertaken on 30 samples across southern Madagascar. Of interest to this study are four of these from the Ihosy Formation tabulated in Table 4.9 (though note that CJW20b is not an effective bulk composition for modelling purposes). The values for X_{Al} X_{Fe} ranges from 0.53 to 0.57 and 0.61 to 0.68 respectively. The bulk-rock compositions used for modelling have been converted from weight % oxides to molar % oxides. Table 4.9 gives results of titration and its calculated oxidation state as a maximum value. Analyses were converted to the NCKFMASHTO chemical system for phase equilibria modelling by disregarding minor amounts of MnO, Cr_2O_3 and P_2O_5. The amount of H_2O and O in the system is detailed in the following section.

Table 4.9. Whole-rock analyses in mol% for Ihosy Formation metapelites used in this study. Note: The whole-rock analysis for CJW20b is not used for modelling as the rock is interpreted as domainal. A whole rock bulk composition is used later in the Appendix to show how a pseudosection approach is ineffective.

Sample	**Ihosy Formation**			
	19a	**19b**	**20a**	**20b**
mol%				
SiO2	61.12	58.15	67.39	71.29
Al2O3	16.36	18.19	14.97	11.89
Fe2O3	3.63	3.97	2.37	1.16
FeO	5.51	5.56	4.68	5.01
MnO	0.19	0.18	0.14	0.14
MgO	5.37	6.14	3.99	2.88
CaO	0.56	0.73	0.99	0.45
Na2O	0.88	0.77	1.22	1.01
K2O	0.96	1.32	1.91	2.01
TiO2	1.11	1.17	0.78	0.69
LOI	4.5	3.99	1.68	3.61
Total	100.19	100.17	100.12	100.14
X_{Al}	0.53	0.54	0.58	0.57
X_{Fe}	0.63	0.61	0.64	0.68
X_K	0.52	0.63	0.61	0.67
X_{Ca}	0.24	0.26	0.24	0.13

4.5.5 Traditional pseudosection modelling for homogeneous rocks

All the samples for P–T modelling are chosen from within a small area. The rocks are of the same age but with different preserved mineral assemblages and so are interpreted to have shared metamorphic histories as well as experiencing the same peak P–T conditions. Three bulk compositions (CJW19a, CJW19b and CJW20a) are used to constrain peak P–T conditions for this area, by overlapping the observed peak mineral assemblage fields for each sample.

Modelling of non-sapphirine-bearing samples began using the titrated iron estimation for oxidation state and the LOI value for H_2O content. This produced pseudosections with no spinel and with inferred peak assemblages that form at a temperature too low to plot above the opx-sill-liq univariant line in KFMASHTO (see Figure 4.9) that is required for the peak assemblage of opx–sill in the sapphirine-bearing rocks. In order to produce a more meaningful result, the amount of modelled H_2O is decreased, with the implication that this will stabilise the feldspars, destabilise biotite and would move the solidus to higher temperature with the peak assemblage preserved just after the solidus. A 1.0 mol% of H_2O was settled upon to provide appropriate topologies with regards to solidus temperature and peak assemblage P–T. The solidus for this H_2O content is between 800–850°C at pressures between 7–10kbar.

The calculated P–T pseudosections for samples CJW19a, CJW19b and CJW20a are shown in Figures 4.18, 4.19 and 4.20 respectively. All three samples have a peak assemblage of garnet–sillimanite–magnetite–K-feldspar–plagioclase–quartz–ilmenite–melt. The pseudosections have sim-

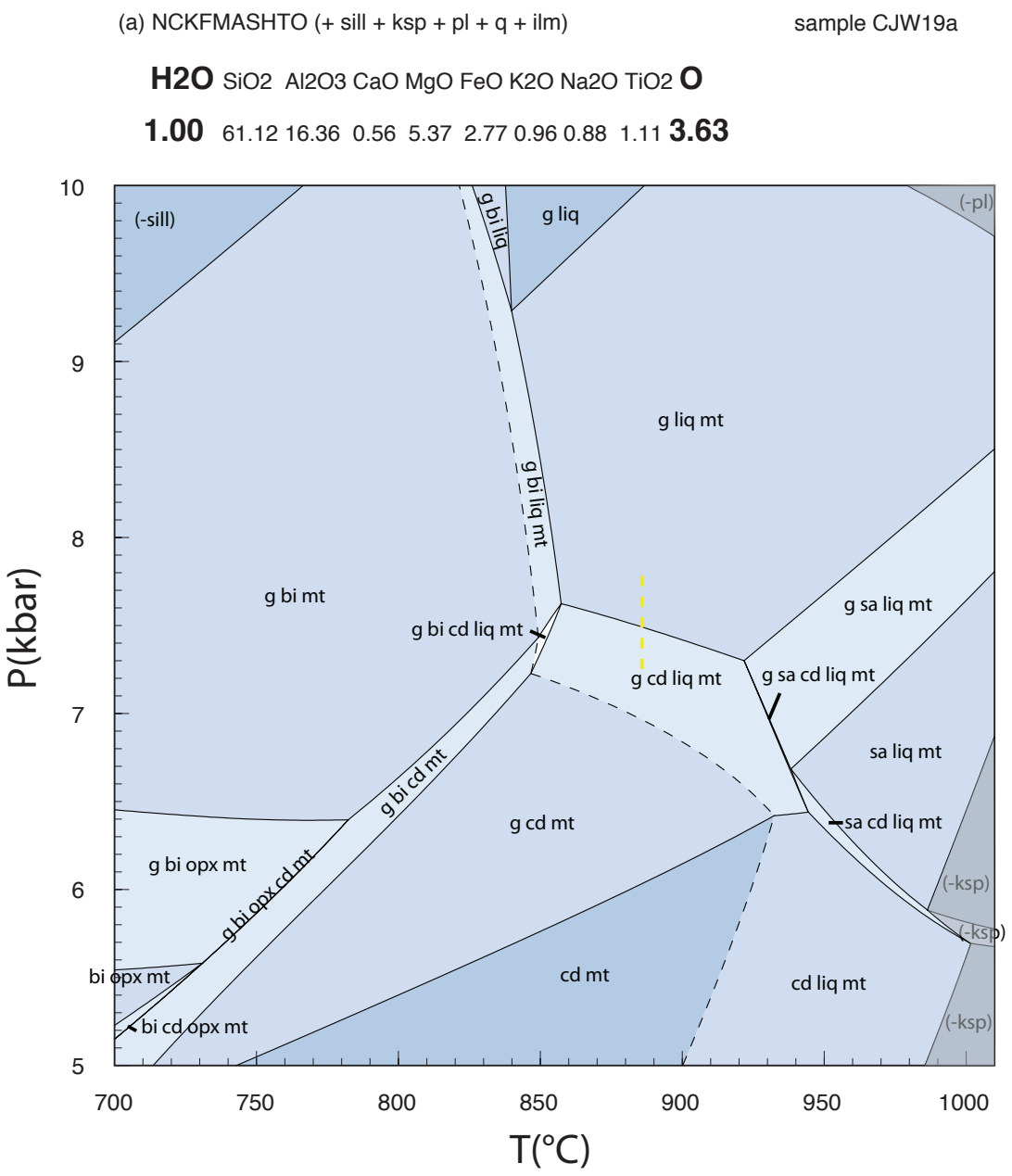

Figure 4.18. *P–T* pseudosection for sample CJW19a metapelite from the Ihosy Formation. The solidus is shown with a dotted line. Yellow dashed line shows a potential decompression *P–T* path, with peak g-liq-sill-mt and retrograde cordierite. Modelling undertaken in NCKFMASHTO with K-feldspar, plagioclase, quartz and ilmenite in-excess.

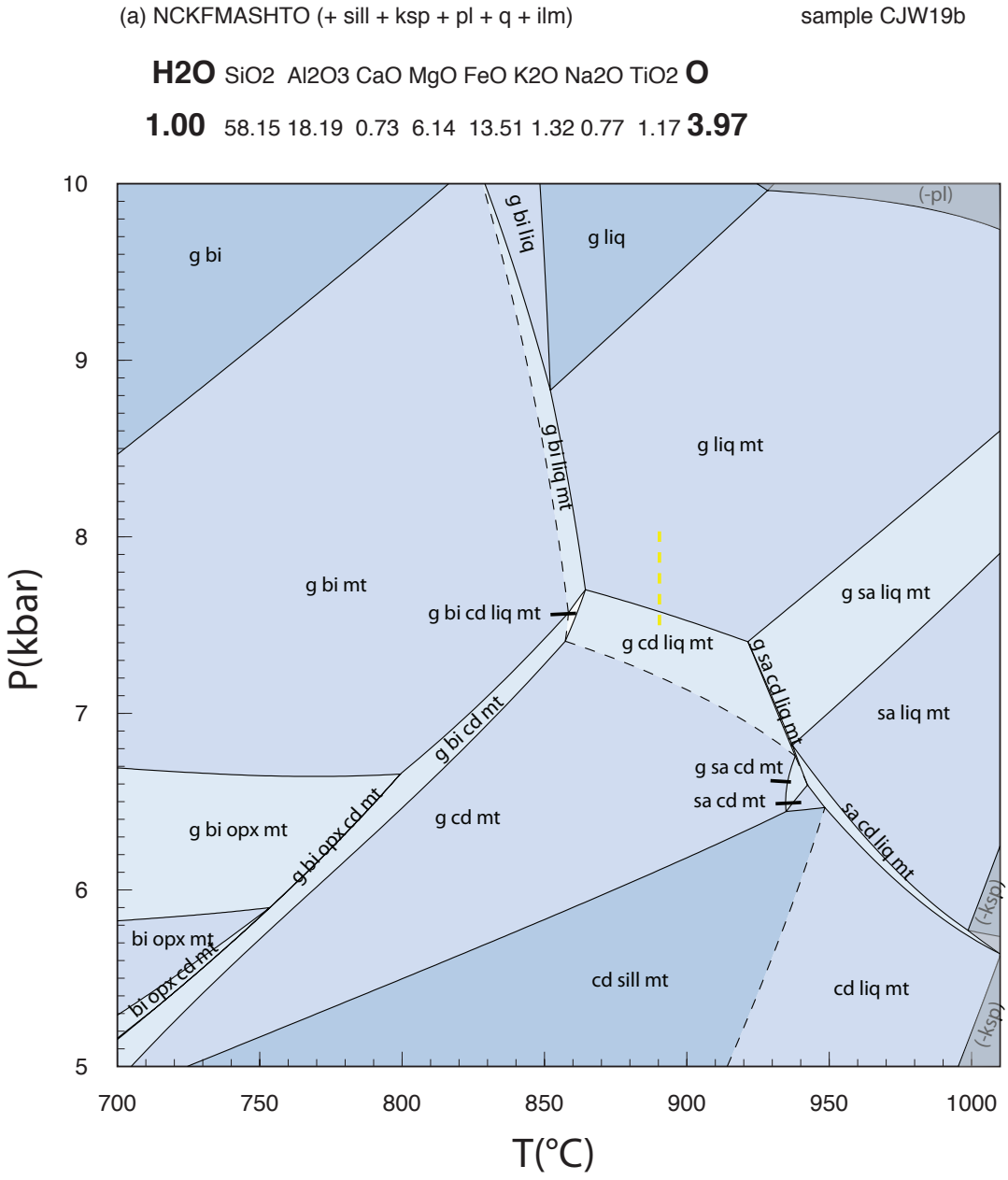

Figure 4.19. *P–T* pseudosection for sample CJW19b metapelite from the Ihosy Formation. The solidus is shown with a dotted line. Yellow dashed line shows a potential decompression *P–T* path, with peak g-liq-sill-mt and retrograde cordierite. Modelling undertaken in NCKFMASHTO with K-feldspar, plagioclase, quartz and ilmenite in-excess.

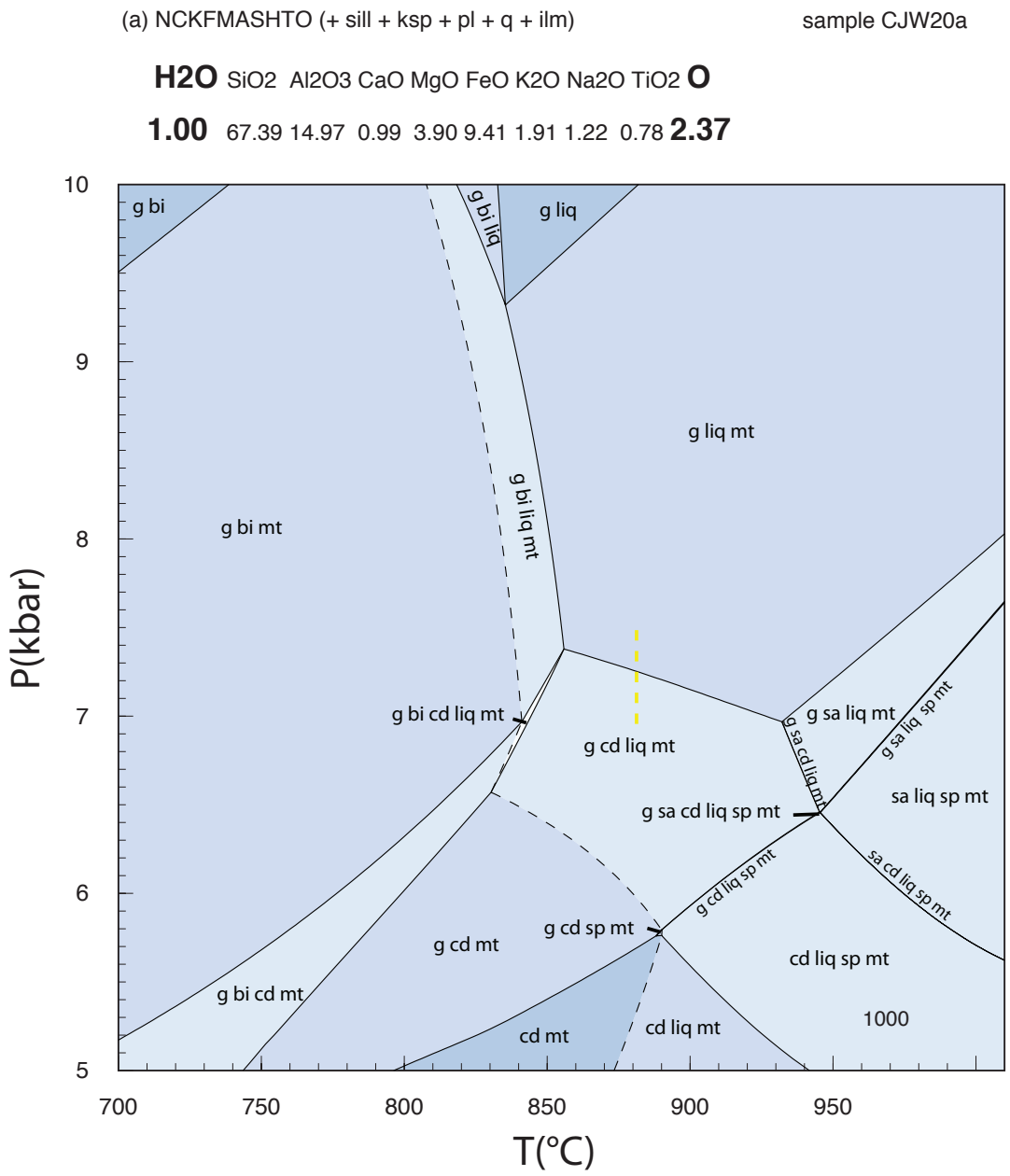

Figure 4.20. *P–T* pseudosection for sample CJW20a metapelite from the Ihosy Formation. The solidus is shown with a dotted line. Yellow dashed line shows a potential decompression *P–T* path, with peak g-liq-sill-mt and retrograde cordierite. Modelling undertaken in NCKFMASHTO with K-feldspar, plagioclase, quartz and ilmenite in-excess.

ilar topologies and the overlap of peak mineral assemblage fields provides a constraint on the lower boundary of stability.

From petrographic observation of the timing of mineral growth, a P–T path can be estimated. Due to the high temperatures experienced by these rocks, a prograde path is not preserved or easily established, although rare biotite grains could have grown in a g–bi–mt field prior to reaching peak. Peak conditions were reached within the g-liq-sill-mt field, with minimum P–T estimates of 855°C and at pressures above 7.4 kbar. The rock then undergoes decompression from the peak, as seen in the formation of cordierite, as rims or as optically continuous poikiloblasts with inclusions of garnet and sillimanite. The timing of growth of spinel is not obvious in these rocks. Spinel is not found during prograde or peak conditions on any of the pseudosections consistent with it being a retrograde mineral formed by exsolution from magnetite post peak.

All three samples show formation under a P–T path from peak to decompression. These results suggest that the samples experienced regional metamorphic conditions with a peak mineral assemblage of at least 850°C at pressures of above 7.4kbar. No upper limit on the pressure or temperature is given by the reactions seen by the samples. However, as the rock is inferred to reach peak at temperatures not much greater than the solidus (White & Powell, 2002), this most likely constrains peak pressure and temperature to below 8 kbar and 950°C.

4.6 Discussion and Conclusions

Figure 4.21 summarises the results of the methods used to find the peak P–T range for the formation of the metapelites in the Ihosy Formation, bringing together both the overlapping peak fields of the non-sapphirine-bearing samples and the lower P–T boundary in NCKFMASHTO for the sapphirine-bearing sample. The results of the samples combined indicate that the peak P–T conditions experienced in the south-east of the Anosyen tectonic domain attained at least 850°C and pressures greater than 7.6 kbar. While not providing a conclusive upper temperature for peak assemblages found in the granulites of the Ihosy Formation in southern Madagascar, the modelling shows that sapphirine–quartz-bearing assemblages can be stable at temperatures below 900°C in such an oxidised terrane.

Use of four samples over a restricted area is not enough to make a judgement on tectonic processes in the area, however the lower boundary estimate for PT conditions is lower than that described by Jöns and Schenk (2011) and is more in agreement with temperature estimates by Boger et al. (2012). The osumilite-bearing sample analysed by Horton et al. (2016) has an estimated peak temperature of between 910–950 °C, however this might be more similar to the results here if ferric iron were able to be considered in the osumilite-bearing assemblages. The low pressure boundary of 7.6 kbar in this study is constrained by the location of the opx+liq+sill = g+sa+cd univariant reaction enabling the formation of opx+sill microdomains in the sapphirine-bearing sample. This modelling does not disprove the possibility of pressures at 10 kbar (e.g. Horton et al., 2016) or temperatures in-excess of 1000°C (e.g. Jöns & Schenk, 2011), however it does show that these ultra-high temperatures and moderately high pressures are not required and, most likely, are not preferred.

Attempts at modelling the inhomogeneous sample CJW20b using the whole rock bulk analysis as an effective bulk composition are given in the Appendix to this chapter, and show categorically why this does not work. No P–T conditions were identified that could predict a low variance sapphirine- and orthopyroxene-bearing assemblage, even when water content and oxidation state were treated as variables. The P–T grid and compatibility diagram approach to modelling microdomains was successful, as the microdomains could be constrained to a P–T field by univariant

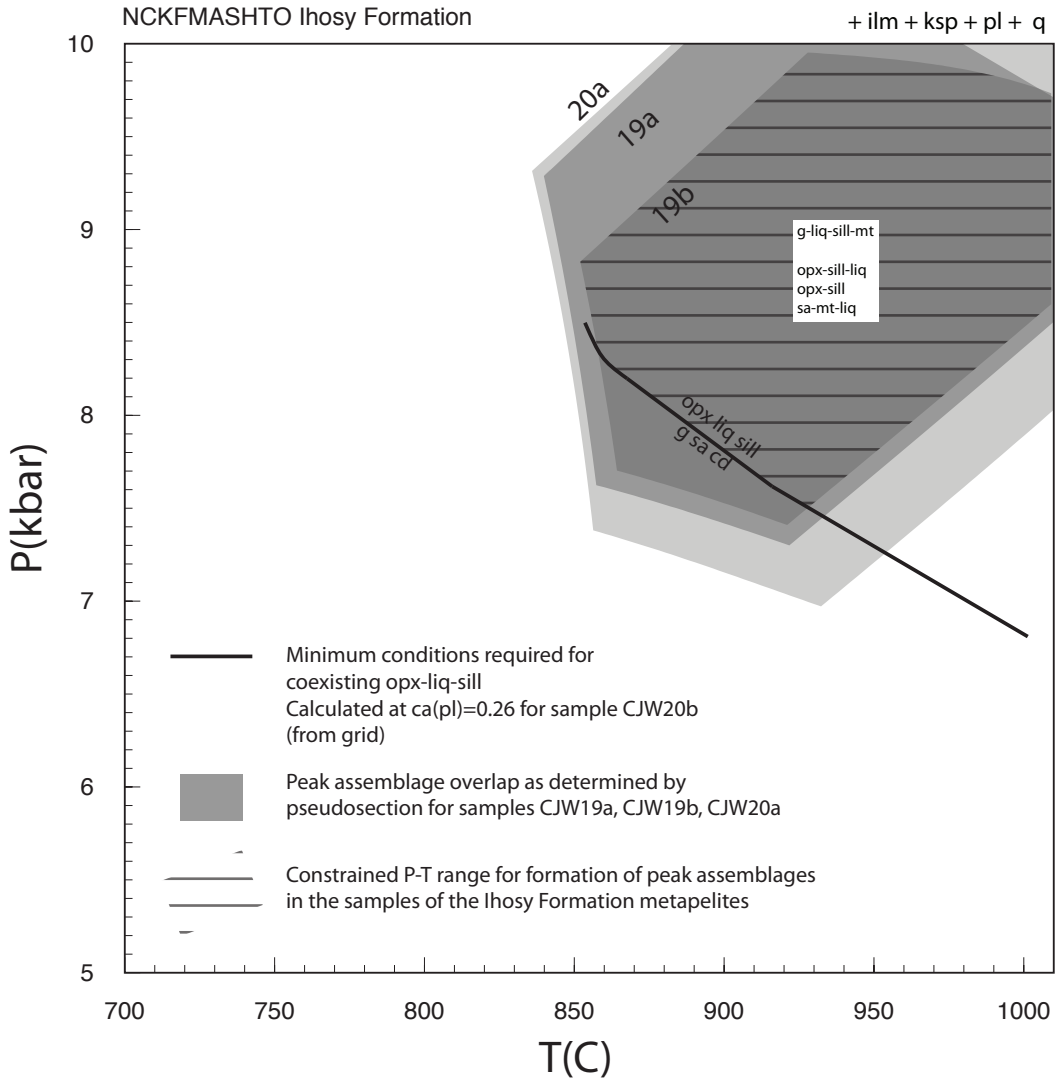

Figure 4.21. A summary of the P–T conditions required to form the peak assemblages as seen in the Ihosy Formation. Grey shaded regions cover the conditions of formation in NCKFMASHTO for samples CJW19a, CJW19b, and CWJ20a from the pseudosections presented in Figures 4.18 to 4.20. The black line shows the minimum conditions required for coexisting opx-liq-sill in sample CJW20b, and is the same line as in the right image in Figure 4.10 calculated at ca(pl) = 0.29 (anorthite content from Table 4.5)

reactions. Compatibility diagrams allow visualisation of all the microdomains in one diagram and can show the compositional relationship between them. Shown in series, the diagrams can be interpreted to show the conditions when assemblage became domainal, and as such record different parts of the retrograde P–T path.

4.7 Appendix

4.7.1 Attempts to model a domainal rock with a whole rock bulk composition

When attempts to model an observed peak mineral assemblage with the bulk composition as measured by XRF fail, there are questions to be answered as to why that is the case. Can a better estimate of ferric iron content or amount of water present make a difference? Is the bulk composition unusual in that it is inappropriate to simplify the system to NCKFMASHTO? The following details an example of when the traditional method of modelling a peak assemblage with pseudosections is abandoned.

Initial attempts at modelling the apparently low-variance overall sapphirine-bearing assemblage assumed non-domainal equilibration. Pseudosections are calculated to find the pressure and temperature for the formation of the interpreted peak assemblage of sapphirine–orthopyroxene–magnetite–melt (+ sillimanite + K-feldspar + plagioclase + + quartz + ilmenite).

XRF measured bulk with H_2O similar to previous interpretation, and O determined by titration

Figure 4.22 shows a P–T pseudosection in NCKFMASHTO, calculated with the measured bulk composition for sample CJW20b (Table 4.9) between 4-8 kbar and 700-1000°C, with the O value of 1.16 mol% determined by titration, and an H_2O value of 2.18 mol% (chosen as below LOI and similar to that chosen by Boger et al. (2012) for Ihosy Formation metapelites). A sa–opx–liq–sill field is identified, however magnetite has not developed under these conditions. As the stability of oxides in P–T space is largely affected by oxidation state, the bulk composition can be varied with changing O at a fixed pressure across a temperature range. Water content of the rocks at peak was also varied, however this is only thought to change the location of the solidus and would not affect the stability of anhydrous minerals at peak.

Varying O for the XRF measured bulk with H_2O similar to previous interpretation

A T–M_O diagram (Figure 4.23), using the measured bulk composition of CJW20b and at a fixed pressure of 6 kbar is calculated, showing that magnetite is only stable within this bulk composition at conditions of higher oxidation state ($>M_O$ of 0.7) and lower temperatures (less than 750 °C) than the sapphirine-bearing assemblage which occurs only above 900 °C.

Varying H_2O for the XRF measured bulk with O determined by titration

Varying H_2O content (T–M_{H_2O}) in Figure 4.24 also has no effect on the sapphirine-bearing assemblage, with the only significant feature being the raising of the solidus at lower M_{H_2O}. This is significant however, as the preserved peak assemblage would form at temperatures that are far higher than the solidus once crossed. A solidus closer to sapphirine-bearing assemblages, and further from biotite-bearing assemblages is favoured, occurring at a low H_2O content of 0.02 mol%.

Varying O for the XRF measured bulk with low water content

Lowering H_2O content and calculating a T–M_O diagram investigates what effect changing O has on rock with low water content (Figure 4.25). Sapphirine and magnetite only coexist at M_O values greater than around 0.4. Spinel is lost in this rock above an M_O of 0.7. Choosing an O value within this range allows the sample to be oxidised enough to stabilise sapphirine and magnetite,

but low enough to enable spinel to form. For Figure 4.26 onwards, the O value is increased to 1.625 mol%.

XRF measured bulk with low H_2O, and O higher than the titration value

Using the increased value for O, combined with a lower H_2O value does not result in coexisting sapphirine and orthopyroxene, as seen in the P–T pseudosection in Figure 4.26. Orthopyroxene is restricted to assemblages at temperatures lower than 800°C, and therefore does not form in equilibrium with sapphirine, which arrives in the system at approximately 900°C. A T–M_{H_2O} using the increased O value (Figure 4.27) shows that increasing water content in the bulk composition does not extend the stability of orthopyroxene into a sapphirine-bearing field. Even then, the assemblage would not include melt.

Varying H_2O for the XRF measured bulk with high oxidation state

Figures 4.23 to 4.27 show the attempts at varying the oxidation state and water content of the bulk composition to accurately model the observed peak mineral assemblages in sample CJW20b. These modifications did not model an assemblage including sapphirine, sillimanite, orthopyroxene, magnetite, garnet, quartz, plagioclase, K-feldspar, ilmenite and melt. Having accounted for variations in bulk composition, the assumptions made in quantitative modelling can be investigated. There may be extra components in minerals not accounted for in the models – such as the influence zinc has in spinel. Spinel is interpreted to be a retrograde mineral, so the significance of this is small. Simplifying the system from NCFKAMSHTO to KFMASHTO can allow modelling by discounting the influence of sodium and calcium, therefore removing plagioclase from the calculations.

XRF measured bulk with low H_2O, and O higher than the titration value in a reduced system

A P–T pseudosection in KFMASHTO with an increased O at 1.625 mol% and a reduced water content at 0.02 mol% is calculated in Figure 4.28. Sapphirine and orthopyroxene can coexist on a univariant between 880–900°C at between 5–6 kbar, however the assemblage is melt absent.

Varying H_2O for the XRF measured bulk with high oxidation state

Increasing water content using the T–M_O in Figure 4.29 only destabilises sapphirine and orthopyroxene. Having varied oxidation state, water content and moving to a more simplified system, other assumptions outside the bulk composition are considered. On close inspection of the petrography the ferromagnesian minerals appear inhomogeneous in distribution and quite possibly have formed in microdomains, and therefore not in equilibrium with each other. As a bulk composition for each microdomain is needed for pseudosection modelling, and such compositions are not available, the decision is made to investigate mineral evolution through quantitative compatibility diagrams.

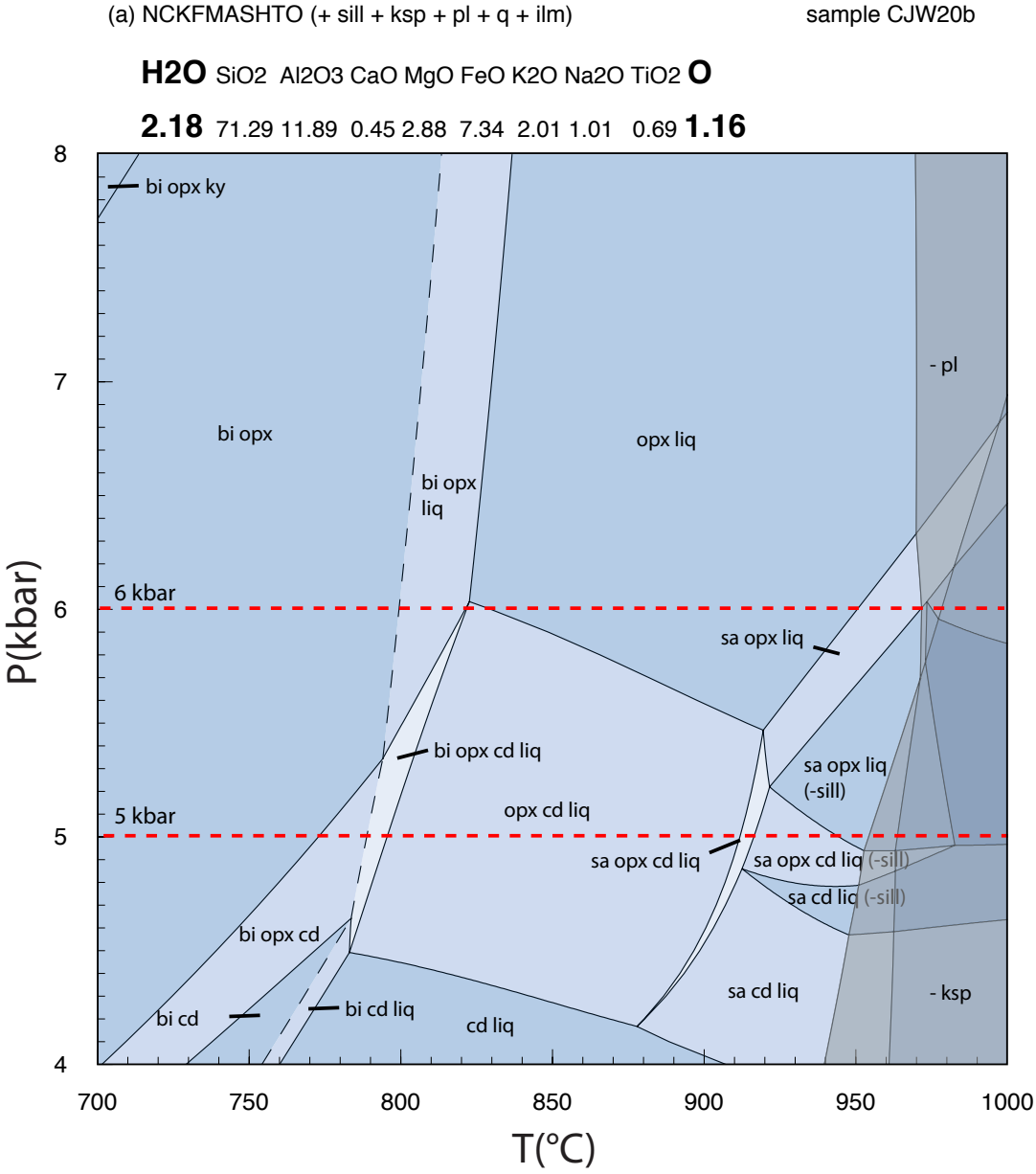

Figure 4.22. *P–T* pseudosection for sample CJW20b metapelite from the Ihosy Formation. O value determined by titration and H_2O value chosen as below LOI and similar to that chosen by Boger, White and Schulte (2012). Magnetite does not coexist with sapphirine and orthopyroxene within the modelled conditions. The solidus is shown with a dotted line. Modelling undertaken in NCKFMASHTO with sillimanite, K-feldspar, plagioclase, quartz and ilmenite in-excess. Red dashed lines indicate position of varying O at 6 kbar (Figure 4.23) and for varying H_2O at 5 kbar (Figure 4.24).

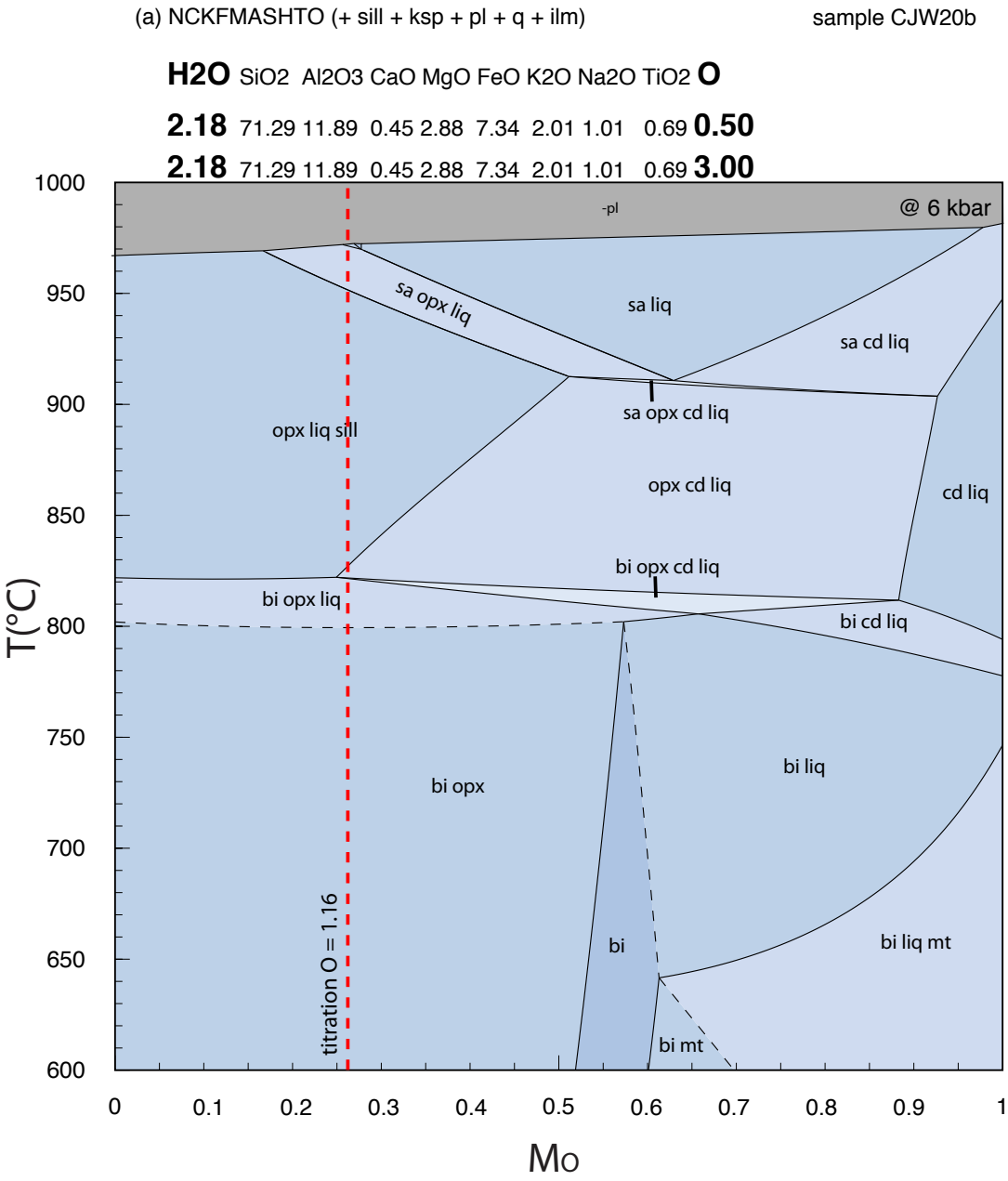

Figure 4.23. T–M_{O} pseudosection for sample CJW20b metapelite from the Ihosy Formation at 6 kbar. O value is varied on the X axis from 0.50 mol% to 3.00 mol%, and H_2O value chosen as below LOI and similar to that chosen by Boger, White and Schulte (2012). At these conditions, magnetite is stable in the rock at higher oxidation states than modelled in Figure 4.22, however still does not coexist with sapphirine and orthopyroxene. The solidus is shown with a dotted line. Modelling undertaken in NCKFMASHTO with sillimanite, K-feldspar, plagioclase, quartz and ilmenite in-excess. Red dashed line shows the M_{O} corresponding to Figure 4.22 which was the titration value.

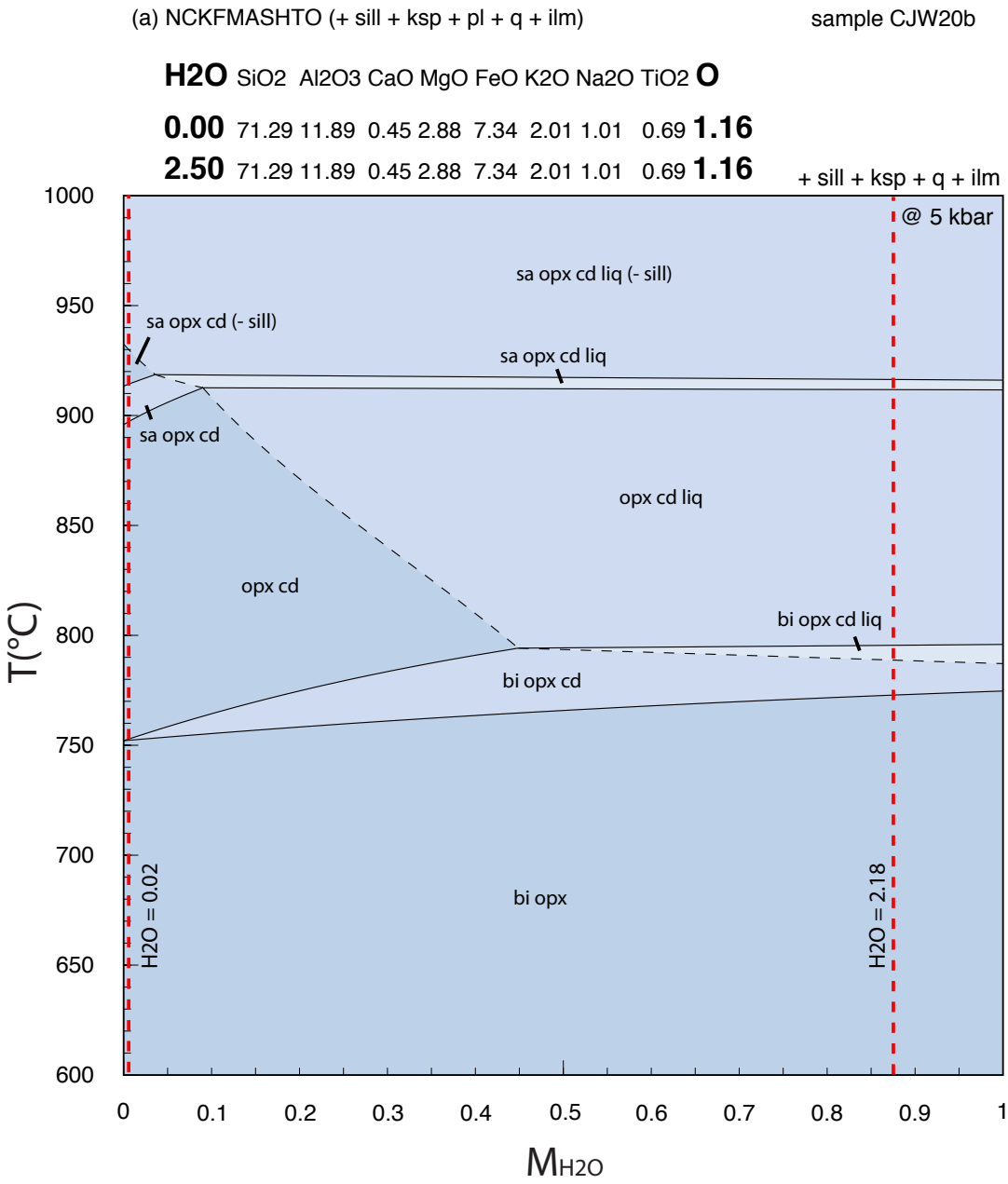

Figure 4.24. T–M_{H_2O} pseudosection for sample CJW20b metapelite from the Ihosy Formation at 5kbar. O value is fixed at the titration value, and H_2O value varies from 0.00 mol% to 2.50 mol%. Decreasing water content from what was used in Figure 4.22 (red line) results in the raising of the solidus. This results in the assemblages containing sapphirine being preserved as the solidus is closer to conditions at which the mineral is stable. A lower solidus can allow biotite to be preserved at peak. This is not observed in this sample. The solidus is shown with a dotted line. Modelling undertaken in NCKFMASHTO with sillimanite, K-feldspar, plagioclase, quartz and ilmenite in-excess. Red dashed lines indicate the position of H_2O value chosen as below LOI and similar to that chosen by Boger, White and Schulte (2012); and a lower H_2O content, which is modelled in PT in Figure 4.25 (to investigate varying oxidation state at low water content) and Figure 4.26 (to investigate a low water content, higher oxidation state bulk composition)

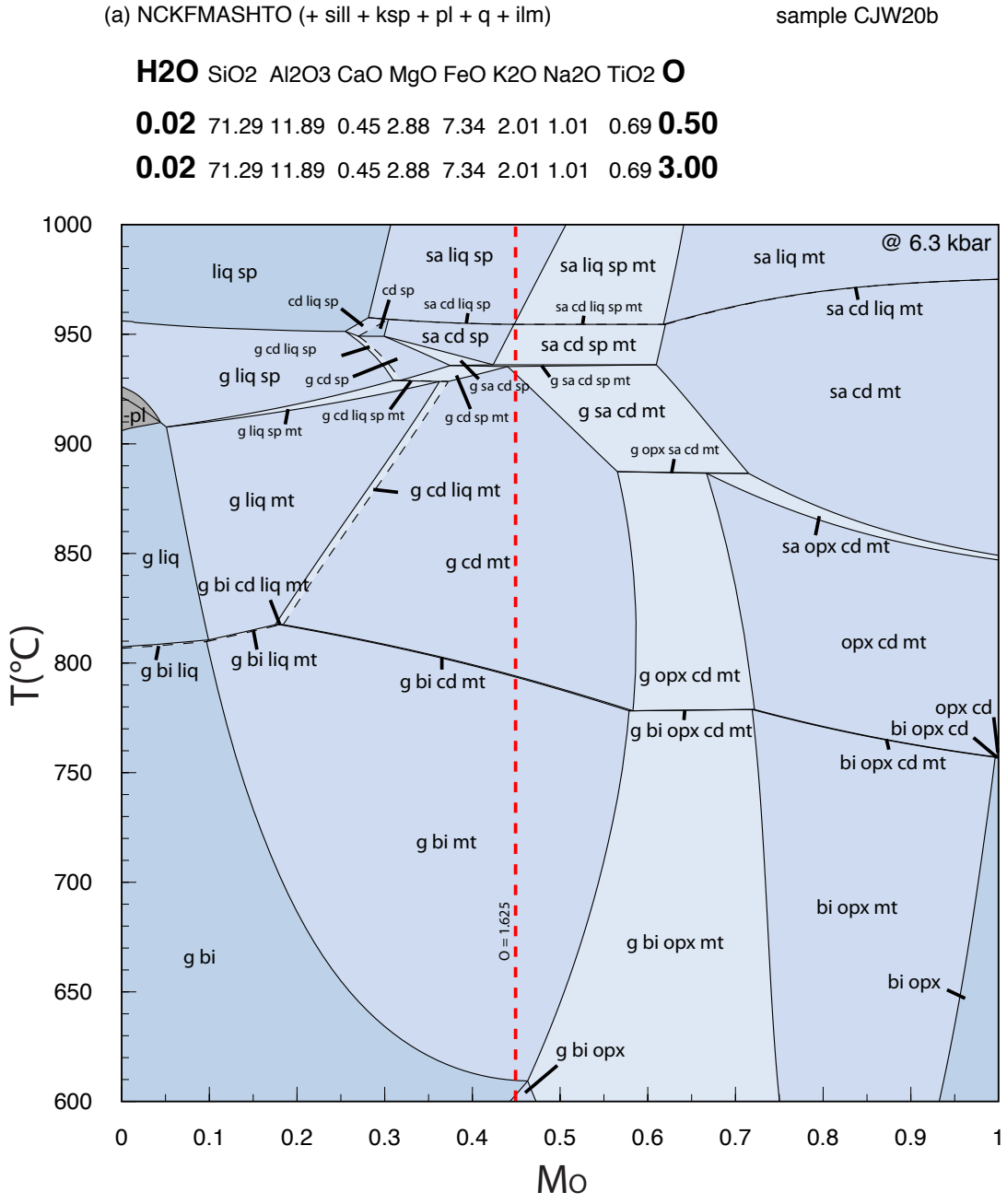

Figure 4.25. T–M_{O} pseudosection for sample CJW20b metapelite from the Ihosy Formation at 6.3kbar. O value is varied on the X axis from 0.50 mol% to 3.00 mol%, with a lowered H_2O value chosen from Figure 4.24 to raise the solidus. Sapphirine coexists with both magnetite and spinel at M_{O} greater than 0.45. For the sample to be oxidised enough to grow sapphirine and magnetite at peak, this means that O should be greater than 1.625 mol%. The solidus is shown with a dotted line. Modelling undertaken in NCKFMASHTO with sillimanite, K-feldspar, plagioclase, quartz and ilmenite in-excess. Red dashed line indicates the higher M_{O} used for Figure 4.26 onwards.

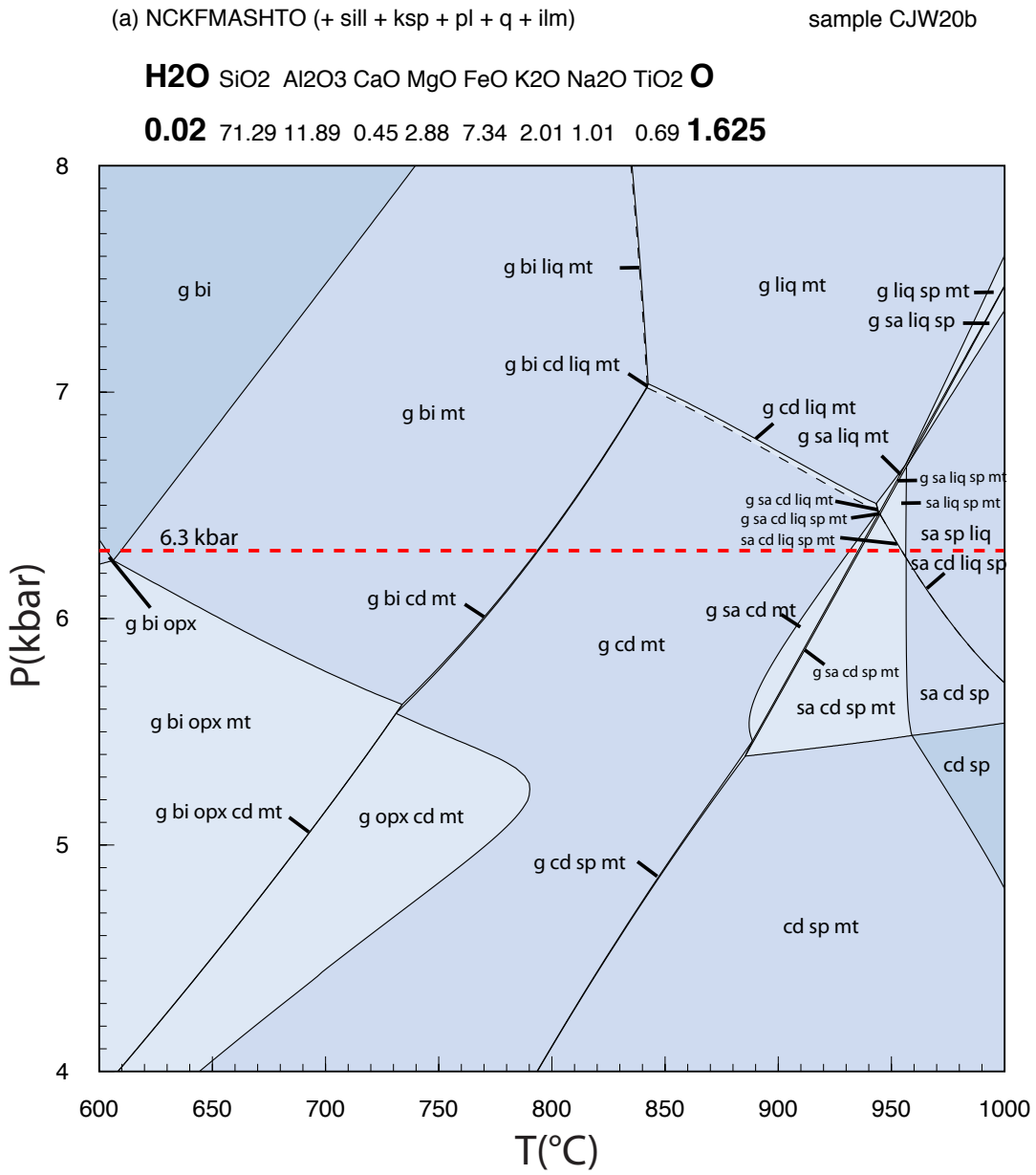

Figure 4.26. *P–T* pseudosection for sample CJW20b metapelite from the Ihosy Formation. O value determined for coexisting sapphirine and magnetite (from Figure 4.25) and H_2O value chosen to raise the solidus (from Figure 4.24). Sapphirine does not coexist with orthopyroxene. The solidus is shown with a dotted line. Modelling undertaken in NCKFMASHTO with sillimanite, K-feldspar, plagioclase, quartz and ilmenite in-excess.

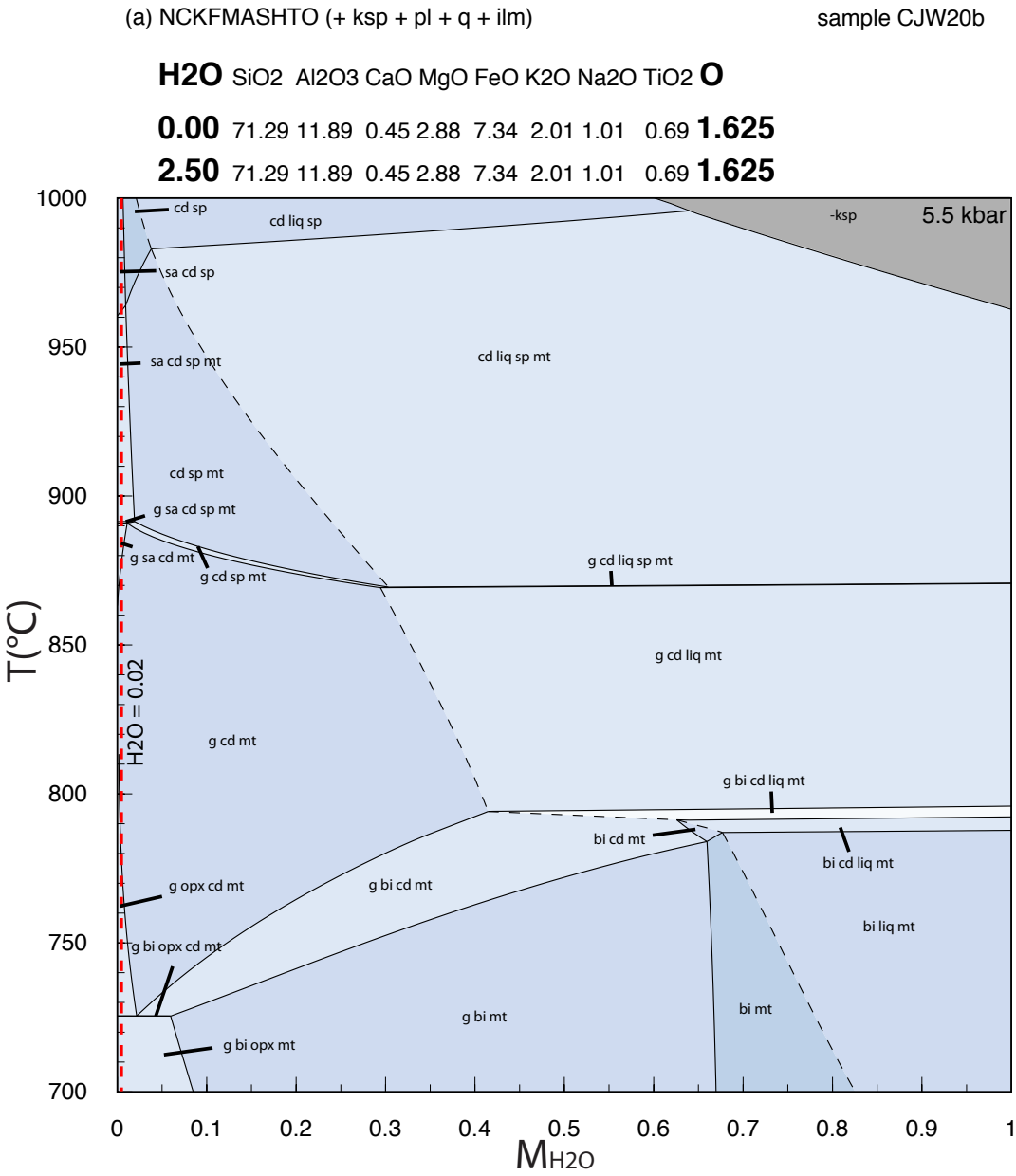

Figure 4.27. T–$M_{\mathrm{H_2O}}$ pseudosection for sample CJW20b metapelite from the Ihosy Formation. O value determined for coexisting sapphirine and magnetite (from Figure 4.25) and H_2O value varies from 0.00 mol% to 2.50 mol%. With increasing water content, sapphirine still does not coexist with orthopyroxene. The solidus is shown with a dotted line. Modelling undertaken in NCKFMASHTO with sillimanite, K-feldspar, plagioclase, quartz and ilmenite in-excess.

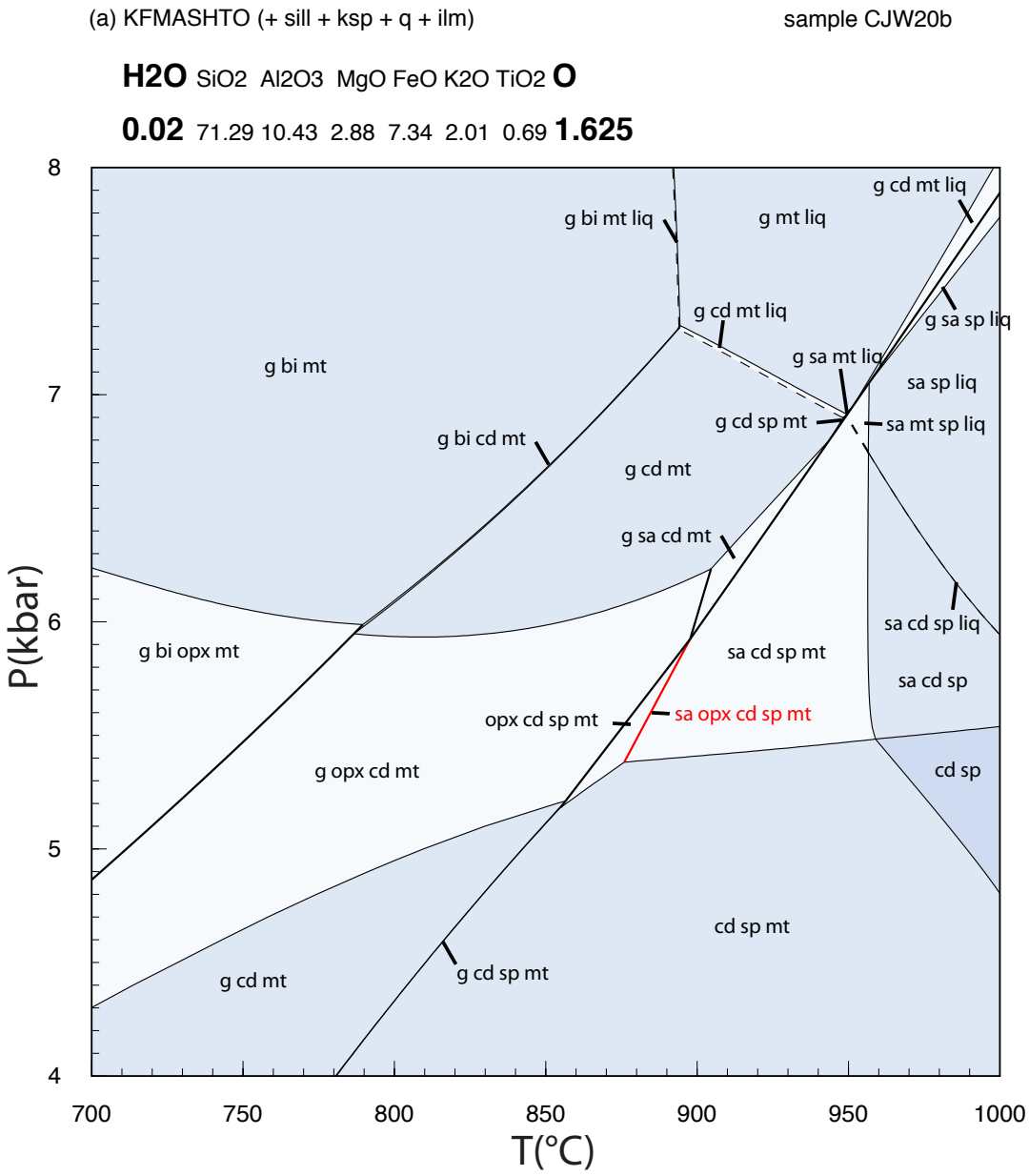

Figure 4.28. *P–T* pseudosection for sample CJW20b metapelite from the Ihosy Formation. O value determined for coexisting sapphirine and magnetite (from Figure 4.25) and H_2O value chosen to raise the solidus (from Figure 4.24). The univariant sa-opx-cd-sp-mt (in red) is the closest here at modelling the observed peak assemblage, however it is without melt. Modelling undertaken in KFMASHTO with sillimanite, K-feldspar, quartz and ilmenite in-excess.

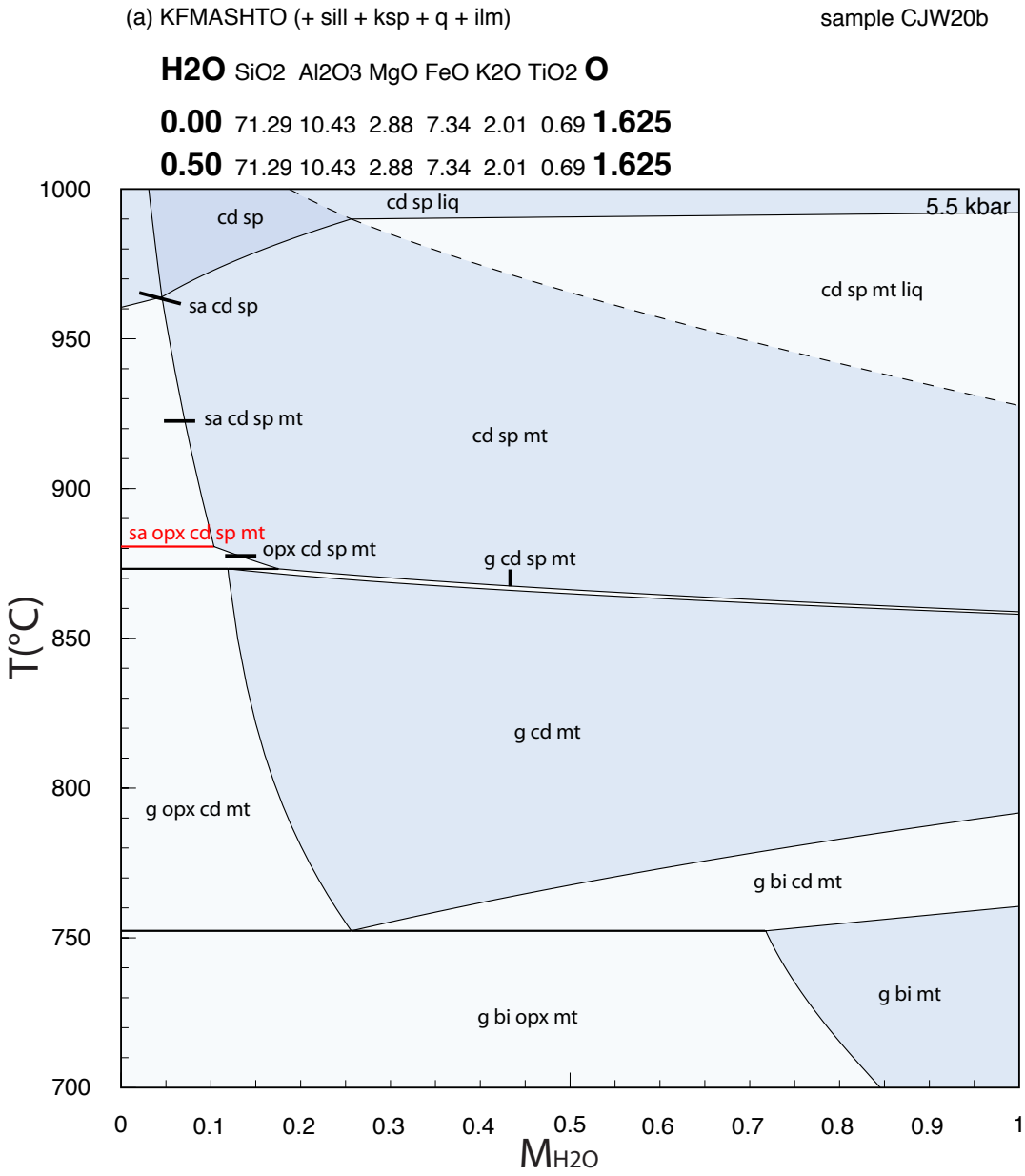

Figure 4.29. T–$M_{\mathrm{H_2O}}$ pseudosection for sample CJW20b metapelite from the Ihosy Formation. O value determined for coexisting sapphirine and magnetite (from Figure 4.25) and H_2O value varies from 0.00 mol% to 0.5 mol%. Even a small increase in H_2O results in the loss of orthopyroxene and sapphirine in the assemblage. Modelling undertaken in KFMASHTO with sillimanite, K-feldspar, quartz and ilmenite in-excess.

Chapter 5

An alternative control on the development of mineral assemblages

5.1 Introduction

Reactions involving fluid generation occur as initially-hydrous mineral assemblages in metamorphic rocks develop with increasing temperature in the prograde history. For example, metapelites have an initially high H_2O content, and are considered to be water-saturated from early in metamorphism. Prograde heating in subsolidus conditions results in H_2O generation by ongoing dehydration reactions, and mineral assemblages become progressively less hydrous. Free water is lost from the source rock due to compaction (e.g. Webb, Powell & Mclaren, 2015; Yardley, 2009), with any remaining H_2O retained in the structure of hydrous minerals. A small amount of retained free H_2O makes a small amount of new hydrous mineral at the start of the retrograde history, with much of the peak metamorphic mineral assemblage preserved (Guiraud et al., 2001). Significant retrogression is associated with advent of fluid, commonly with associated deformation.

Upon reaching temperatures higher than the solidus, melt production proceeds via the breakdown of hydrous minerals, for example muscovite and biotite in metapelites (White, Powell & Clarke, 2002). The H_2O that was structurally bound is then progressively partitioned into the melt (Webb et al., 2015). The preservation of high-grade, mostly less hydrous mineral assemblages from higher temperatures (the 'peak metamorphic assemblage') requires the loss of water bound in the melt, otherwise pervasive retrograde textures would be developed on crystallisation of the melt (White et al., 2002). In the absence of pervasive retrogression, melt must be lost to preserve the peak assemblage. Any remaining melt is crystallised with the growth of more hydrous minerals in the retrograde history (White et al., 2002). This commonly small amount of remaining melt will produce retrogression to a small amount of hydrous assemblages typical of the amphibolite facies (e.g. White & Powell, 2002; White et al., 2001). As in subsolidus rocks, significant retrogression is associated with advent of melt or hydrous fluid, also commonly with associated deformation. This may also form part of the story for rocks that have experienced more than one metamorphic event.

In general, the amount of retrogression of an assemblage is explained in terms of the amount of fluid added, given that retrogression involves the growth of new, more hydrous minerals. On top of this, the conventional way of explaining the degree of retrograde re-equilibration, in the absence of fluid addition, is that diffusion and reaction rates tend to become much slower with

cooling. As a consequence, this kinetic control means that the mineral assemblage can effectively 'freeze' in place. But there is plausibly an additional factor in the cessation of retrograde reaction, which could instead be explained by the rocks becoming sufficiently strong that they react under constant volume conditions, rather than under superimposed pressure. In order to investigate the consequences of a constant volume process, calculated volume–temperature (V–T) phase diagrams are presented, rather than the normal pressure–temperature (P–T) phase diagrams. The resulting paths are then compared under different assumptions of kinetic and mechanical closure. This will be done using mineral equilibrium calculations in THERMOCALC on a granulite sample that has been reworked in subsolidus fluid-absent conditions.

5.2 Previous work

5.2.1 Metamorphic history

This study investigates the process of reworking on the poly-metamorphic evolution of orthopyroxene-rich quartz-saturated granulites of the Strangways Metamorphic Complex (SMC), Arunta Block, central Australia. These rocks have been interpreted to record evidence of two tectonically distinct metamorphic events, the first in the granulite facies, M_1 at *c.* 1.7 Ga, and the second at upper amphibolite facies, M_2, at *c.* 1.65 Ga. The M_1 event involved partial melting and migmatisation, with the preserved mineral assemblages indicating that melt was lost from the rocks at or near peak metamorphic conditions (White & Powell, 2002). Peak M_1 metamorphic conditions have been interpreted at 8.5 kbar and 850°(Diener et al., 2008; Goscombe, 1992b), coinciding with the development of D_1 gneissic fabrics and layer-parallel migmatisation (Clarke, White, Lui, Fitzherbert & Pearson, 2007; Goscombe, 1992a). The second event is associated with transpressional SW-directed transport resulting in D_2 mylonitic fabrics and wide-spread sheath folds (Goscombe, 1991) in the more deformed rocks. The focus of this study is mineral assemblage development in M_2.

Early interpretations of the evolution of the terrane invoke reactivation and deformation during cooling subsequent to M_1. In this case, granulite metamorphism peaking at 850–920°C, 7–9 kbar was followed by isobaric cooling which included an episode of partial hydration. Therefore, the inferred M_2 paragenesis occurred as a consequence of rehydration in a traditional retrograde re-equilibration sense, immediately after M_1 (Warren, 1983). In this scenario, the rocks were rehydrated by fluids released from the crystallisation of partial melts, without requiring subsequent prograde P–T evolution.

Later work by Goscombe (1992a, 1992b) argue that M_1 granulites were reworked in a second tectonic event involving shearing and shortening of the terrane with partial melting. M_1 evolved during an 'anticlockwise' P–T path peak (8–9 kbar and 850–950°C) prior to isobaric cooling to a stable crustal geotherm. Subsequent reworking in M_2 took place in a regime of compressional orogenesis with a 'clockwise' P–T path prior to decompression with cooling. Norman and Clarke (1990) also suggest two metamorphic events, however with M_2 occurring at higher pressure and temperature than the earlier event. Ballèvre, Hensen and Reynard (1997) also propose a two stage history, however like Warren (1983), they group together M_1 and M_2 in a singular tectonic event, with the addition of rehydration during exhumation (M_3) as a method to recrystallise symplectic reaction textures.

More recent work by Diener et al. (2008) present calculated phase diagrams to investigate the P–T path and metamorphic environment of the granulites. Calculated pseudosections show that the growth of M2 mineral assemblages does not require an open system with respect to H_2O.

Pseudosections calculated in the Diener et al. (2008) study place M_2 at subsolidus fluid-absent conditions at 6-7.5 kbar and 670-720 °C. This is similar to pseudosection modelling by Clark, Hand, Kelsey and Goscombe (2007) who placed M_2 peak conditions at 6–8kbar and 700°C. These rocks were not rehydrated after melt loss that occurred during M_1. For M_2 growth, Diener et al. (2008) suggest that re-crystallisation occurred as a response to deformation and the elevated temperature. The interpretation is that M_2 is driven by increased temperature after initial M_1 cooling. Re-crystallisation and re-equilibration induced by deformation resulted in reworking of the mineral assemblage. The terrane then cooled from M_2 along the stable geotherm without exhumation. The terrane was then exhumed during the Alice Springs Orogeny at 400–300 Ma (Ballèvre, Möller & Hensen, 2000; Biermeister et al., 2003).

There is a question of whether M_1 and M_2 are separate high-grade events. Möller, Hensen, Armstron, Mezger and Ballevre (2003) conducted a study using the U-Pb SHRIMP ion microprobe method on zircon, combined with multi-grain TIMS U-Pb dating on monazite to determine the age of the Late Strangways Orogeny (M_1). The results showed M_1 and associated deformation D_1, occurred between 1.715–1.735 Ga in the Edwards Creek area, in the east of the SMC. Clark et al. (2007) used pressure–temperature data and *in situ* monazite geochronology to constrain M_2 to 1.65Ga, coincident with terrane accretion during the Liebig Orogeny. The possibility that the M_2 mineral assemblage textures evolved during retrograde evolution of M_1 (Warren, 1983) in a singular event is open as the estimated timing constraints of the two events [M_1 at 1.715–1.735 (Möller et al., 2003) and M_2 at 1.65 $\pm$0.044 Ga (Clark et al., 2007) may be close. Taking the standard deviation on the ages as 0.02 and 0.022 respectively, the $\pm$ on the age difference is 0.06, more or less encompassing the difference between the age estimates. This study looks at an alternative control on developing the M_2 textures which does not require inducement by further deformation.

5.2.2 Petrography

As observed in Diener et al. (2008) the orthopyroxene-rich granulites in the field have a massive, coarse-grained texture. These granulites occur as 10- to 100m pods and lenses within quartz-rich gneisses. The quartz-rich gneisses have a strong fabric and were less competent than the granulites. Diener et al. (2008) suggest that this leads to any deformation that occurred during reworking was focused in the quartz-rich gneisses and not in the granulites, which show little evidence of deformation. The quartz-rich gneisses only preserve isolated porphyroblasts of the M_1 assemblage in a matrix of M_2 assemblage, while the M_1 assemblage is preserved in the granulites with only partial replacement in the M_2 overprint. This overprint is characterised by symplectites, corona, and exsolution reaction textures. The granulites contain centimetre-scale quartzofeldspathic leucosomes, reflecting partial melting during its metamorphic history.

Two samples of the orthopyroxene-rich granulite are discussed by Diener et al. (2008), one of which (S009) is utilised for modelling here. Sample S009 has an inferred M_1 mineral assemblage consisting of orthopyroxene, cordierite, sillimanite, biotite, plagioclase, quartz and rutile. Garnet and K-feldspar are absent in this sample. The M_2 mineral assemblage is developed as fine-grained reaction textures that overgrow and separate the M_1 phases and consists of orthopyroxene, gedrite, prismatic sillimanite, biotite and quartz. Diener estimates that sample S009 consists of 35% orthopyroxene, 20% cordierite, 15% biotite, 12% quartz, 10% sillimanite, and 5% plagioclase based on thin-section area.

Orthopyroxene dominates the M_1 assemblage and contains inclusions of cordierite, sillimanite, biotite, and quartz as well as fine-grained sillimanite and exsolved hematite. Orthopyroxene also

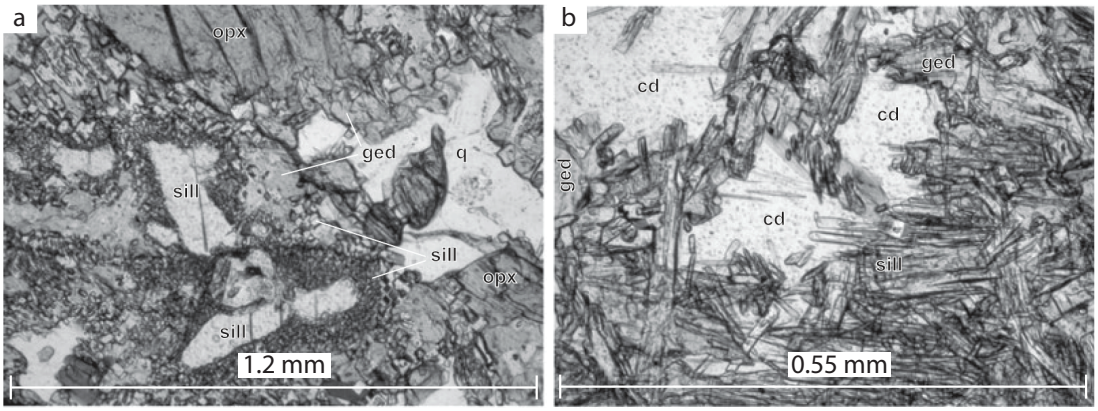

Figure 5.1. Photomicrographs of reaction textures. (a) Symplectites of M_2 gedrite and sillimanite overgrowing M_1 orthopyroxene and sillimanite. Width of view is 1.2mm. (b) Cordierite partly replaced by M_2 sillimanite and gedrite. Width of view is 0.55mm. From Diener, White and Powell (2008)

appears in the M_2 assemblage as fine-grained symplectic intergrowths with sillimanite. Cordierite appears as an M_1 mineral associated with orthopyroxene and sillimanite, and also appears in the matrix with quartz. It is commonly found partially replaced by M_2 gedrite and sillimanite in from its grain boundaries. This texture is defined by fine-grained gedrite containing needles of sillimanite. Biotite is found as inclusions within M_1 orthopyroxene and as single grains within the matrix. Some fine-grained biotite is associated with M_2 phases, suggesting that biotite was stable throughout the metamorphic history. Gedrite is only found in the M_2 assemblage, occurring as fine-grained aggregates in reaction textures that occur as rims around orthopyroxene and preferentially replacing M_1 cordierite porphyroblasts. Commonly only partial replacement has occurred, as in Figure 5.1b).

The bulk composition of sample S009 contains sufficient H_2O in the bulk to completely replace the M_1 assemblages with M_2 assemblages, primarily through the H_2O held in cordierite (see below). However, the M_2 overprint in the granulites is exhibited in reaction textures and symplectites that only *partially* replace M_1 phases, in what are interpreted as low-strain pockets. Symplectites themselves can be seen as a replacement mechanism under limited diffusion in the absence of deformation (White & Powell, 2011). Diener et al. (2008) discusses the limiting constraints on the development of M_2 assemblages and raises the possibility that the ability for the environment of the reaction volume to deform is a controlling factor that limits the development of new textures, the idea of which is addressed in this chapter.

5.2.3 Mechanism of reaction

The granulite samples from the Strangways Range are characterised by 'retrograde' assemblages which appear to be more hydrous than the original M_1 minerals that they partially replace. In earlier work, this lead to the presumption that the rocks were rehydrated during reworking (assemblage crosses contours of increasing H_2O content Guiraud et al., 2001). However, Diener et al. (2008) use calculated pseudosections to explain the observed reworked assemblages to see whether melt can be lost sufficiently during high-grade metamorphism to preserve peak M1 metamorphic assemblage while retaining enough H_2O in the minerals to elucidate reworking without rehydration. Diener et al. (2008) concludes that the latter is the case and that reworking at M_2 could have occurred in a closed system with respect to H_2O. Deformation during M_2 provided the impetus to restart equilibration and the growth of new mineral assemblages. In addition deformation is

implicated in allowing the volume change from the metamorphic reactions to occur. Following this logic, there should be a correlation between the intensity of deformation and the proportional development of M_2 mineral assemblages in the granulites. This can explain the limited replacement of M_1 assemblages in the granulites which show little evidence of reaction (such as sample S009) compared to the almost complete replacement of M_1 assemblages in the most deformed granulites and the surrounding strongly deformed quartz-rich gneisses.

Melt loss during prograde metamorphism is responsible for the preservation of high-grade mineral assemblages as it acts to elevate the solidus and therefore causes the residuum to become increasingly refractory (e.g. Fyfe, Price & Thompson, 1978; Powell, 1983; White & Powell, 2002). Therefore, subsequent reworking of this residuum composition in subsolidus conditions is unlikely without further fluid gain or deformation. This is due to slower intracrystalline and intergranular diffusion rates at lower temperatures. Other factors may also be involved, such as such as suggested by Milke, Abart, Kunze, Kock-Muller and Schmid (2009), Schmid, Abart, Podladchikov and Milke (2009) and Diener et al. (2008), who raise the possibility that 'it might in fact be the ability of the environment of the reaction volume to deform, rather than diffusion, that is the controlling factor that limits the development of [M_2 mineral assemblages]'. M_2 reworking could be thought to be the result of reactions at constant volume whereby the host becomes sufficiently strong to behave elastically and so reactions occur along an isochor. This is in contrast to a view that M_2 reworking required heating and/or deformation followed by retrograde cooling at superimposed pressure.

Mechanical closure

Metamorphic reactions and phase changes involve a volume change of the rock. This requires mechanical deformation of the surrounding matrix from where the reaction takes place. The stress induced by a reaction can act against the reaction that generates it (Hacker & Peacock, 1995; Mosenfelder & Bohlen, 1997; Paterson, 1995). If this induced deformation cannot take place because the rock is sufficiently strong, then the reaction does not run to completion. Following analysis of rim growth experiments (Milke et al., 2009), Schmid et al. (2009) have developed a coupled reaction–deformation model where 'the chemical mass transport associated with the rim growth reaction is combined with the viscous creep response of the matrix material'. The experiments showed the formation of different widths of reaction rims under two different matrix rheologies. The difference is attributed to the change in volume required in the rim-forming reaction being too large to be accommodated by the elastic response of the matrix. The rate law for reaction rim growth shows that 'the progress rate is proportional to the reaction overstepping and controlled by the slower of the two competing processes; either diffusion or creep'. If viscous creep is the limiting factor, then 'reaction rates are reduced and may become effectively creep controlled'. Schmid et al. (2009) refers to this phenomenon as 'mechanical closure', and is used with this meaning herein. Creep-controlled behaviour can be approximated by considering reaction at constant volume. The consequences of mineral evolution via diffusion (kinetic closure) or creep (mechanical closure) can be visualised on phase diagrams via consideration of conjugate variable pairs.

Choice of variables

While the natural choice of variables to use as axes on a phase diagram for most geological phenomena is pressure and temperature, it is possible that alternative variables are more useful to represent the geological processes occurring in a rock. There are two types of variables occurring as conjugate pairs: *intensive variables* such as pressure (P), temperature (T) and chemical potential

(μ) and *extensive variables* such as volume (V), entropy, (S) and composition (X).

Intensive variables are equalised within the system during equilibration (i.e. pressure by deformation; temperature by conduction and convection; and chemical potential by diffusion), while extensive variables depend on the amount of material present (Powell et al., 2005). The conjugate pairs include an intensive and an extensive variable, T–S, P–V, and μ_k–n_k which can be swapped within the pair to create combinations of axes for diagrams such as P–T and V–T by exchanging pressure with volume. Pseudosections can be drawn, using one each from a pair of conjugate variables.

As real systems may not operate at constant superimposed pressure, a V–T pseudosection can be useful to show how the change in volume of the mineral assemblage relates to changing temperature. Use of a P–T pseudosection makes sense when the host environment of the mineral assemblage can deform to maintain the superimposed far-field pressure. In a case where the host environment is sufficiently strong to resist the volume change associated with a reaction, it is possible to reach a constant volume with superimposed pressure in a closed system and create a pressure gradient between parts of a mineral assemblage (Powell et al., 2005). A V–T pseudosection can then be used to see what assemblages form at constant or varying volume with decreasing temperature.

5.2.4 Summary

Sample S009 preserves evidence of two metamorphic events, M_1 and M_2. The M_2 mineral assemblage is developed as fine-grained reaction textures that partially overprint and separate the M_1 phases and consists of orthopyroxene, gedrite, sillimanite, biotite and quartz. Several interpretations have been proposed for the evolution of the textures including a view that M_2 occurred as part of the retrograde evolution of M_1, rather than as a consequence of two separate events. The current hypothesis is that the Strangways Metamorphic Complex experienced conditions around 8.8 kbar and 850 °C during M_1, having followed a clockwise P–T path. The retrograde history occurred with partial reworking at 6–7kbar and 700–720°C associated with deformation and elevated temperature. This chapter will investigate the mechanism of mechanical closure of mineral assemblages in the context of the reworking of granulites in subsolidus conditions. It will look at the hypothesis that reworking can occur at constant volume by calculation of a P–T pseudosection contoured for reaction volume, followed by an unconventional V–T pseudosection contoured for pressure.

5.3 Mineral equilibria modelling

5.3.1 Methodology

Calculations were performed using THERMOCALC 3.50 using an updated version of the Holland & Powell 2011 data set (**ds633**, July 2019; file tc-ds633.txt). The phases considered in modelling are the a–x models for silicate melt (liq), orthopyroxene (opx), garnet (g), cordierite (cd) (Holland, Green & Powell, 2018), plagioclase (pl) (Holland & Powell, 2003), biotite (bi) (White, Powell, Holland, Green et al., 2014), and gedrite (ged) (pers.comm. Johann Diener 31/10/2016).

The whole rock bulk composition for sample S009 (displayed in Figure 5.2) is identical to that used in Figure 6 in Diener et al. (2008). There are differences in the equilibria attributed to moving from the 2003 updated version of the Holland and Powell (1998) data set (**ds55**) and the **ds633** data set used here. The main consequence of this change is that the solidus has moved down temperature by about 30°C. Using the new data set, the phase relations calculated should

be more geologically realistic as the data set involves more experimental data and better activity–composition models have been used (see discussion in Chapter 3 and Chapter 4)

5.3.2 Pseudosections for residuum compositions

Calculated pseudosections show the stable mineral assemblages in a chemical system for a specified bulk rock composition. Diener et al. (2008) chose the model system Na_2O-CaO-K_2O-FeO-MgO-Al_2O_3-SiO_2-H_2O-TiO_2-Fe_2O_3 (NCKFMASHTO) to calculate the phase relationships of sample S009. This pseudosection has been re-calculated here (Figure 5.2). The H_2O content (here 2.91 mole %) was chosen so that the observed peak M_1 assemblage is stable at conditions just above the solidus. This is done to reflect the conditions directly post final melt loss where the peak assemblage would have been in equilibrium with the last remaining melt phase (White, Powell & Halpin, 2004). The assumption is based on the fact that the peak mineral assemblage is well-preserved, which is consistent with final melt loss or melt consumption at these conditions.

The stable mineral assemblages across P–T for the sample S009 in NCKFMASHTO are shown in Figure 5.2. The preserved M_1 assemblage of orthopyroxene, cordierite, sillimanite, biotite, plagioclase, quartz, rutile and melt in the sample is stable in a narrow field from 8.6 kbar and 780°C to 7.7 kbar and 850°C (Figure 5.2; e.g. black star). The solidus slopes gently towards higher temperature and restricts the melt-bearing assemblage to higher pressure. The melt-absent assemblage below the solidus spans a large P–T area to lower pressure and temperature. The incursion to higher temperature of the solidus in this way is due to the stability of the hydrous mineral, cordierite, competing effectively with melt for H_2O.

The preserved M_2 assemblage of orthopyroxene, gedrite, sillimanite, biotite, quartz and rutile is stable over a narrow, steep P–T band from 4.2 kbar and 530°C to 7.7 kbar and 780°C. The stability field is at lower pressure and higher temperature than adjacent kyanite-bearing equilibria and at higher pressure and lower temperature than gedrite-absent equilibria. Positions for M_1 and M_2 within the stability fields are approximate to those determined by Al^{VI} content in orthopyroxene in Diener et al. (2008).

Modebox diagrams show the modal abundance of the stable minerals for a rock composition along, for example, a P–T path. The change in modal abundance of minerals due to temperature and pressure changes, volume variation, and from the addition/depletion of other minerals can be represented on modebox diagrams. The modal proportions of each phase in a clockwise retrograde path from the solidus shows a decrease in the abundance of sillimanite and orthopyroxene and an increase in cordierite (following the red dashed line in Figure 5.2 with modal proportions displayed in the bottom modebox in Figure 5.4). Diener et al. (2008) explains this by suggesting that M_1 sillimanite is resorbed during melt crystallisation, with the growth of cordierite occurring at sites where the sillimanite is consumed. This would explain fine-grained cordierite coronae around remaining M_1 sillimanite. Within the subsolidus field, a decrease in temperature with no decompression at 6.3 kbar shows a steady decrease in cordierite abundance and an increase in sillimanite. Once the gedrite-bearing equilibria are entered, a dramatic decrease in cordierite is recorded, resulting in the disappearance of M_1 cordierite. The abundance of orthopyroxene also decreases over a short temperature interval, while sillimanite increases. This is consistent with observations by Diener et al. (2008) of new prismatic sillimanite growth and sillimanite-on-sillimanite textures.

When contoured for molar reaction volume of the mineral assemblage (here in kJ $kbar^{-1}$ mol^{-1}), the P–T pseudosection can show the volume change that occurs when continuous and discontinuous reactions take place along a proposed metamorphic path. Any volume change requires the matrix

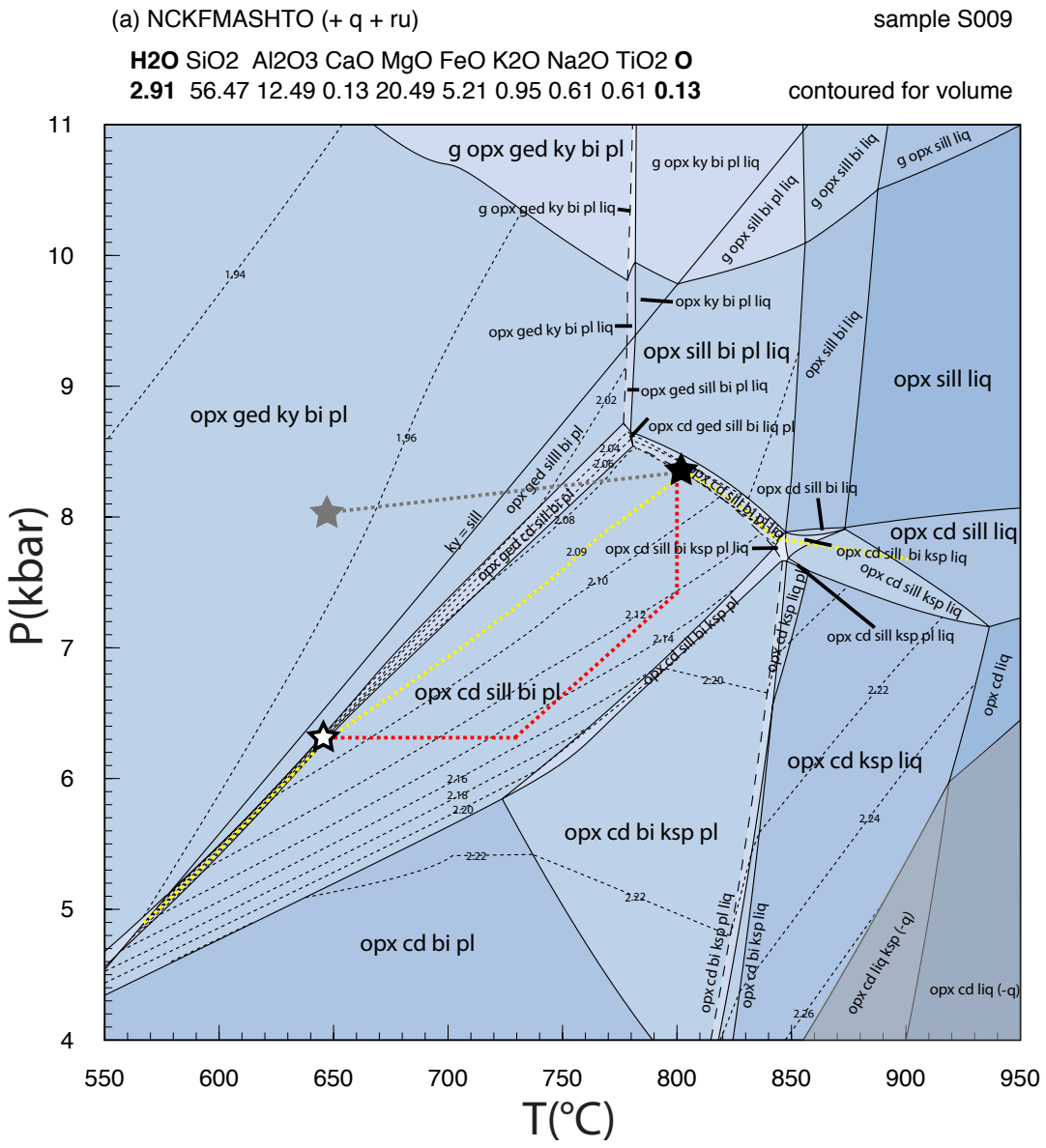

Figure 5.2. Calculated P–T pseudosection for the residuum composition of sample S009, contoured for volume. M_1 conditions are shown as a black star and M_2 conditions are shown as a white-filled star. A near isobaric cooling path is also displayed with a grey star (see Discussion and Conclusions). The size of the symbols is not indicative of the precision of the estimates. The solidus occurs as a black dashed line. Modeboxes in Figure 5.4 are calculated along the red-dashed line (clockwise path so that both M_1 and M_2 conditions are on the section) and the yellow-dashed line (along the 2.09 kJ kbar^{-1} mol^{-1} isochor).

to be able to accommodate this change (through viscous creep) for the change to go to completion. The growth of gedrite is marked by a bulk volume change of -3%, from 2.08 to 2.02 kJ kbar^{-1} mol^{-1} over a short temperature range of <10°C. Per Schmid et al. (2009), a relatively large volume change requires adjustments to the matrix that might not be accounted for by the elastic response of the environment, and would therefore require creep. As suggested by Diener et al. (2008), deformation was required during the M_2 event during reworking for the environment of the reaction volume to accommodate the volume change associated with gedrite growth. If the strength of the deformation was insufficient, reactions would remain incomplete due to the environment of the reaction not accommodating the volume change. The limit is that a reaction is constrained to be along the isochor.

In order to investigate the hypothesis of reworking at constant volume, a path from M_1 to M_2 can be investigated along a constant volume contour. As shown on the P–T diagram, at a pressure of $\sim$ 6.3 kbar (M_2) gedrite appears at a volume of $\sim$ 2.09 kJ kbar^{-1}. It is possible that the rock path crossed the solidus where the volume was 2.09 kJ kbar^{-1}, assuming that the rocks became sufficiently strong to stop accommodating change in volume as pressure and temperature change. The rock then follows the volume contour, with reactions occurring due to local equilibrium in a closed system (see yellow dashed line in Figure 5.2).

A subsequent diagram was constructed using V and T as axes. Figure 5.3 shows the stable mineral assemblages according to volume and temperature. In this diagram, the relationship between the solidus and the isochor is clearer. The 2.09 kJ kbar^{-1} contour and the solidus intersect on this diagram and it is also possible that the rock reached a constant volume due to melt loss early on. In this case, the rock path would follow the 2.09 kJ kbar^{-1} contour as soon as the solidus is reached (see yellow dashed line in Figure 5.3). The top modebox in Figure 5.4 shows the evolution of mineral proportions once the rock has achieved constant volume at 2.09 kJ kbar^{-1}. With decreasing temperature and pressure the mineral abundances vary only slightly once liquid has been lost. Modal changes are slight once constant volume conditions apply. As the environment of the reaction volume is unable to deform, the development of new reaction textures is limited to that of mechanically-controlled local equilibrium.

5.3.3 Summary

Pseudosections for the residuum composition of sample S009 and calculated modeboxes are used to compare the assemblages resulting from kinetic and mechanical closure. Both pathways can result in the growth of gedrite upon reworking. If diffusion is the rate limiting step, then the incomplete M_2 overprint can be explained by sluggish kinetics with decreasing temperature, with reactions stopping just after crossing into the gedrite-bearing field. If viscous creep is rate limiting (mechanical closure), then development of gedrite can be approximated by evolution along an isochor, i.e. at constant volume. This result shows an alternative way that overprinting textures in the orthopyroxene-rich granulites of the Strangways Metamorphic Complex can develop as the rocks became sufficiently strong after M_1 melt loss.

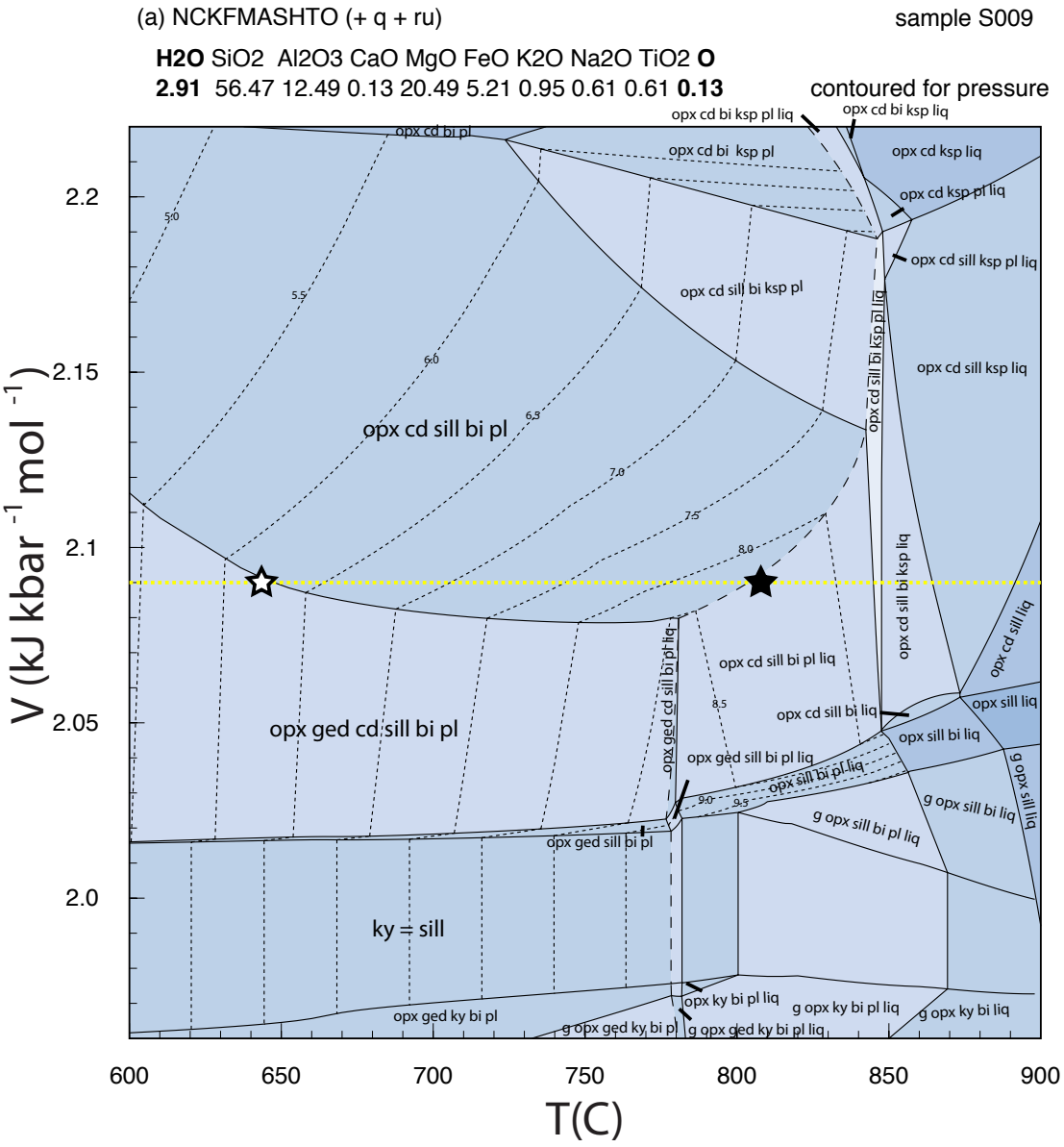

Figure 5.3. Calculated V–T pseudosection for the residuum composition of sample S009, contoured for pressure. M_1 conditions are shown as black stars and M_2 conditions are shown as white-filled stars. The size of the symbols is not indicative of the precision of the estimates. The solidus occurs as a black dashed line. The top modebox in Figure 5.4 is calculated along the yellow-dashed line (along the 2.09 kJ kbar^{-1} mol^{-1} isochor).

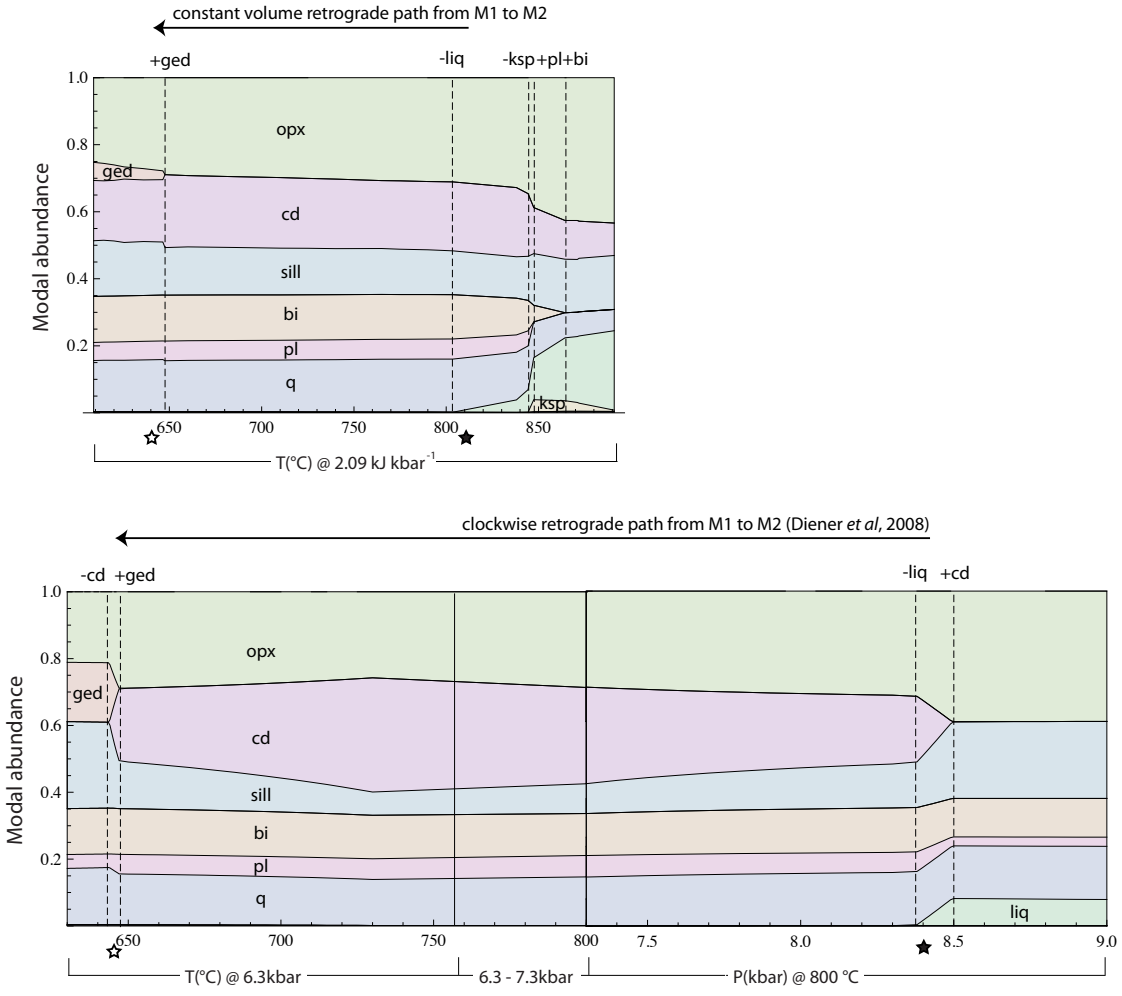

Figure 5.4. Top: Modal composition along the 2.09 kJ kbar^{-1} mol^{-1} isochor (yellow dashed line in Figure 5.2 and Figure 5.3). Bottom: Modal composition along a clockwise P–T retrograde path (red dashed line in Figure 5.2. The diagram is calculated along P–T so that both the M_1 and M_2 metamorphic conditions are represented in the section. M_1 conditions are shown as black stars and M_2 conditions are shown as white-filled stars. The size of the symbols is not indicative of the precision of the estimates.

5.4 Discussion and conclusions

Experimental metamorphic growth studies are conducted under isothermal-isobaric conditions. Powell, Evans, Green and White (2019) provide a discussion of the boundary conditions that are assumed when modelling metamorphic mineral assemblages. Experimental metamorphism, where reactions between minerals in a capsule are investigated, take place at the experimental pressure and temperature. The experiment is held at a certain P–T and the starting materials equilibrate over time as chemical potential gradients are flattened through diffusion. Assuming the reaction vessel are impermeable, no further change will occur once equilibrium is reached. Outside of an experiment, metamorphism occurs progressively where mineral assemblages are continuously developing with changing P–T. Boundary conditions also vary. In a condition where temperature is changed, what happens to the 'reaction vessel' depends on the mechanical boundary of the environment. Where the environment can mechanically adjust to control the pressure imposed on the vessel contents, reactions may only be limited by the reaction kinetics. The alternative is that the environment is such that the reaction vessel is mechanically fixed at a constant volume. The result of equilibration in each case will be different.

In Diener et al. (2008), the view of the mechanism of metamorphism is the conventional approach that a constant pressure boundary condition is assumed for mineral equilibrium calculations. For subsolidus reactions, either deformation or an influx of fluid is required to necessitate reworking. The development of incomplete reaction textures is attributed to sluggish kinetics at lower temperature. Reaction textures can either be formed through retrogression from a singular event, or after a hiatus in the P–T evolution during the same metamorphic event and the reaction is re-initiated, or from multiple unrelated metamorphic events (White & Powell, 2011). The symplectitic overgrowths have been described in many studies investigating the timing of metamorphic events. Warren (1983) describes the intergrowths as forming during isobaric cooling from peak M_1. Norman and Clarke (1990) considers the intergrowths forming at M_2 but at a higher pressure and temperature than M_1. Ballèvre et al. (1997) re-examines similar symplectites from the region and concludes that, as there is little evidence of strain during formation, that the growth did not form during a prograde metamorphic event at high temperature. They further classify the alumninosilicate in the texture as andalusite, and suggest its growth was a result of rehydration in the stability field of andalusite (<4 kbar) during exhumation in the Alice Strings Orogeny at 400–300 Ma.

Here, it is shown that reaction at equilibrium can be attenuated due to the reaction vessel maintaining constant volume, with the external environment unable to accommodate volume change. In the limiting case, reactions continue along an isochor. When the rock enters the gedrite-forming field, reaction continues down the 2.09 $\mathrm{kJ\,kbar^{-1}}$ isochor, which according to Figures 5.2 and 5.3 does not exit the gedrite-bearing field until approximately 4.5 kbar and 560°C where kyanite would begin to form. In other samples, not looked at in this study, late kyanite overprinting sillimanite in M_2 reaction textures has been documented by Goscombe (1992a), consistent with, but not necessarily meaning, further reaction along the isochor to lower pressure.

Reactions evolving under constant volume add complexity to assigning depth values to calculated pressures. To calculate pressure at depth within the Earth during metamorphism within an orogenic belt, the equation for pressure at depth normally invoked is $P = \rho\, g\, h$, where ρ = density, g = gravity and h = depth. A retrograde metamorphic path of the rock with decreasing pressure and temperature (red dashed line, Figure 5.2) uses this assumption whereby pressure and depth can be intrinsically related. The idea that preservation of metamorphic reaction textures due to mechanical closure challenges this assumption as depth cannot be constrained by the min-

eral assemblage. Indeed, the assemblage could represent a multitude of pressures depending on the conditions the rock becomes strong enough to attenuate reaction, and/or the intensity of the imposed deformation varies. The absence of deformation fabrics in the least reworked parts of this sample is consistent with the idea of reaction ceasing at constant volume. As a prediction, it would mean that different parts of a granulite might have subtly different mineral compositions reflecting these pressure variations.

If the granulites were indeed able to deform with superimposed pressure to accommodate the volume change required for reactions post melt loss, then the mineral assemblages formed in the retrograde would be different. Depending on the ability of the environment on different parts of the rocks to accommodate volume change, a highly deformed part of the rock may lie on a different P–T path, with near-isobaric cooling while remaining at depth forming kyanite in the opx–ged–ky–bi–pl stability field (see grey star in Figure 5.2). This would require a volume decrease to approximately 1.96 kJ kba109r^{-1}. This may explain observations by Warren (1983) and Goscombe (1992a) of M_2 kyanite overprint in other samples in the SMC. Parts of rocks of the composition of S009 that have evolved to different volumes, intermediate between these limiting cases, are predicted to have mineral assemblages and mineral compositions reflecting different pressures.

Chapter 6

Thesis conclusions

This thesis has explored some factors influencing phase equilibrium modelling of metamorphic rocks. The work should be seen in the context outlined in the Introduction of the many fronts that theoretical metamorphic petrology advances on, including generating the data used for the quantification of metamorphic processes, and understanding how the mineral assemblages and textures in metamorphic rocks might develop.

In the first part of the thesis, a new activity–composition model for the ilmenite–hematite solid solution has been developed. Calibrated using relatively new experimental data, this model is internally-consistent with the thermodynamic database of Holland and Powell (2011), referred to in the literature as **ds62**, and has been implemented for use in THERMOCALC. Creating the model involved determining a revised critical temperature (T_c) for pure ilmenite; a new estimate of the solvus for the ilmenite–hematite solid solution; new values for macroscopic interaction energies between the ordered and disordered end-members of ilmenite and hematite; and the incorporation of magnesium and manganese into the model using the micro-ϕ approach in the symmetric formalism. This model is an advance on the White et al. (2000) thermodynamic descriptions as it accounts for order–disorder on the A and B sites for Fe^{2+}, Mg^{2+} and Mn^{2+}. As disorder in mineral solid solutions is a contributing factor to mineral stability at higher temperature, this model should be an improvement for use in calculations at higher temperature.

Future work on the ilmenite thermodynamic model could look at incorporating the effects of short-range and magnetic order in order to better model these effects at low temperature. Approximating the effect of short-range order could be done by investigating a proportional reduction in the configurational mixing term, as followed for example in White, Powell, Holland, Green et al. (2014) for the tetrahedral site mixing in the pyroxenes.

The second part of the thesis considered a method for interpreting the P–T history of rocks with domainal textures using an approach involving a P–T grid and compatibility diagram. This approach was developed and tested using a texturally-complex sapphirine–quartz-bearing granulite from the Anosyen tectonic domain in southern Madagascar. Petrographical observations inferred three distinct microdomains that developed post peak. The P–T evolution of these microdomains was deduced by identifying the conditions where the peak assemblages of each microdomain are found, bounded by constraining univariant reactions. A series of orthogonal compatibility diagrams constructed for isothermal decompression showed the progressive formation and evolution of each microdomain as melt is lost at different conditions from different parts of the rock as it moves from overall melt-present to overall melt-absent.

For the same terrane, three other samples were used to further constrain the P–T conditions experienced in the south of the Anosyen. A traditional pseudosection method was used as these

samples are texturally homogeneous. The combined results of the samples indicate that the peak P–T conditions experienced in the south-east of the Anosyen tectonic domain attained at least 850°C and pressures greater than 7.6 kbar. While not providing a conclusive upper temperature for peak assemblages, the modelling shows that sapphirine–quartz-bearing assemblages can be stable at temperatures below 900°C in such an oxidised terrane.

Future studies that involve interpreting the P–T history of high-grade rocks which have equilibrated in domains may benefit from the proposed method involving P–T grids and compatibility diagrams as advocated and applied here. A key to this is being able to identify a chemical system small enough so that a grid and compatibility diagrams can be drawn, while being sufficiently appropriate to represent the mineral assemblages developed.

The final part of the thesis focused on investigating an alternative mechanism for the attenuation of reaction at equilibrium. Absent or incomplete reaction in the retrograde history in the absence of fluid advent is commonly attributed to sluggish kinetics. If the ingredients for retrograde reaction are present, particularly at higher metamorphic grade, is sluggish kinetics a sufficient explanation for lack of or incomplete reaction? Mechanical closure was investigated as a possible contributory mechanism. To see how mineral assemblages can equilibrate under a constant volume process, a volume-temperature (V–T) phase diagram was calculated for a granulite sample that has been reworked in subsolidus fluid-absent conditions. The results show that reaction at equilibrium can be attenuated due to the reaction 'vessel' maintaining constant volume, where the external environment is unable to accommodate volume change of reaction by deformation. Future studies relating to this part of the thesis involve recognising and modelling textures in rocks for which the reaction 'vessel' involved did not operate in the conventional way with P and T superimposed on it, with its composition being just the contents of the vessel.

Bibliography

Ackermand, D., Windley, B. F. & Razafiniparany, A. (1989). The Precambrian mobile belt of southern Madagascar. *Geological Society, London, Special Publications, 43(1)*, 293–296.

Ballèvre, M., Hensen, B. J. & Reynard, B. (1997). Orthopyroxene-andalusite symplectites replacing cordierite in granulites from the Strangways Range (Arunta block, central Australia): A new twist to the pressure-temperature history. *Geology*, *25*, 215–218.

Ballèvre, M., Möller, A. & Hensen, B. J. (2000). Exhumation of the lower crust during crustal shortening: an Alice Springs (380 Ma) age for a prograde amphibolite facies shear zone in the Strangways Metamorphic Complex (central Australia). *Journal of Metamorphic Geology*, *18*, 737–747.

Biermeister, C., Wiesinger, M., Stüwe, K., Foster, D. A., Gibson, H. J. & Raza, A. (2003). Aspects of the structural and late thermal evolution of the Redbank Thrust system, central Australia: constraints from the Speares Metamorphics. *Australian Journal of Earth Sciences*, *50*, 983–999.

Boger, S. D., Ferreira, C. A. M., Hirders, W., Schulte, B., Jennet, T. & Dallwig, R. (2008a). No 11 - Ampanihy, 12 - Tôlanaro. Ministère de l'Energie et des Mines, Project de Gouvernance des Ressources Minèrales, Antananarivo. *Carte Geologique de Madagascar 1:500 000, Feuilles.*

Boger, S. D., Ferreira, C. A. M., Hirders, W., Schulte, B., Jennet, T. & Dallwig, R. (2008b). No 10 - Fianarantsoa. Ministère de l'Energie et des Mines, Project de Gouvernance des Ressources Minèrales, Antananarivo. *Carte Geologique de Madagascar 1:500 000, Feuilles.*

Boger, S. D., Hirdes, W., Ferreira, C. A. M., Jenett, T., Dallwig, R. & Fanning, C. M. (2015). The 580-520 Ma Gondwana suture of Madagascar and its continuation into Antarctica and Africa. *Gondwana Research*, *28*, 1048–1050.

Boger, S. D., Maas, R., Pastuhov, M., Macey, P., Hirdes, W., Schulte, B., ... Dallwig, R. (2019). The tectonic domains of southern and western Madagascar. *Precambrian Research*, *327*, 144–175.

Boger, S. D., White, R. W. & Schulte, B. (2012). The importance of iron speciation (Fe^{2+}/Fe^{3+}) in determining mineral assemblages: an example from the high0grade aluminous metapelites of southeastern Madagascar. *Journal of Metamorphic Petrology*, *30*, 997–1018.

Bowen, N. L. (1940). Progressive metamorphism of siliceous limestone and dolomite. *Journal of Geology*, *48*, 225–274.

Burton, B. P. (1984). Thermodynamic analysis of the system Fe_2O_3–$FeTiO_3$. *Physics and Chemistry of Minerals*, *11*, 132–139.

Burton, B. P. (1985). Theoretical analysis of chemical and magnetic ordering in the system Fe_2O_3–$FeTiO_3$. *American Mineralogist*, *70*, 1027–1035.

Burton, B. P., Chaka, A. & Singh, D. J. (2005). Chemical, magnetic and charge ordering in the system hematite-ilmenite, Fe_2O_3-$FeTiO_3$. *Phase Transitions*, *78*, 239–249.

Callen, H. B. (1985). *Thermodynamics and an Introduction to Thermostatistics* (Second). John Wiley & Sons.

Carmichael, D. M. (1987). *Induced Stress and Secondary Mass Transfer: Thermodynamic Basis for the Tendency toward Constant-Volume Constraint in Diffusion Metasomatism*. Springer, Dordrecht.

Carson, C. J. & Powell, R. (1996). Garnet–orthopyroxene geothermomentry and geobarometry: error propagation and equilibration effects. *Journal of Metamorphic Geology*, *15*, 679–686.

Chinner, G. A. (1960). Pelitic gneisses with varying ferrous/ferric ratios from Glen Angus, Scotland. *Journal of Petrology*, *1*, 178–217.

Clark, C., Hand, M., Kelsey, D. E. & Goscombe, B. (2007). Linking crustal reworking to terrane accretion. *Journal of the Geological Society, London*, *164*, 937–940.

Clarke, G. L., White, R. W., Lui, S., Fitzherbert, J. A. & Pearson, N. (2007). Contrasting behaviour of rare earth and major elements during partial melting in granulite facies migmatites, Wuluma Hills, Arunta Block, central Australia. *Journal of Metamorphic Geology*, *25*, 1–18.

Connolly, J. A. D. (1990). Multivariable phase-diagrams - an algorithm based on generalized thermodynamics. *American Journal of Science*, *290*, 666–718.

de Capitani, C. & Petrakakis, K. (2010). The computation of equilibrium assemblage diagrams with Theriak/Domino software. *American Mineralogist*, *95*, 1006–1016.

Diener, J. F. A., White, R. W. & Hudson, T. J. M. (2014). Melt production, redistribution and accumulation in mid-crustal source rocks, with implications for crustal-scale melt transfer. *Lithos*, *200-201*, 212–225.

Diener, J. F. A., White, R. W. & Powell, R. (2008). Granulite facies metamorphism and subsolidus fluid–absent reworking, Strangways Range, Arunta Block, central Australia. *Journal of Metamorphic Geology*, *26*, 603–622.

Evans, B. W., Scaillet, B. & Kuehner, S. M. (2006). Experimental determination of co-existing iron-titanium oxides in the systems FeTiAlO, FeTiAlMgO, FeTiAlMnO, and FeTiAlMgMnO at 800 and 900°C, 1–4 kbar, and relatively high oxygen fugacity. *Contributions to Mineralogy and Petrology*, *152*, 149–167.

Evans, K. A., Powell, R. & Frost, B. R. (2013). Using equilibrium thermodynamics in the study of metasomatic alteration, illustrated by an application to serpentinites. *Lithos*, *168–169*, 67–84.

Fyfe, W. S., Price, N. J. & Thompson, A. B. (1978). *Fluids in the Earth's Crust*. Amsterdam: Elsevier.

GAF-BGR. (2008). Final report. Explanatory notes for the Anosyen Domain southeast Madagascar. Réalisation des travaux de cartographie géologique de Madagascar, révision approfondie de la cartographie géologique et minière aux échelles 1/100,000 et 1/500,000 zone Sud. Republique de Madagascar, *Republique de Madagascar, Ministère de L'energie et des Mines (MEM/SG/DG/UCP/PGRM)*, 93.

Ghiorso, M. S. (1990). Thermodynamic properties of hematite–ilmenite–geikielite solid solutions. *Contributions to Mineralogy and Petrology*, *104*, 645–667.

Ghiorso, M. S. (1997). Thermodynamic analysis of the effect of magnetic ordering on miscibility gaps in the FeTi cubic and rhomohedral oxide minerals and the FeTi oxide geothermometer. *Physics and Chemistry of Minerals*, *25*, 28–38.

Ghiorso, M. S. & Evans, B. W. (2008). Thermodynamics of rhombohedral oxide solid solutions and a revision of the Fe-Ti-oxide geothermometer and oxygen-barometer. *American Journal of Science*, *308*, 957–1039.

Goscombe, B. D. (1991). Intense non-coaxial shear and the development of mega-scale sheath folds in the Arunta Block, central Australia. *Journal of Structural Geology*, *13*, 299–318.

Goscombe, B. D. (1992a). High-grade reworking of central Australian granulites. Part 1. Structural Evolution. *Journal of Petrology*, *33*, 917–962.

Goscombe, B. D. (1992b). High-grade reworking of central Australian granulites: metamorphic evolution of the Arunta Complex. *Tectonophysics*, *204*, 361–399.

Guevara, V. E. & Caddick, J. (2016). Shooting at a moving target: phase equilibria modelling of high-temperature metamorphism. *Journal of Metamorphic Geology*, *34*, 209–235.

Guiraud, M., Powell, R. & Rebay, G. (2001). H_2O in metamorphism and unexpected behaviour in the preservation of metamorphic mineral assemblages. *Journal of Metamorphic Geoogy*, *19*, 445–454.

Hacker, B. R. & Peacock, S. M. (1995). Creation, preservation, and exhumation of ultrahigh pressure metamorphic rocks. In R. C. Coleman & X. Wang (Eds.), *Ultrahigh Pressure Metamorphism* (pp. 159–181). Cambridge: Cambridge University Press.

Harley, S. L. (2008). Refining the PT records of UHT crustal metamorphism. *Journal of Metamorphic Geology*, *26*, 125–154.

Harrison, R. J., Becker, U. & Redfern, S. (2000). Thermodynamics of the $R\bar{3}$ to $R\bar{3}c$ phase transition in the ilmenite-hematite solid solution. *American Mineralogist*, *85*, 1694–1705.

Harrison, R. J. & Redfern, S. A. T. (2001). Short- and long–range ordering in the ilmenite–hematite solid solution. *Physics and Chemistry of Minerals*, *28*, 399–412.

Harrison, R. J., Redfern, S. & Smith, R. I. (2000). In-situ study of the $R\bar{3}$ to $R\bar{3}c$ phase transition in the ilmenite-hematite solid solution using time-of-flight neutron powder diffraction. *American Mineralogist*, *85*, 194–205.

Harrison, R. J., Stone, H. J. & Redfern, S. A. T. (2006). Pressure dependence of Fe–Ti order in the ilmenite–hematite solid solution: Implications for the origin of lower crustal magnetization. *Physics of the Earth and Planetary Interiors*, *154*, 266–275.

Holder, R. M., Hacker, B., Horton, F. & Rakotondrazafy, A. F. M. (2018). Ultrahigh-temperature osumilite gneisses in southern Madagascar record combined heat advection and high rates of radiogenic heat production in a long-lived high-T orogen. *Journal of Metamorphic Geology*, *36*, 855–880.

Holland, T. J. B., Babu, E. V. S. S. K. & Waters, D. J. (1996). Phase relations of osumilite and dehydration melting in pelitic rocks: A simple thermodynamic model for the KFMASH system. *Contributions to Mineralogy and Petrology*, *124*, 383–394.

Holland, T. J. B., Green, E. & Powell, R. (2018). Melting of peridotites through to granites: a simple thermodynamic model in the system KNCFMASHTOCr. *Journal of Petrology*, *59*, 881–900.

Holland, T. J. B. & Powell, R. (1990). An enlarged and updated internally consistent thermodynamic dataset with uncertainties and correlations; the system K_2O–Na_2O–CaO–MgO–MnO–FeO–Fe_2O_3–Al_2O_3–TiO_2–SiO_2–C-H_2–O_2. *Journal of Metamorphic Geology*, *8*, 89–124.

Holland, T. J. B. & Powell, R. (1996a). Thermodynamics of order-disorder in minerals: I. Symmetric formalism applied to minerals of fixed composition. *American Mineralogist*, *81*, 1413–1424.

Holland, T. J. B. & Powell, R. (1996b). Thermodynamics of order-disorder in minerals: II. Symmetric formalism applied to solid solutions. *American Mineralogist*, *81*, 1425–1437.

Holland, T. J. B. & Powell, R. (1998). An internally consistent dataset for phases of petrological interest. *Journal of Metamorphic Geology*, *16*, 309–343.

Holland, T. J. B. & Powell, R. (2003). Activity-composition relations for phases in petrological calculations: an asymmetric multicomponent formulation. *Contributions to Mineralogy and Petrology*, *145*, 492–501.

Holland, T. J. B. & Powell, R. (2011). An improved and extended internally-consistent thermodynamic dataset for phases of petrological interest, involving a new equation of state for solids. *Journal of Metamorphic Geology*, *29*, 333–383.

Horton, F., B., H., Kylander-Clark, A., R., H. & Jöns, N. (2016). Focused radiogenic heating of middle crust caused ultrahigh temperatures in southern Madagascar. *Tectonics*, *35*, 293–314.

Jöns, N. & Schenk, V. (2008). Relicts of the Mozambique Ocean in the central East African Orogen: Ecidecnce from the Vohibory block of southern Madagascar. *Journal of Metamorphic Geology*, *26(1)*, 17–28.

Jöns, N. & Schenk, V. (2011). The ultrahigh temperature granulites of southern Madagascar in a polymetamorphic context: implications for the amalgamation of the Gondwana supercontinent. *European Journal of Mineralogy*, *23*, 127–156.

Kelsey, D. E., White, R. W. & Powell, R. (2005). Calculated phase equilibria in K_2O–FeO–MgO–Al_2O_3–SiO_2–H_2O for silica-undersaturated sapphirine-bearing mineral assemblages. *Journal of Metamorphic Geology*, *23*, 217–239.

Kröner, A., Braun, I. & Jaeckel, P. (1996). Zircon geochronology of anatectic melts and residues from a high-grade pelitic assemblage at Ihosy, southern Madagascar: evidence for Pan-African granulite metamorphism. *Geological Magazine*, *133*, 311–323.

Lattard, D., Sauerzapf, U. & Käsemann, M. (2005). New calibration data for the Fe–Ti oxide thermo-oxybarometers from experiments in the Fe–Ti–O system at 1 bar, 1,000–1,300°C and a large range of oxygen fugacities. *Contributions to Mineralogy and Petrology*, *149*, 735–754.

Meert, J. G. (2003). A synopsis of events related to the assembly of eastern Gondwana. *Tectonophysics*, *362*, 1–40.

Milke, R., Abart, R., Kunze, K., Kock-Muller, M. & Schmid, P., D. W. and. Ulmer. (2009). Matrix rheology effects on reaction rim growth I: evidence from orthopyroxene rim growth experiments. *Journal of Metamorphic Geology*, *27*, 71–82.

Moine, B., Takotondratsima, C. & Cuney, M. (1985). Les pyroxenites a urano-thorianite du sud-est de Madagascar: conditions physico-chimique de la metasomatose. *Bulletin de Mineralogie*, *108*, 325–340.

Möller, A., Hensen, B. J., Armstron, R. A., Mezger, K. & Ballevre, M. (2003). U-Pb zircon and monazite age constraints on granulite-facies metamorphism and deformation in the Strangways Metamorphic Complex (central Australia). *Contributions to Mineralogy and Petrology*, *145*, 406–423.

Mosenfelder, J. L. & Bohlen, S. R. (1997). Kinetics of the coesite to quartz transformation. *Earth and Planetary Science Letters*, *153*, 133–147.

Nicollet, C. (1989). L'eclogite de Faratsiho (Madagascar): Un cas exceptionnel de mètamorphisme de haut-P-basse-T au Protèrozoïc supèrieur. *Precambrian Research*, *45(4)*, 343–352.

Norman, A. R. & Clarke, G. L. (1990). A barometric response to late compression in the Strangways Metamorphic Complex, Arunta Block, Central Australia. *Journal of Structural Geology*, *12*, 667–684.

Paterson, M. S. (1995). A theory for granular flow accommodated by material transfer via an intergranular fluid. *Tectonophysics*, *245*, 135–151.

Powell, R. (1978). *Equilibrium Thermodynamics in Petrology: an Introduction*. Harper and Row Publishers.

Powell, R. (1983). Processes in granulite facies metamorphism. In M. P. Atherton & C. D. Gribble (Eds.), *Migmatites, Melting and Metamorphism* (pp. 127–139). London: Shiva.

Powell, R., Evans, K. A., Green, E. C. R. & White, R. W. (2019). The truth and beauty of chemical potentials. *Journal of Metamorphic Geology*, *7*, 1007–1019.

Powell, R., Guiraud, M. & White, R. W. (2005). Truth and beauty in metamorphic mineral equilibria: conjugate variables and phase diagrams. *Canadian Mineralogist*, *43*, 21–33.

Powell, R. & Holland, T. J. B. (1985). An internally consistent thermodynamic dataset with uncertainties and correlations; I, Methods and a worked example. *Journal of Metamorphic Geology*, *3*, 327–342.

Powell, R. & Holland, T. J. B. (1988). An internally consistent dataset with uncertainties and correlations; 3, Applications to geobarometry, worked examples and a computer program. *Journal of Metamorphic Geology*, *6*, 173–204.

Powell, R. & Holland, T. J. B. (1993). On the formulation of simple mixing models for complex phases. *American Mineralogist*, *78*, 1174–1180.

Powell, R., Holland, T. & Worley, B. (1998). Calculating phase diagrams involving solid solid solutions via non-linear equations, with examples using THERMOCALC. *Journal of Metamorphic Geology*, *16*, 577–588.

Powell, R., White, R. W., Green, E. C. R., Holland, T. J. B. & Diener, J. F. A. (2014). On parameterising thermodynamic descriptions of minerals for petrological calculations. *Journal of Metamorphic Geology*, *32*, 245–260.

Rakotonandrasana, N. O. T., Arima, M., Miyawaki, R. & Rambeloson, R. A. (2010). Widespread occurrences of hogbomite-2N2S in UHT metapelites from the Betroka Belt, Southern Madagascar: Implications on melt or fluid activity during regional metamorphism. *Journal of Petrology*, *51(4)*, 869–895.

Sack, R. O. (1980). Some constraints on the thermodynamic mixing properties of Fe–Mg orthopyroxenes and olivines. *Contributions to Mineralogy and Petrology*, *71*, 257–269.

Sack, R. O. & Ghiorso, M. S. (1991). Chromian spinels as petrogenetic indicators: Thermodynamics and petrological applications. *American Mineralogist*, *76*, 827–847.

Schmid, D. W., Abart, R., Podladchikov, Y. Y. & Milke, R. (2009). Matrix rheology effects on reaction rim growth II: coupled diffusion and creep model. *Journal of Metamorphic Geology*, *27*, 83–91.

Taylor-Jones, K. & Powell, R. (2010). The stability of sapphirine + quartz: calculated phase equilibria in FeO–MgO–Al_2O_3–SiO_2–TiO_2–O. *Journal of Metamorphic Geology*, *28*, 615–633.

Thomas, J. B., Watson, E., Spear, F. S., Shemlla, S. K., Nyak, S. K. & A., L. (2010). TitaniQ under pressure: the effect of pressure and temperature on the solubility of Ti in quartz. *Contributions to Mineralogy and Petrology*, *160(5)*, 743–759.

Thompson, J. B. (1967). Thermodynamic properties of simple solutions. In P. H. Abelson (Ed.), *Researches in geochemistry* (pp. 340–361). New York: Wiley.

Tucker, R. D., Roig, J. Y., Moine, B., Delor, C. & Peters, S. G. (2014). A geological synthesis of the Precambrian Shield in Madagascar. *Journal of African Earth Sciences*, *94*, 9–30.

Warren, R. G. (1983). Metamorphic and tectonic evolution of granulites, Arunta Block, central Australia. *Nature*, *305*, 300–303.

Webb, G., Powell, R. & Mclaren, S. (2015). Phase equilibria constraints on the melt fertility of crustal rocks: the effect of subsolidus water loss. *Journal of Metamorphic Geology*, *33*, 147–165.

Wheller, C. J. & Powell, R. (2014). A new thermodynamic model for sapphirine: calculated phase equilibria in K_2O–FeO–MgO–Al_2O_3–SiO_2–H_2O–TiO_2–Fe_2O_3. *Journal of Metamorphic Geology*, *32*, 287–299.

White, R. W. & Powell, R. (2002). Melt loss and the preservation of granulite facies mineral assemblages. *Journal of Metamorphic Geology*, *20*, 621–632.

White, R. W. & Powell, R. (2011). On the interpretation of retrograde reaction textures in granulite facies rocks. *Journal of Metamorphic Geology*, *29*, 131–149.

White, R. W., Powell, R. & Clarke, G. L. (2002). The interpretation of reaction textures in Fe-rich metapelitic granulites of the Musgrave Block, central Australia: constraints from mineral equilibria calculations in the system K_2O–FeO–MgO–Al_2O_3–SiO_2–H_2O–TiO_2–Fe_2O_3. *Journal of Metamorphic Geology*, *20*, 41–55.

White, R. W., Powell, R. & Halpin, J. A. (2004). Progress relating to calculation of partial melting equilibria for metapelites. *Journal of Metamorphic Geology*, *25*, 511–527.

White, R. W., Powell, R. & Holland, T. J. B. (2001). Calculation of partial melting equilibria in the system Na_2O–CaO–K_2O–FeO–MgO–Al_2O_3–SiO_2–H_2O (NCKFMASH). *Journal of Metamorphic Geology*, *19*, 139–153.

White, R. W., Powell, R. & Holland, T. J. B. (2007). Progress relating to calculation of partial melting equilibria for metapelites and felsic gneisses. *Journal of Metamorphic Geology*, *25*, 511–527.

White, R. W., Powell, R., Holland, T. J. B., Green, E. C. R., Johnson, T. J. & Diener, J. F. A. (2014). Thermodynamic calculations in metapelitic systems: new activity–composition relations. *Journal of Metamorphic Geology*, *32*, 261–286.

White, R. W., Powell, R., Holland, T. J. B. & Worley, B. A. (2000). The effect of TiO_2 and Fe_2O_3 on metapelitic assemblages at green schist and amphibolite facies conditions: mineral equilibria calculations in the system K_2O–FeO–MgO–Al_2O_3–SiO_2–H_2O–TiO_2–Fe_2O_3. *Journal of Metamorphic Geology*, *18*, 497–411.

White, R. W., Powell, R. & Johnson, T. J. (2014). The effect of Mn on mineral stability in metapelites revisited: new *a-x* relations for manganese-bearing minerals. *Journal of Metamorphic Geology*, *32*, 809–828.

Yardley, B. W. D. (2009). The role of water in the evolution of the continental crust. *Journal of the Geological Society*, *166*, 585–600.